1-1-2013

Biomaterial-Induced Osteogenesis of Mesenchymal Stem Cells by Surface Roughness and Functionalization

Pongkwan Sitasuwan
University of South Carolina - Columbia

BIOMATERIAL-INDUCED OSTEOGENESIS OF MESENCHYMAL STEM CELLS BY SURFACE ROUGHNESS AND FUNCTIONALIZATION

by

Pongkwan Sitasuwan

Bachelor of Applied Science
University of Otago, 2007

Submitted in Partial Fulfillment of the Requirements

For the Degree of Doctor of Philosophy in

Chemistry

College of Arts and Sciences

University of South Carolina

2013

Accepted by:

Qian Wang, Major Professor

James M. Sodetz, Committee Member (Chair)

Caryn E. Outten, Committee Member

Jay Potts, Committee Member

Lacy Ford, Vice Provost and Dean of Graduate Studies

ACKNOWLEDGEMENTS

I first would like to thank my advisor Prof. Qian Wang. As a mentor and a friend, he encouraged and guided me through my graduate study with passion and sincerity. Qian provided me with unwavering support and confidence in my abilities, allowing me to pursue my research goals and successful results. He has given me the opportunity to work in an interdisciplinary field, which expose me to various new techniques. Although the projects are outside of Qian's area of expertise, his insightful vision shaped them up and his trust in my experimental details moved them forward. I would like to extend my gratitude to two senior graduate students who taught me new laboratory techniques, Andrew Lim Lee, Ph.D. and Gagandeep Kaur, Ph.D. Through their experienced lessons, I was able to overcome problems and be effective at troubleshooting. I also had a privilege to work with Prof. Tara Sabo-Attwood, an expert in gene expression detection, during my first two years of my graduate school until she moved to another university. I owe thanks to Tara for her help in primer design and signaling pathway analysis.

I would like to express my sincere gratitude towards former and current fellow laboratory members for creating a supportive and fun working environment, especially Eve Nisaraporn Suthiwangcharoen, Ph.D., Sharmistha Saha, Ph.D., Elizabeth Balizan, Ph.D., Jittima Luckanagul, Kamonrat Metavarayuth, Quyen Nguyen, and Erin N. Davis. I have enjoyed my five years working and spending time with all of you.

Thank you my beloved family members, my parents and my older brothers, for their unconditional love and support. Their encouragement and understanding has provided me the greatest comfort and strength.

ABSTRACT

For tissue engineering and regenerative medicine, it is important to understand factors directing the stem cell fate, including self-renewal, proliferation, differentiation, and apoptosis. Bone marrow derived mesenchymal stem cells (BMSCs) have the potential to differentiate into osteoblasts, chondrocytes, adipocytes, and smooth muscle cells. Specifically, in the field of bone tissue engineering, BMSCs are commonly used for *in vitro* osteogenesis studies. However the mechanisms and signaling pathways that these cells recognize material surface and utilize to differentiate are still unclear. This dissertation focuses on investigating the effect of surface nanotopography and functionalization on the promotion of osteogenic differentiation of BMSCs. Surface topographies were created by *Tobacco mosaic virus* (TMV) for chapter 1-5, *Turnip yellow mosaic virus* (TYMV) for chapter 6, and calcium phosphate crystals (CaP) for chapter 7. These surfaces were previously documented to promote osteogenesis.

The first two chapters present the study of early endogenous bone morphogenetic protein 2 (BMP2) expression pattern which is believed to be responsible for accelerated osteogenesis, and possible pathways that TMV substrate can induce BMP2 upregulation. It was discovered that BMP2 had a peak expression level at 8 hours after osteoinduction on TMV substrate, similar to stress-induced osteogenesis. The underlying mechanisms may be overlapping. Chapter 3 involves the decoration of adhesive peptide on the exterior surface of TMV particles via a Click reaction to improve cell adhesion on TMV

substrate. The results indicate that the presence of cell adhesive sequence combined with nanotopography of TMV substrate can further enhance the expression of osteospecific genes. Chapter 4 demonstrates the study of different TMV nanostructures on osteogenesis of BMSCs. TMV subunits can be diassembled and reassembled without internal RNA strand. However, the reassembled TMV was not stable in culture conditions. Native rod-like TMV particles are also transformed to spherical particles upon heat denaturation. Chapter 5 attempts to create a reproducible and even monolayer of TMV for consistent cell culture experiment utilizing layer-by-layer deposition.

Nanoparticles are switched from TMV to TYMV in chapter 6 to study the effect of genetically modified TYMV presenting cell adhesive peptides on its surface on osteogenesis of BMSCs. Although both TMV and TYMV coated substrates have previously been reported to accelerate osteogenic differentiation, the particle shapes are distinctively different. TMV is a rod while TYMV is a sphere. The result illustrates that genetic mutation of TYMV is effective in displaying multivalent ligands on plant viral particles and mutant TYMV enhances BMSC adhesion depending on the amount of virus coating. The last chapter studies the osteoinductivity of calcium phosphate (CaP)-based surface generated *in situ* by nucleation on polyelectrolyte multilayer films. The novel fabrication of CaP coating is demonstrated as an example to easily create a biomimetic surface with controllable roughness on bone implant materials.

Collectively, the research presented in this dissertation explores into the osteogenic potential of BMSCs on different 2D surface topographies and functionalities, in order to gain insights into the design of functional biomaterials for tissue engineering and regenerative medicine applications.

TABLE OF CONTENTS

LIST OF TABLES

LIST OF FIGURES

CHAPTER 1

PLANT VIRUS SUBSTRATE INDUCES EARLY UPREGULATION OF BMP2 FOR RAPID BONE FORMATION[1]

1.1 INTRODUCTION

1.1.1 Bone marrow derived mesenchymal stem cells

Stem cell fate is dependent on the surrounding stimuli, including both soluble and insoluble factors. How stem cells respond to different nanoscale cues has been extensively studied for tissue engineering and regenerative medicine applications [1-4]. There are several reports indicating that stem cell differentiation can be dictated at the nanometer level [5-14]. Bone marrow derived mesenchymal stem cells (BMSCs) are from the non-hematopoietic sub-population of bone marrow stroma [15-17], which have the ability to self-renew and differentiate to various lineages, such as adipocytes, osteocytes, chondrocytes, hepatocytes, neurons, muscle cells, and epithelial cells [17-22]. The pluripotent potential of BMSCs, ease of isolation, rapid expansion [23], and less controversial use than embryonic stem cells make this cell type an ideal source of adult stem cells to study material-mediated differentiation.

1.1.2 Plant virus-based substrates for accelerated osteogenesis

Recently, we have reported accelerated osteogenic differentiation for BMSCs grown on

[1] Sitasuwan P, Andrew Lee L, Bo P, Davis EN, Lin Y, Wang Q. 2012. *Integr Biol.* 4: 651-60. Reprinted here with permission of publisher (Appendix A).

plant virus coated substrates in comparison to cells cultured on conventional tissue culture plastic (TCP) [24, 25]. Two different plant viruses were employed in those studies, i.e. spherical *Turnip yellow mosaic virus* (TYMV) and rod-like *Tobacco mosaic virus* (TMV). In both situations, several key mRNA markers associated with bone differentiation peaked at day 14 for cells on virus-coated substrates, whereas the cells on conventional plates required an additional 7 days to reach similar expression profiles [24, 25]. Moreover, immunohistochemical staining for osteoblastic specific differentiation markers, osteocalcin, osteonectin, and osteopontin, had supported the gene expression profiles on day 14. The expression of such osteogenic markers were further enhanced upon chemically modifying the virus with phosphates as indicated by increased Ca^{2+} mineralization and even higher mRNA expression levels of osteocalcin [26]. More importantly, gene profile studies of total mRNA and real time PCR suggested an early upregulation of endogenous mRNA levels of bone morphogenetic protein-2 (BMP2). This increase in BMP2 mRNA level was observed for BMSCs cultured on TMV substrates within 24 hours of osteoinduction, which we speculate may be a key factor in the enhanced differentiation of BMSCs on virus coated substrates [24].

1.1.3 Bone morphogenetic protein 2 as a key osteogenic initiator

BMP2 is a member of bone morphogenetic protein subgroup within the transforming growth factor β (TGF-β) super family. Among the bone morphogenetic proteins (BMPs), the role of BMP2 in osteoblast differentiation and bone formation during embryonic skeletal development and postnatal bone remodelling have been extensively investigated [27-31]. Animal studies have shown that *BMP2* mRNA expression was at maximal level

within 24 hours of murine fracture injury, indicating that BMP2 is highly involved with bone repair initiation [32]. The results from another study showed that BMP2, BMP6, and BMP9 were potent inducers of mesenchymal stem cell differentiation towards osteoblasts [33]. Recombinant human BMP2 is commercially available and used as a therapeutic supplement for bone repair in spine fusion surgeries and tibial fracture healing [34]. The supplement can promote faster bone fusion for patients with back pain by promoting bone formation *in vivo*, and many hydrogel encapsulation studies have shown enhanced osteogenic differentiation of MSCs *in vitro* [35, 36].

However, rhBMP2 is costly and some recent studies reported the adverse effects caused by implant failure or leakage causing life-threatening urogenital events, retrograde ejaculation, back and leg pain, hematoma, or breathing difficulty [37, 38]. Therefore, the use of nanoscale materials to promote endogenous BMP2 production becomes an extremely attractive route for bone regeneration without systemic inductive supplements. This report is to examine the virus-based system and its role in early differentiation of BMSCs by monitoring its ability to upregulate BMP2 expression.

1.1.4 TMV substrate-induced early BMP2 upregulation

TMV is a rod-shaped particle measuring 300 nm in length with a diameter of 18 nm. The shape of the plant virus resembles the size scales of fibrillar extracellular matrix (ECM) protein, such as collagen. The viral capsid consists of 2130 identical coat protein subunits assembled in a helical structure around the single stranded genomic RNA. The production of TMV is cost effective and the resulting viral particles are highly uniform in size. The ability of TMV to be easily and uniformly manipulated via chemical [26, 39,

40] and genetic modifications [41-43] has gained traction as novel biomaterials for potential tissue engineering applications [44-49]. Herein, we report the early molecular events that occur within the first 24 hours of osteoinduction in BMSCs when cultured on TMV-coated substrates.

1.2 RESULTS AND DISCUSSION

1.2.1 The morphological differences of BMSCs on TCP versus TMV substrates

The topographical features of TMV substrate before and after incubation in media observed by atomic force microscopy revealed such rough surfaces from the TMV coating, which was still visible after 24 hours of cell culture (Figure 1.1). The result indicated that TMV coating was stable for cell culture experiments. The morphological difference of BMSCs cultured on TCP or TMV coated substrates (e.g. 3-aminopropyltriethoxysilane (APTES) grafted coverslips) were imaged at the early time points. After 6 hours in basal media, cells on TCP fully spread on the substrate (Figure 1.2 A), whereas cells seeded on TMV wafers partially spread (Figure 1.2 D). 24 hours after seeding, BMSCs on TCP sample continued to spread and cover the entire substrate (Figure 1.2 B), whereas the cells on TMV-coated substrate aggregated to form nodule-like cell clumps (Figure 1.2 E). After 24 hours of culture in basal media, the media was changed to osteogenic media and the cells were imaged again 8 hours later. The cells on TCP remained spread out with no aggregation (Figure 1.2 C), and the cells on TMV substrates continued to form larger aggregates (Figure 1.2 F).

Cell adhesion and spreading are highly dependent of substrate surface. Interestingly, in this study, the cell morphologies were distinct as early as at 6-hour post

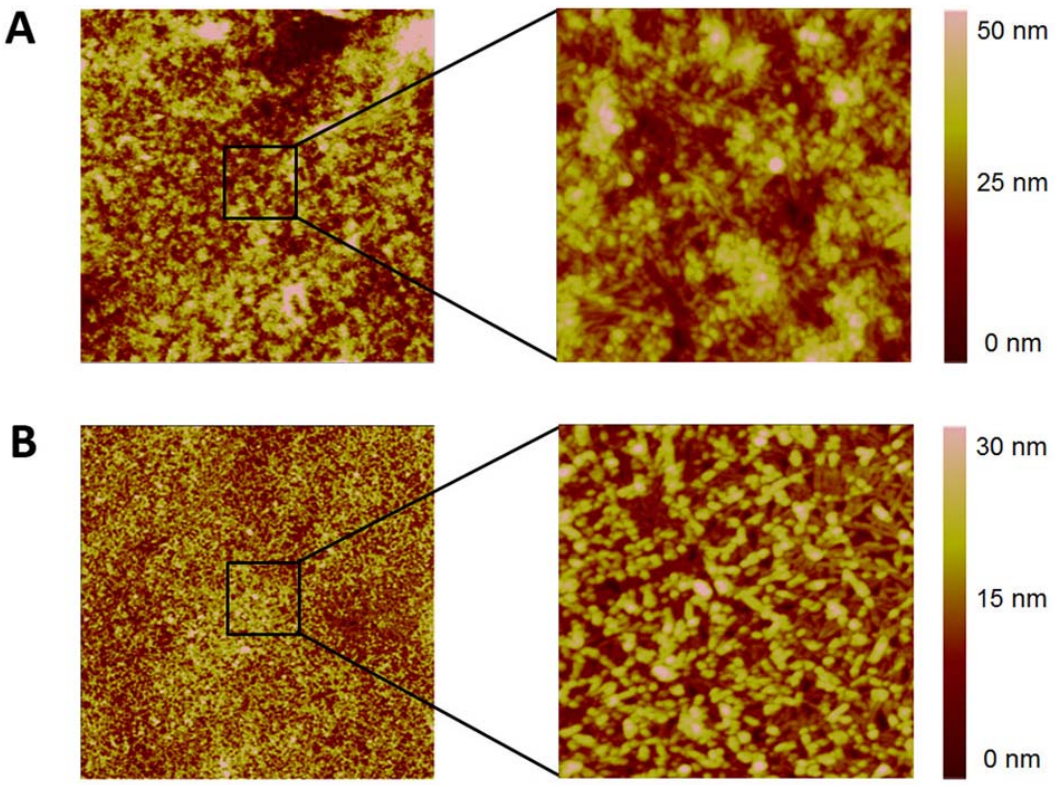

Figure 1.1 Representative AFM micrographs showing the stability of TMV substrate after 24 hours incubation. (*A*) Silane wafer coated with 3 μg/cm^2 TMV nanoparticles. Left: the wafer is completely covered with multilayers of TMV (scan area is 10 μm). Right: the morphology of rod-shape virus is visible (scan area is 2 μm). (*B*) TMV-coated wafer after 24 hours incubation in PBS at 37 °C. Left: the wafer is still completely covered with a few layers of TMV (scan area is 10 μm). Right: the rod-shape virus is still visible showing intact viral particles on the substrate.

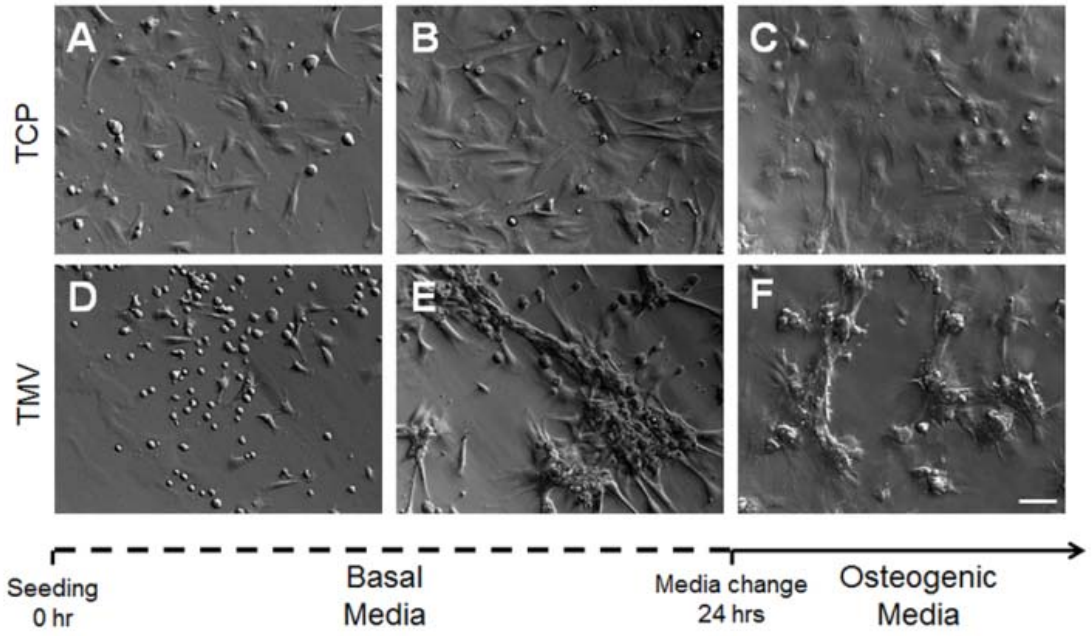

Figure 1.2 Differential interference contrast (DIC) images of BMSCs on TCP and TMV substrates showing morphological changes over culture time. The time points are (*A*, *D*) 6 hours and (*B*, *E*) 24 hours after seeding in basal media, followed by (*C*, *F*) 8 hours in osteogenic media. The cells on standard TCP are well spread (*A* - *C*), whereas the cells on TMV coated substrate are often rounded and poorly spread (*D* - *F*). Scale bar is 100 μm.

seeding. The difference in cell shapes observed indicates altered cellular responses. Gene and protein analyses during the first 24 hours of osteoinduction were carried out to identify how TMV substrate could enhance osteogenesis of BMSCs. In order to examine if TMV is capable of chemically inducing the changes, the supplement of TMV into culture media was included in all studies. It is important to note that the morphology of BMSCs grown in media supplemented with TMV remained the same with that of TCP control (data not shown).

1.2.2 TMV on surface alters BMP2 and IBSP gene expression

In the previous study, we found enhanced osteogenic differentiation of BMSCs when cultured on TMV coated APTES glass coverslips [24]. Without TMV coating, the APTES glass coverslips showed similar effects as uncoated glass and TCP. Microarray analysis of total cellular mRNA and real time PCR results indicated that BMP2 mRNA level was higher in cells cultured on TMV coated substrate than in cells on TCP [24]. Based on these results, we examined the temporal changes in gene expression involved in early differentiation (*ALPL*, *BMP2* and *IBSP*) for cells cultured on TMV coated substrates, cells supplemented with TMV in solution, and cells cultured on conventional TCP (Figure 1.3). Although there was no significant difference in *ALPL* mRNA expression for cells cultured on the three different substrates after 8 hours, the expression significantly increased after 24 hours in cells cultured on TMV substrate (Figure 1.3 A). However, the increase only exhibit less than two-fold difference over uninduced cells. Since alkaline phosphatase (ALP) is an enzyme that facilitates matrix mineralization and gradually increases over a period of 2 weeks [51], it is possible that the time point of this

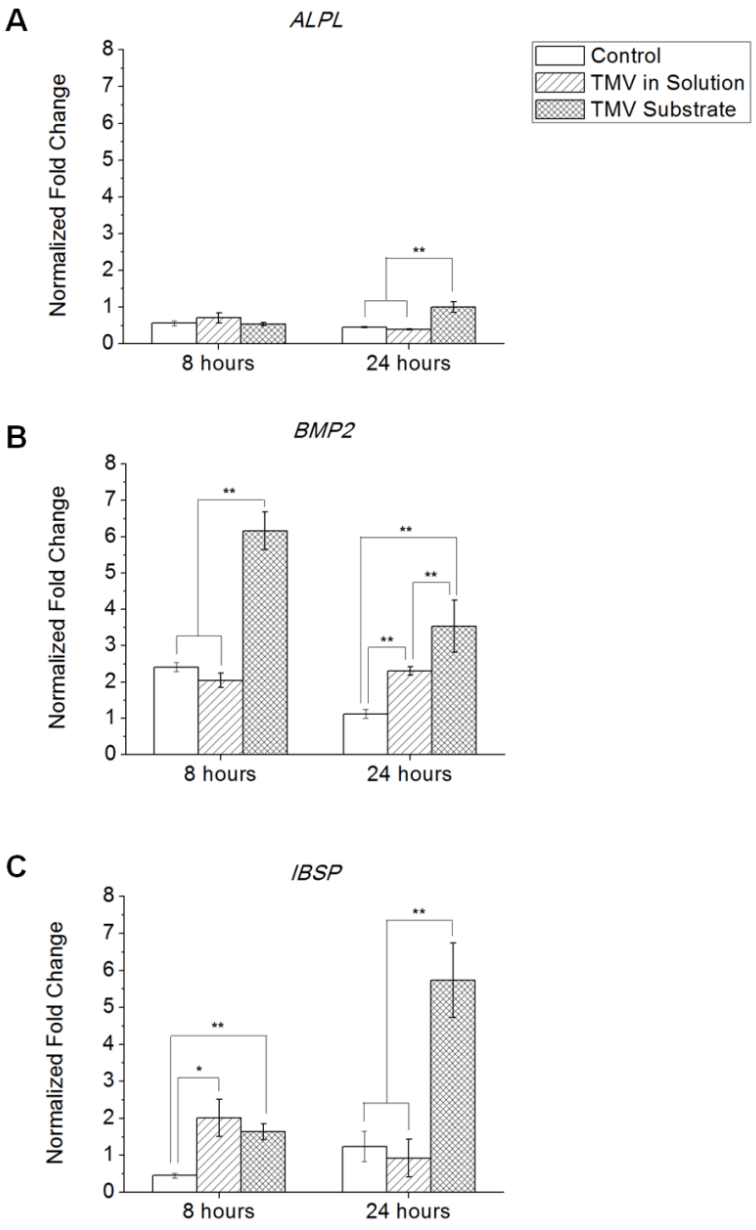

Figure 1.3 RT-qPCR analysis for osteo-specific gene expression of BMSCs under osteogenic conditions. For each growing condition, the profiles showed two time points: 8 and 24 hours after induction with osteogenic media. Gene expression in the cells seeded on TCP, TCP with TMV in solution and TMV substrate under osteogenic conditions. (*A*) *ALPL* expression was upregulated in cells grown on TMV at 24 hours. (*B*) *BMP2* expression at both time points was significantly increased in cells grown on TMV substrates. (*C*) *IBSP* was highly expressed in cells grown on TMV substrates at both time points. In all graphs, the error bars denote ± 1 s.d. (**) and (*) represent $p < 0.05$ and $p < 0.1$, respectively.

study is too early to observe any significant upregulation in *ALPL* mRNA expression. For cells cultured on TMV coated substrates, *BMP2* expression levels were six-fold higher than uninduced cultures after 8 hours of osteoinduction. In comparison, the cells in traditional cultures had only slightly increased *BMP2* gene expression by two- fold (Figure 1.3 B). The initial increase in *BMP2* gene expression for TCP had diminished back to basal level after 24 hours, whereas the cells cultured on TMV coated substrate still maintained higher *BMP2* gene expression levels, a three-fold increase over TCP substrates (Figure 1.3 B). Although the addition of TMV as a solution supplement to the culture media resulted in a modest increase in *BMP2* expression at 24 hours, it failed to provide the same effects as the virus-coated substrates. The initial results with TMV in solution indicate that the coating of the virus to the solid support is necessary to affect early *BMP2* gene expression and the virus itself does not act as a soluble inducer. The results also suggests that TMV coated substrates enhance osteogenic differentiation of BMSCs by increasing *BMP2* mRNA levels.

In addition to increased *BMP2* gene expression, mRNA levels for integrin-binding sialoprotein (*IBSP*), a secreted extracellular matrix protein required for hydroxyapatite formation, increased over time in both TCP and TMV samples. *IBSP* is an osteogenic marker associated with mineralizing tissues [52], hence the increase in *IBSP* gene expression within 24 hours is an important discovery in explaining the role of TMV in osteogenic differentiation [24]. *IBSP* gene expression levels for cells grown on TMV were two-fold higher than those of TCP after 8 hours of osteoinduction and the difference further increased to five-fold after 24 hours (Figure 1.3 C). The addition of

TMV as a solution to the culture media did not provide the similar increase in *IBSP* expression levels as TMV coated substrates (Figure 1.3 C).

The apparent increase in *BMP2* and *IBSP* mRNA levels for the cells on TMV-coated substrates suggest that these two proteins are involved in the enhancement of osteogenic differentiation (Figure 1.3 B, C). The observed differences in gene expression of *BMP2* and *IBSP* indicate that the surface coating with the virus moderates *BMP2* and *IBSP* expression levels within the first day, and the virus itself does not act as a soluble chemical inducer, but rather as a substrate with unique topographical features, or offering a rough surface, at both nanometer and micrometer scales. Such surface features have been observed with M13 bacteriophage and TMV to affect cell directionality and ECM protein deposition [48, 49, 53]. It was demonstrated that nanoscale topography (e.g. roughness) directly influenced cell adhesion leading to altered cellular behaviours including proliferation and differentiation [6, 54, 55].

1.2.3 TMV substrate induces higher localized BMP2 production

The increase in *BMP2* mRNA expression level was corroborated by ELISA, showing a similar trend of BMP2 increase at 8 and 24 hours in osteogenic media (Figure 1.4 A). In comparison to uninduced controls, the cells on TMV coated substrates expressed four-fold and three-fold higher levels of BMP2 at 8 and 24 hours, respectively. For TCP culture, there was no significant increase in BMP2 production at either time points (Figure 1.4 A). Although the addition of TMV in solution showed an increase in *BMP2* mRNA level after 24 hours (Figure 1.3 B), the protein analysis did not validate this temporal increase (Figure 1.4 A). Thus, among the three growth conditions, only TMV

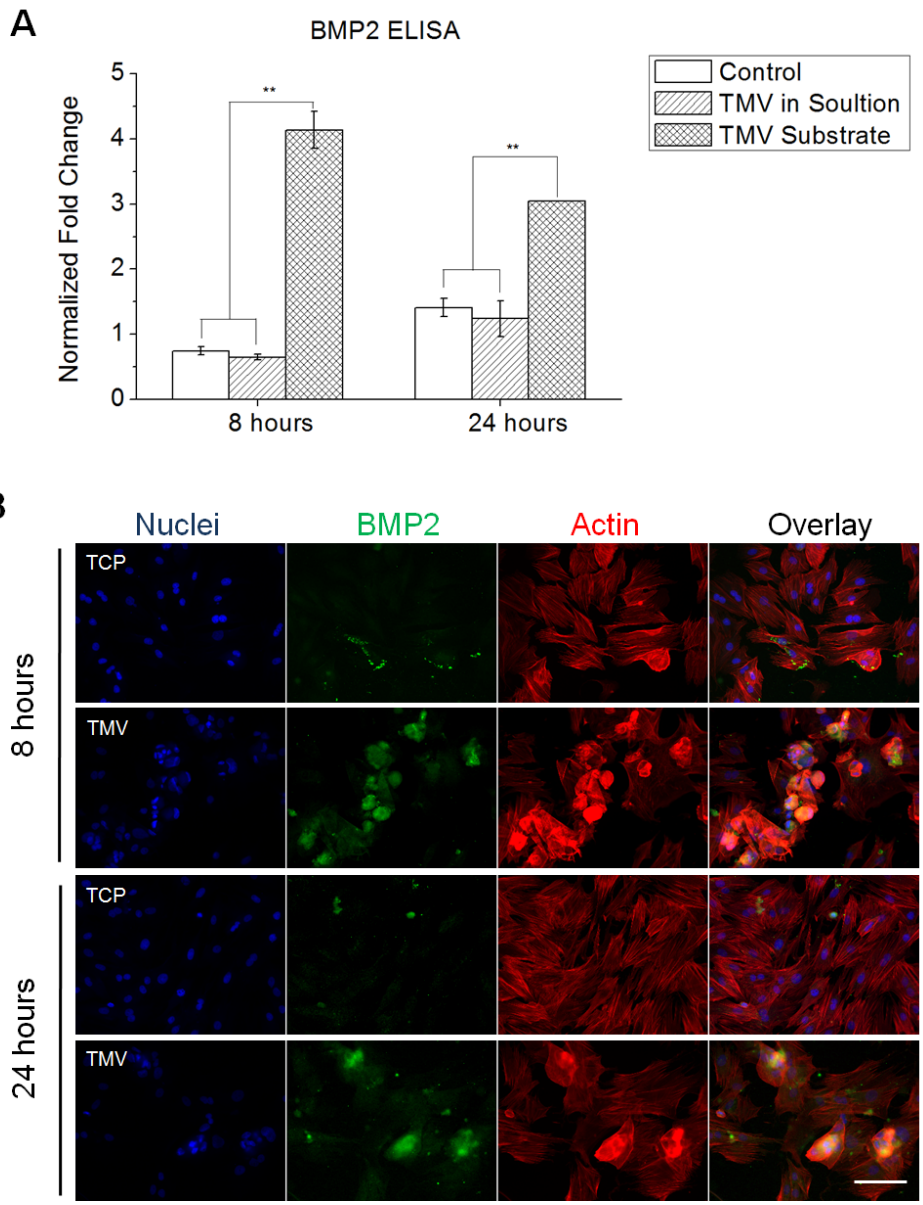

Figure 1.4 Differential expression and localization of BMP2 analyzed by ELISA and immunohistochemical staining. (*A*) Quantification of BMP2 protein expression at 8 and 24 hours normalized to cell number by ELISA. The values are expressed as fold change compared to cells on TCP before osteoinduction. The error bars denote ± 1 s.d. $^{**}p < 0.05$ based on ANOVA. (*B*) Cells on TCP control or TMV substrate were collected at 8 and 24 hours after osteogenic induction. At both time points, cells on TMV-coated surface expressed more BMP2 protein and the protein is highly expressed at cell aggregates. Color representation: nucleus (blue), BMP2 (green), actin (red). Scale bar is 100 μm.

coated surface induced a significant increase in BMP2 mRNA and protein expression after 8 hours of osteogenic induction.

Immunofluorescence imaging for BMP2 revealed that the morphogen is localized to the cell aggregates. As shown in Figure 1.4 B, BMSCs on TMV stained positive for BMP2 with higher fluorescence intensity at both time points. BMP2 was observed around the cells that formed nodules or aggregates. It is hypothesized that too strong substrate binding may inhibit osteogenic differentiation [50]. Similarly to the previous results, the cells with TMV in solution stained poorly for BMP2 (*data not shown*).

The concentrations of secreted BMP2 in conditioned media from the three culture conditions were measured by sandwich based ELISA. Higher concentration of BMP2 was observed in media with cells on TMV substrate, compared to cells on TCP with and without TMV supplemented in the media. The concentrations ranged between 100-200 pg/mL (*data not shown*), which is consistent with that reported in an ultrasound-induced BMP2 secretion within 24 hours [56].

1.2.4 Enhanced osteogenesis requires TMV coating on substrate

The enhancement in bone differentiation was also assessed by measuring ALP activity and calcium deposition at day 7, 14, and 21. ALP is an early marker of osteogenesis and its activity mediates matrix mineralization. Although only minor upregulation of *ALPL* mRNA levels was observed by RT-qPCR after 24 hours, ALP enzyme activity assays over the course of 3 weeks showed significant differences at day 7 and 14 (Figure 1.5 A). Similar to the earlier results, the addition of TMV in solution does not increase ALP activity, and only the cells on TMV coated substrates had significantly higher enzyme

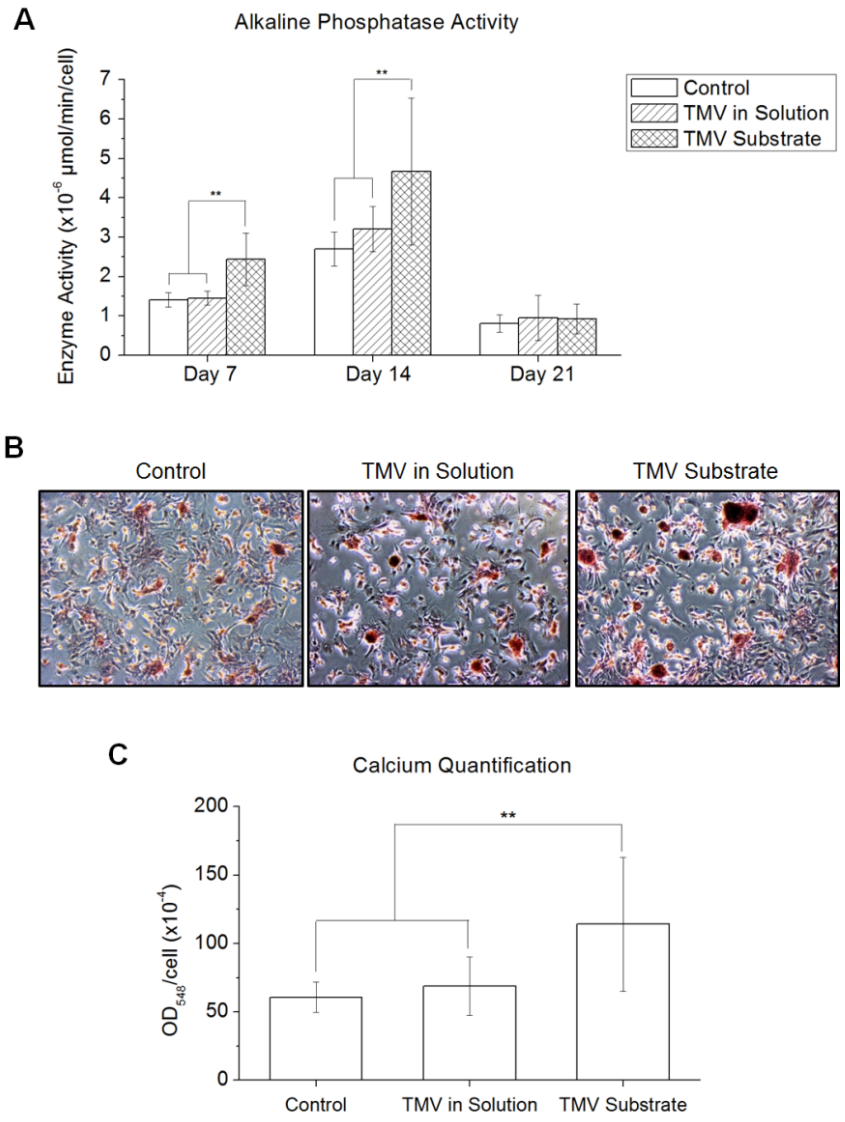

Figure 1.5 Cytochemical analysis of bone differentiation process of BMSCs on TCP, TCP with TMV in media, TMV substrate at 7, 14, and 21 days after osteogenic induction. (*A*) Alkaline phosphatase activity of cells in three different conditions. Cells on TMV substrate have an increase in enzyme activity at day 7 and 14, whereas the addition of TMV solution does not alter the enzyme activity when compared to control. Alkaline phosphatase activity drops to baseline at day 21 for all conditions. (*B*) Alizarin red staining of each sample at day 14. (*C*) Absorbance at 548 nm normalized to cell number to indicate relative amount of calcium deposit at day 14 stained by alizarin red solution. The mineralization of cells on TMV substrate doubles that of TCP and TMV in solution, suggesting an improvement in osteogenesis (** $p < 0.05$ based ANOVA). The error bars denote ± s.d.

activities compared to controls. The enzyme activity at day 21 diminishes to the same level for all samples, suggesting that the observed level may be a basal activity level of ALP during mineralization stage.

Calcium deposition was determined at day 14 by staining with Alizarin Red S. Small nodules of mineralized calcium were observed for controls and cells supplemented with TMV in solution, whereas the nodules were visibly larger for the cells on TMV-coated substrates (Figure 1.5 B). UV-visible absorbance measurements of the extracted dyes indicated the cells on TMV substrate had twice the content of calcium compared to control (Figure 1.5 C). The addition of TMV solution does not enhance matrix mineralization. These results confirm our hypothesis that TMV provides a topographical cue to enhance osteogenic differentiation, likely by changing the surface roughness. The combined results from RT-qPCR, ELISA and immunostaining clearly indicate that BMP2 expression was significantly induced within 24 hours of induction with a peak expression level at 8 hours. The enhancement requires the virus as a substrate rather than as a solution supplement, suggesting the role of topography or surface roughness in TMV-mediated osteogenesis.

1.2.5 Additive effect on BMP2 gene expression

The osteogenic inducing agents that are routinely used for *in vitro* cultures include β-glycerolphosphate, ascorbic acid, and dexamethasone. Individual inducers facilitate differences in the bone differentiation process [51]. To examine which osteogenic inducers are required to induce *BMP2* upregulation in BMSCs grown on TMV substrate, the inducers were individually added to different cell cultures and cells were analyzed

after 8 hours. Within this time frame, *BMP2* expression levels were the same for cells grown on TCP with or without the three osteogenic inducers (Figure 1.6). *BMP2* expression level partially increased for cells grown on TMV coated substrates without any inducers. While the addition of β-glycerolphosphate or L-ascorbic acid 2-phosphate did not upregulate *BMP2* mRNA level, dexamethasone resulted in a significant increase in *BMP2* expression level after 8 hours of osteogenic induction (Figure 1.7).

β-Glycerolphosphate is a phosphate donor for matrix mineralization and in turn increases alkaline phosphatase activity. L-ascorbic acid 2-phosphate, a stable form of vitamin C, is a source for collagen synthesis which is a major component of bone ECM. However, there is no evidence on the direct effect of these two compounds on modulating BMP2 production. On the other hand, dexamethasone, a glucocorticoid derivative, induced a significant increase in *BMP2* expression level in BMSCs on TMV substrates. Bi *et al*. [57] illustrated that the treatment of dexamethasone induced BMP2 expression in BMSCs, resulting in a gradual increase of ALP activity over the first 2 weeks. However, the enhanced effect of dexamethasone on BMP2 expression due to surface roughness has not been reported before. This observed enhancement of BMP2 expression from dexamethasone alone is similar to when all three osteogenic inducers were added to the culture media of cells on TMV wafers (Figure 1.7). Although there is a chance that TMV could act as a carrier for dexamethasone internalization, the fact that TMV supplemented media did not enhance BMP2 expression and osteogenesis, eliminates this possibility. This clearly highlights the ability of TMV nanosurface in the presence of dexamethasone to promote osteogenesis.

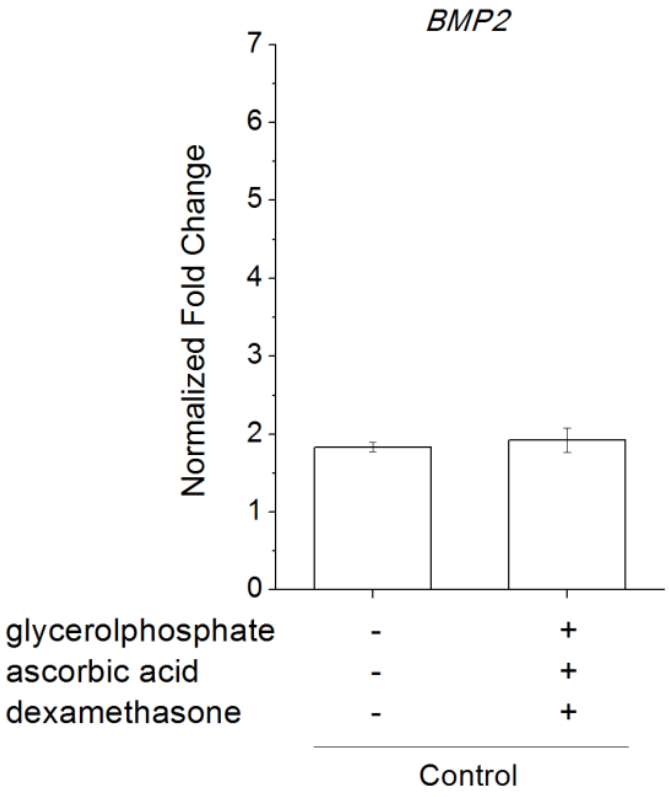

Figure 1.6 RT-qPCR analysis for *BMP2* expression in the cells seeded on TCP control with or without the three osteogenic inducers for 8 hours. The osteogenic inducers are sodium β-glycerolphosphate, L-ascorbic acid 2-phosphate and dexamethasone. No significant difference in *BMP2* gene expression was observed. The error bars denote ± s.d.

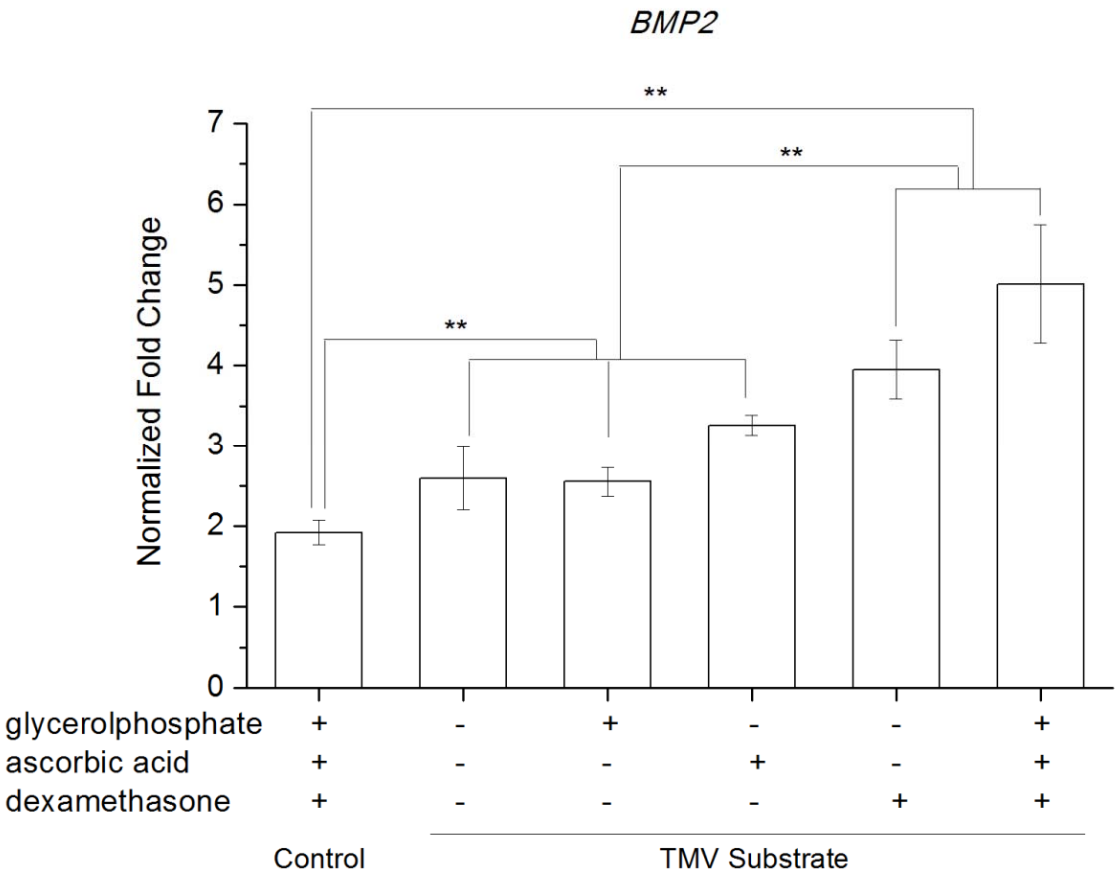

Figure 1.7 RT-qPCR analysis for *BMP2* expression in the cells seeded on TCP control and TMV substrate under individual osteogenic inducers for 8 hours. The osteogenic inducers are sodium β-glycerolphosphate, L-ascorbic acid 2-phosphate and dexamethasone. The addition of all three inducing agents resulted in the highest level of BMP2 mRNA. The error bars denote ± s.d. and (**) represents $p < 0.05$

To determine if the TMV coating concentrates and immobilizes the chemical inducers to the surface, Quartz Crystal Microbalance with Dissipation (QCM-D) was used to monitor the deposition of each inducer on TMV-coated substrate. As shown in Figure 1.8, there is no significant shift in the resonance frequency of the electrode, which indicates no measurable surface deposition of the osteogenic inducers. While effects of dexamethasone and TMV-coating appear to converge on early BMP2 expression, the initial assessment with QCM-D and the previous TMV solution supplement studies suggest that TMV and dexamethasone do not interact with each other (Figure 1.8). Furthermore, the virus-coating alone appeared to affect BMP2 expression, which suggests that an alternative regulatory mechanism may be involved.

1.2.6 TMV coating alters cytokine expression

Several other cytokines apart from BMP2 regulate bone remodelling [58-63]. Specifically, inflammatory cytokines from T-cell conditioned media, including TNF-α, IFN-γ, IL-1, IL-17, were shown to induce BMP2 expression [64]. In another study, IL-6, IL-8, monocyte chemotactic protein 1 (MCP-1), macrophage inflammatory protein 1 alpha (MIP-1α), MIP-3α were shown to be involved in fibroblast growth factor-2 (FGF2)-mediated osteogenesis [61] . There is also an evidence that the addition of chemokine (C-X-C motif) ligand (CXCL) 12 enhanced BMP2-induced differentiation [65]. We therefore investigated the cells' response to the virus by screening such cytokines or other relevant growth factors which could affect early bone differentiation. Cytokine antibody arrays for 29 cytokines were used to screen the conditioned media from cells cultured on TCP and TMV coated wafers. The media consisting of primary

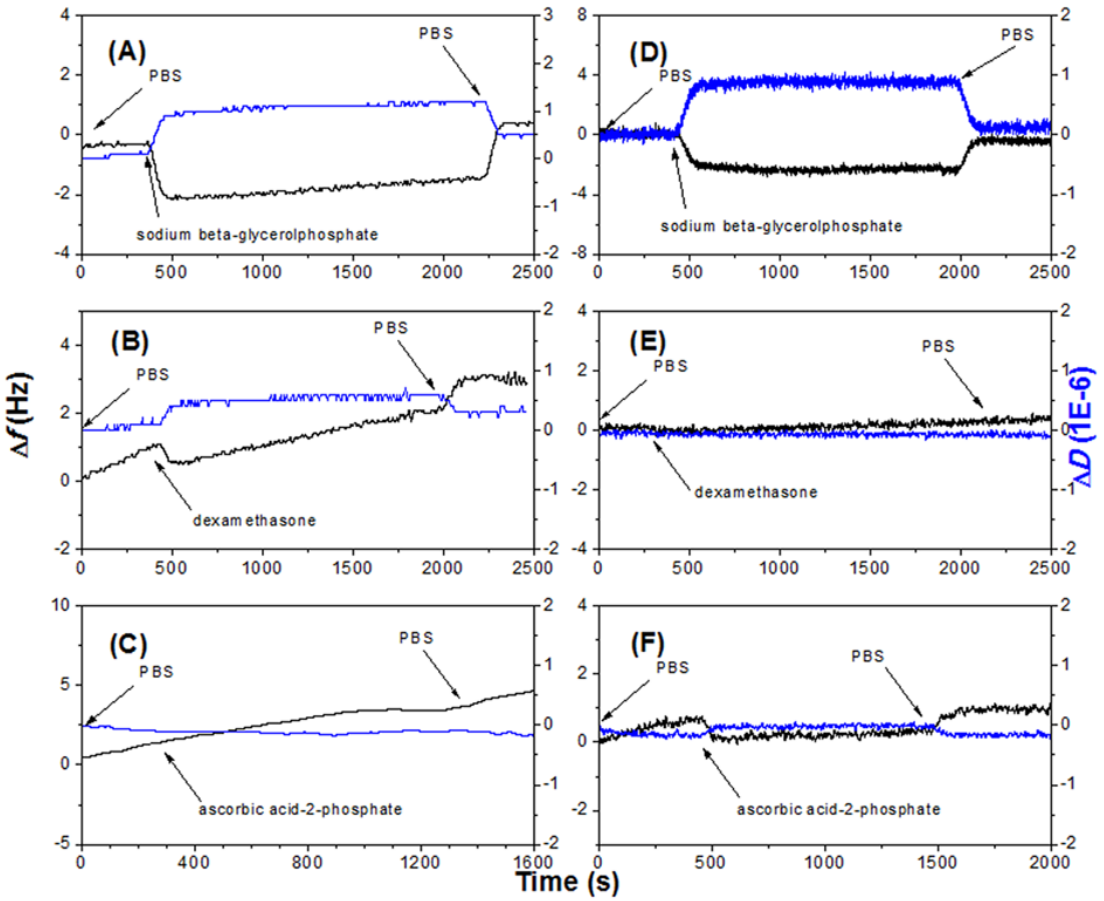

Figure 1.8 QCM-D results showing changes in the third harmonic frequency (Δ*f)* and dissipation (ΔD) when delivering (***A***) 10 mM of sodium β-glycerolphosphate, (***B***) 10 nM of dexamethasone, (***C***) 50 μg/mL of ascorbic acid-2-phosphate to TMV-coated gold surface, and when delivering (***D***) 10 mM of sodium β-glycerolphosphate, (***E***) 10 nM of dexamethasone, (***F***) 50 μg/mL of ascorbic acid-2-phosphate to uncoated gold surface. No significant deposition can be seen at all conditions.

media only was collected after 24 hours of culture and examined. Tissue inhibitor of metalloproteinases-1 (TIMP-1) was the only molecule secreted from both culture conditions, while cytokine-induced neutrophil chemoattractant 1 (CINC-1), CINC-2, MIP-3α, and vascular endothelial growth factor (VEGF) were detected from the conditioned media for the cells on TMV wafers (Figure 1.9). According to Kim *et al.* [61], CINC-1 and MIP-3α recruit neutrophils and monocytes to induce osteogenesis. However, the previous studies did not correlate these cytokines with enhanced BMP2 upregulation during osteogenesis. Future studies on the osteogenic effects of these individual cytokines may reveal their involvement in BMP2-mediated bone differentiation. It could possibly lead to a discovery of new biomaterials to elicit these cytokine productions in order to improve bone healing.

The remaining 24 cytokines, CINC-3, ciliary neurotrophic factor (CNTF), fractalkine, GM-CSF, sICAM-1, IFN-γ, IL-1α, -1β, -1ra, -2, -3, -4, -6,-10, -13, -17, IP-10, lipopolysaccharide induced c-x-c chemokine (LIX), L-selectin, monokine induced by gamma interferon (MIG), MIP-1α, RANTES, thymus chemokine and TNF-α were below the detection limits of the cytokine array.

1.2.7 Actin depolymerization for cells on TMV substrates

Since there was no established direct correlation of other cytokines and osteogenesis, cell morphologies were closely observed prior to osteoinduction. It was demonstrated that BMP2 production was highly localized around the cell nodules (Figure 1.4 B). Some reports illustrated that culture materials modulate bone differentiation through cytoskeleton organization [66, 67]. The investigation of actin polymerization and

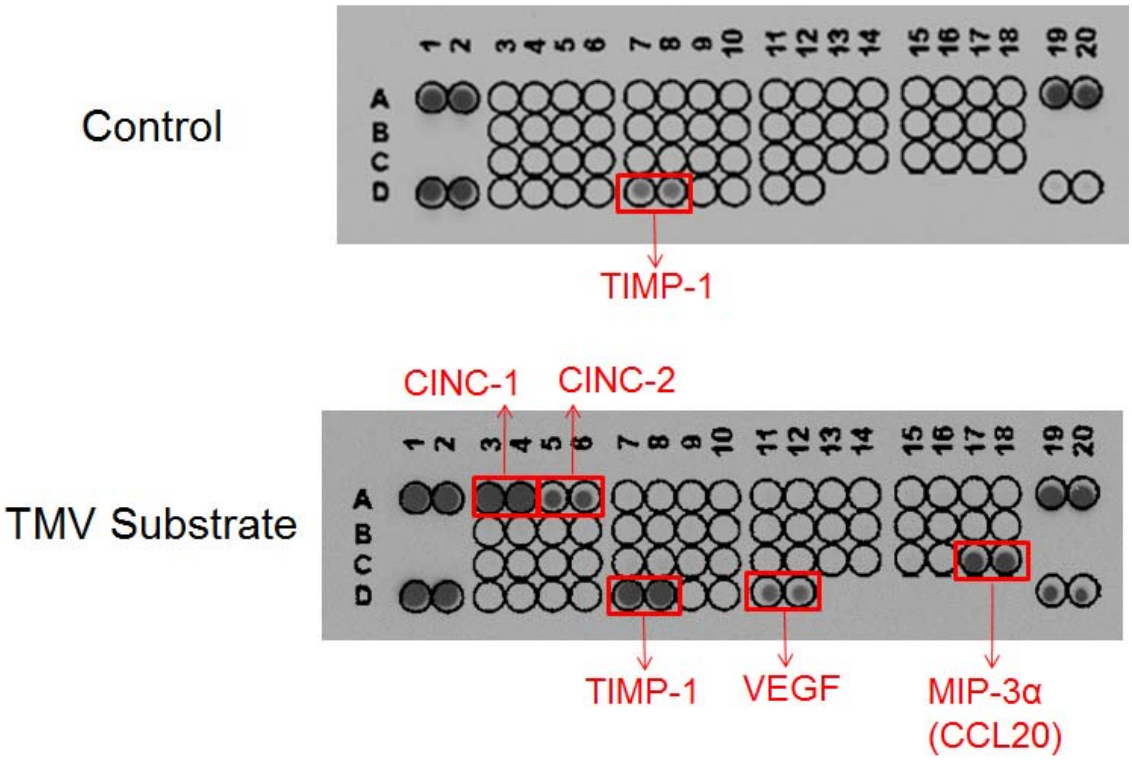

Figure 1.9 Comparison of cytokine profiles in culture media of BMSCs on TCP control and TMV substrate for 24 hours, prior to osteoinduction. An antibody array containing 29 different cytokines was used to compare protein profiles produced by cells on different substrates. TIMP-1 was detected in both cultures with higher levels from TMV substrate. However, the productions of some cytokines and growth factors were induced only by TMV-coated wafer, including CINC-1, CINC-2, MIP-3α, and VEGF.

organization was carried out to compare cells on TCP and TMV substrates prior to osteoinduction, at which time cell aggregation was first observed. The actin intensity by phalloidin staining was more intense in cells on TMV substrate, indicating higher activity from actin polymerization which could facilitate mobilization of cells to form nodules within 24 hours of cell seeding (Figure 1.10). At higher magnification, cells on TCP surface maintained highly aligned sarcomeric striations, whereas cells on TMV substrate displayed nonaligned striations. These observations are similar to an experiment by Mendonça *et al*. [50], which demonstrated that cells on a rougher surface topography exhibit an undefined long axis with thicker actin filaments leading to less initial cell spreading followed by enhanced mineralization.

1.2.8 Reduced focal adhesion size

The interaction between cell and ECM is mediated by cell surface receptors (i.e. integrins) [68]. Vinculins, part of focal adhesion complexes (FACs), couple the integrins to the cytoskeleton allowing crosstalk between ECM and intracellular signalling [69]. Biggs *et al.* highlighted the effects of nanogrooves mediating osteoblastic functions by regulating focal adhesions and subsequent intracellular molecular events.[6] There are other reports showing that integrin-mediated focal adhesion is an important regulator for osteogenesis [70, 71]. Previous studies illustrated that increased localization of vinculin is associated with larger focal adhesion (FA) size and strengthening of adhesion leading to reduced cell motility [69, 72]. Smaller size of FAs suggests that BMSCs attached to TMV substrate weakly, whereas the larger size of FACs dictates stronger cell-substrate adhesion [73]. While BMSCs on standard TCP exhibited larger average vinculin size,

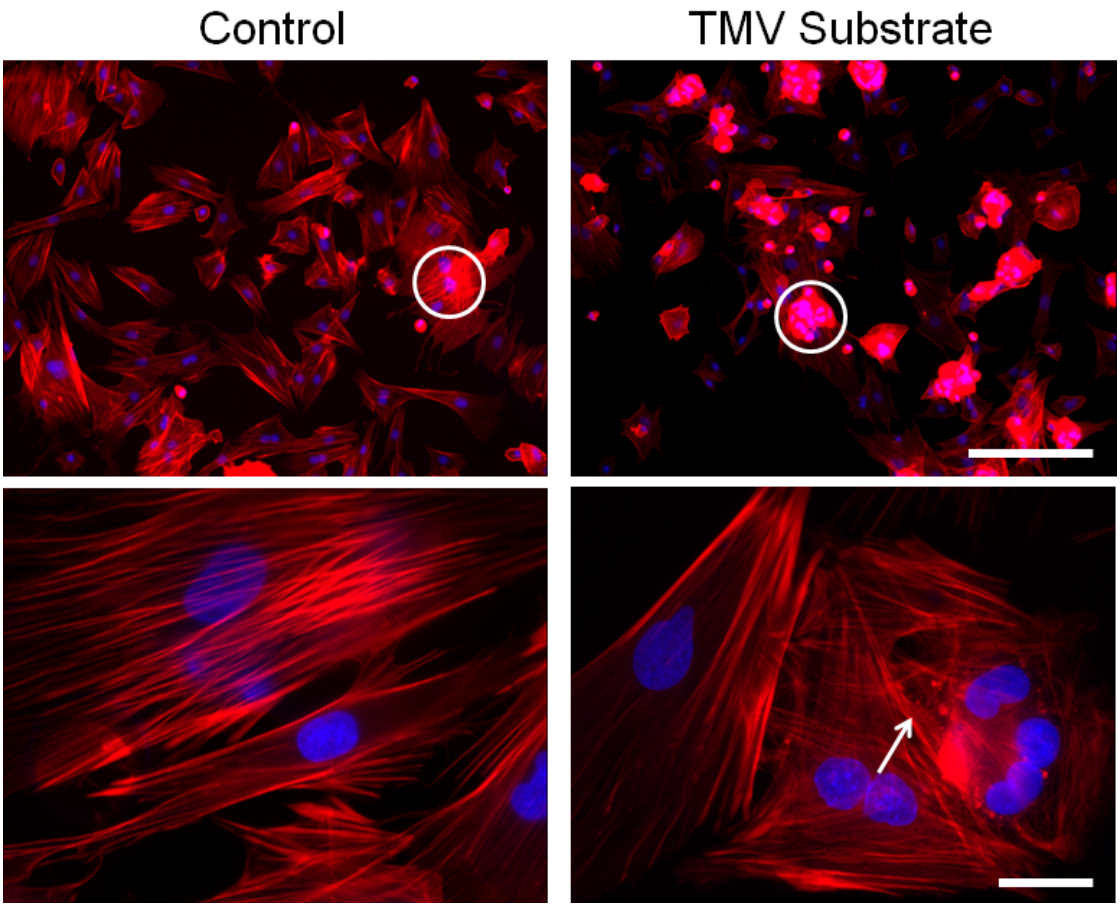

Figure 1.10 Cytoskeleton immunochemical staining showing actin polymerization and organization of cells on TCP control and TMV substrate after 24 hours seeding, prior to osteoinduction, at low- (top row) and high-magnification (bottom row). Similar fibrous cytoskeleton organization was observed where cells spread out in both cell cultures. However, in cell aggregates on TMV substrate the actin intensity was higher (white circles) and well-defined actin filament was absent (white arrow). Color representation: nucleus (blue), actin (red). Scale bars are 200 μm for top row and 25 μm for bottom row.

indicating stronger adhesion to the underlying substrate, the cells on TMV substrate showed smaller FA sizes (Figure 1.11 A, B). The significantly smaller FA size for cells on TMV substrates is likely to increase cell motility and facilitate the formation of cell aggregates within 24 hours of seeding. Further studies are necessary to establish the correlation of the focal adhesion of BMSCs on virus-coated substrates with the downstream responses.

1.3 CONCLUSION

Early morphological differences were documented for cells seeded on TMV-coated substrates, wherein the cells often aggregated and spread poorly. The highest BMP2 mRNA and protein levels was detected in cells cultured on TMV-coated substrates after 8 hours of osteoinduction and maintained high levels of *BMP2* mRNA and protein levels even after 24 hours. To eliminate the possibility that the virus may act as a soluble inducer, the virus was supplemented in the media as a solution, however this approach did not afford the same enhancement as the immobilized virus substrate. BMP2 was localized to the cell aggregates, which are only present on cells cultured on TMV coated substrates. Decoupling the three osteogenic agents (dexamethasone, β-glycerophosphate, and ascorbic acid) suggests that TMV coating enhances the effect of dexamethasone, but TMV coating alone was sufficient to induce BMP2 gene expression. Screening the media for cytokines revealed the presence of CINC-1, CINC-2, MIP-3α, and VEGF. The surface topography from TMV coating disrupted actin alignment and reduced FA size. The smaller FA indicates a weaker cell-substrate interaction on TMV substrates. The results suggest that TMV substrate promotes cell aggregation and induces an early onset

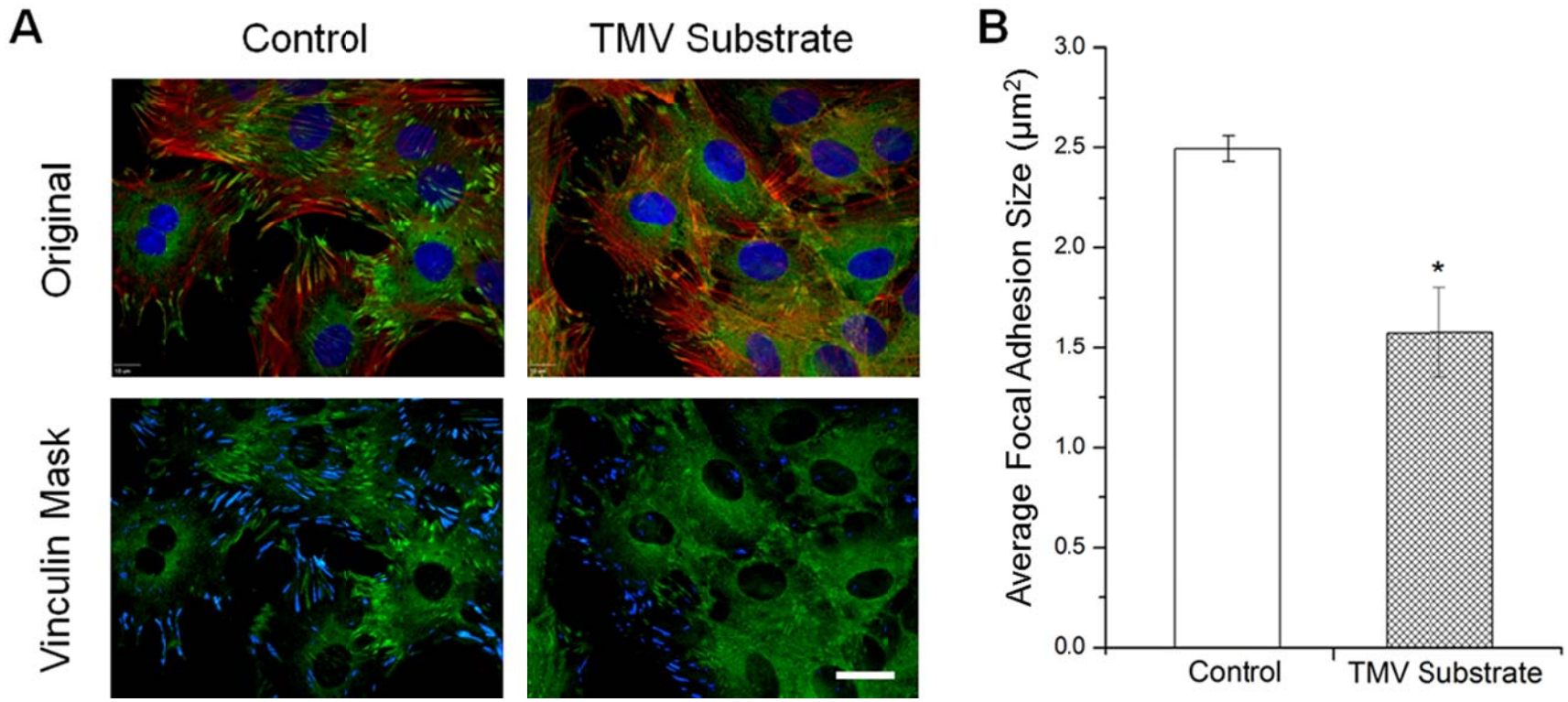

Figure 1.11 Immunochemical staining showing the difference in vinculin size of cells on TCP control or TMV substrate for 24 hours. (*A*) Immunofluorescence images of cells on different substrates for 24 hours prior to osteoinduction (top panel). Color representation: nucleus (blue), vinculin (green), phalloidin (red). The bottom panel illustrates vinculin masking and selection for size analysis. The selected vinculin spots as part of focal adhesion complex are highlighted in blue. (*B*) Average vinculin size of cells on either TCP or TMV-coated surface. The error bars denote ± 1 s.d. and * $p < 0.05$ based on equal variance two-tailed Student t-test.

BMP2 expression.

Although extensive studies with BMP2 show potent osteoinductive effects at early time points, additional studies involving BMP2 knockdown by siRNA and BMP2 antagonist, noggin, will be necessary to eliminate other possible factors involved in TMV-mediated osteogenesis. Further investigation into other early cell-material and secreted protein-material interactions is necessary to gain a better understanding of how the TMV coating can promote the endogenous production of BMP2. The regulation of endogenous BMP2 expression will be critical for advanced biomaterial development in bone tissue engineering applications.

1.4 EXPERIMENTAL SECTION

1.4.1 TMV Isolation

TMV was isolated and purified according to a protocol previously reported [24, 26].

1.4.2 Preparation of TMV coated substrates

For imaging experiments, 22x22 cm glass coverslips (VWR) were cleaned by piranha solution (7:3 mixture of 98% H_2SO_4 and 30% H_2O_2) at 75 °C for 2 hours, followed by three washes with water (Millipore Synergy UV system, 18.2 MΩ) and sonication. The dry glass coverslips were immersed in 1% (v/v) of 3-aminopropyltriethoxysilane (APTES) in ethanol for 10 minutes and washed thoroughly with ethanol to remove excess APTES. After drying with nitrogen, APTES coating was crosslinked at 160°C in a vacuum oven for 1 hour. The wafers were dried and flushed with nitrogen gas for complete drying. For gene expression experiments, APTES coated slides (Lab Scientific

Inc.) were cut into 1.5 cm^2 wafers. Both coverslips and slide wafers were sterilized with ethanol before use. For TMV coating, the wafers and coverslips were coated with 0.2 mg/mL TMV solution diluted in water and the coated substrates were dried overnight in a sterile biosafety cabinet. The virus coverage on the wafers was characterized using tapping-mode AFM images using a NanoScope IIIA MultiMode AFM (Veeco). Si tips with a resonance frequency of approximately 300 kHz, a spring constant of about 40 N m^{-1} and a scan rate of 0.5 Hz were used.

1.4.3 BMSC isolation and expansion

Primary BMSCs were isolated from the bone marrow of young adult 80 g male Wister rats (Harlan Sprague Dawley, Inc.). The procedures were performed in accordance with the guidelines for animal experimentation by the Institutional Animal Care and Use Committee, School of Medicine, University of South Carolina. Cells were maintained in growth medium (DMEM supplemented with 10% fetal bovine serum (FBS), penicillin (100 U/mL), streptomycin (100 μg/mL) and amphotericin B (250 ng/mL)) and passaged no more than four times after isolation. To induce osteogenesis, growth media was replaced with osteogenic media consisting of DMEM supplemented with 10% FBS, penicillin (100 u/mL), streptomycin (100 μg/mL), amphotericin B (250 ng/mL), 10 mM sodium β-glycerolphosphate, L-ascorbic acid 2-phosphate (50 μg/mL) and 10^{-8} M dexamethasone. Media was replenished every 3-4 days.

1.4.4 Quantitative real-time RT-PCR analysis (RT-qPCR)

TMV coated wafers were seeded with 4.5 X 10^4 cells per wafer and allowed to attach overnight in growth media. The media is replaced with osteogenic media and cultured for 8 and 24 hours. In addition, BMSCs with similar density were seeded on 3.8 cm^2 tissue culture plastic (TCP), with or without TMV in the osteogenic media, for the above mentioned time periods. Furthermore, to determine which osteogenic components are required to enhance osteogenesis on TMV-coated wafers, BMSCs on TMV substrates were cultured in basal media with each osteogenic inducing agent for 8 hours. The cell cultures were terminated at this time point and total RNA was subsequently extracted using (RNeasy mini purification kit, Qiagen). The number of samples for each experiment (n) was two and each experiment was repeated (N) three times.

The quality and quantity of the extracted RNA was analyzed using Bio-Rad Experion (Bio-Rad Laboratories) and was reverse transcribed by using qScript™ cDNA Supermix (Quanta Biosciences). RT-qPCR (iQ5 real-time PCR detection system Bio-Rad Laboratories) was done by the method described as: 60 cycles of PCR (95˚C for 20s, 58˚C for 15 s, and 72˚C for 15s), after initial denaturation step of 5 minutes at 95˚C, by using 12.5 µL of iQ5 SYBR Green I Supermix, 2 pmol/µL of each forward and reverse primers and 0.5 µL cDNA templates in a final reaction volume of 25 µL. Glyceraldehyde 3-phosphate dehydrogenase (GAPDH) was used as the housekeeping gene. Data collection was enabled at 72˚C in each cycle and C_T (threshold cycle) values were calculated using the iQ5 optical system software version 2.1. The expression levels of differentiated genes and undifferentiated genes were calculated using Pfaffl's method (M.W. Pfaffl, G.W. Horgan and L. Dempfle, Relative expression software tool) for

group-wise comparison and statistical analysis of relative expression results in real-time PCR, using GAPDH as the reference gene. Quantification of gene expression was based on the C_T value for each sample which was calculated as the average of three replicate measurements for each sample analyzed. "Pair Wise Fixed Reallocation Randomization Test" was performed on each sample and a value of $p < 0.05$ was regarded as significant. The primers used for RT-qPCR are shown in Table 1.1. The primers were synthesized commercially (Integrated DNA Technologies, Inc.), and evaluated for an annealing temperature of 58˚C.

1.4.5 Cytochemical staining and quantification

For cytochemical staining, 4.5×10^4 cells were seeded on TMV coated wafers and allowed to attach overnight in basal media. The media was replaced after 24 hours of culture with osteogenic media and cultured for an additional 7, 14, and 21 days. As controls, BMSCs were seeded on 3.8 cm^2 TCP at similar densities for the same time periods. CellTiter Blue® assay (Promega) was used to determine number of cells in each sample one hour prior to cell fixation. The cells were fixed with 4% paraformaldehyde for 15 minutes at room temperature. To determine ALP activity, each fixed samples were incubated in 500 µL of 1-Step *p*-nitrophenyl phosphate solution (Thermo Scientific) for 15 minutes at room temperature. Then the solution was transferred to a new microfuge tube with 250 µL of 2 N NaOH to stop the reaction and the absorbance at 405 nm was measured. The number of samples for each experiment (n) was three and each experiment was repeated (N) two times.

Table 1.1 Primers used for RT-qPCR to measure gene expression levels. ALPL: alkaline phosphatase; BMP2: bone morphogenetic protein 2; IBSP: integrin-binding sialoprotein.

Gene	Sequence (5'-3')
ALPL	Forward: ACCTCGAGCAGGAACAGAAGTTTGCT
	Reverse: TTCCATGATGGTTGCAGGGTCTGGA
BMP2	Forward: ACCAACCATGGGTTTGTGGTGGAAGT
	Reverse: TCCGCTGTTTGTGTTTGGCTTGACG
GAPDH	Forward: ACTAAAGGGCATCCTGGGCTACACTGA
	Reverse: TGGGTGGTCCAGGGTTTCTTACTCCTT
IBSP	Forward: TCTGAACGGGTTTCAGCAGACGA
	Reverse: GCCATGCCCCTTGTAGTAGCTGTA

To compare calcium deposition, fixed samples at day 14 were stained with 0.1% Alizarin red solution (Sigma-Aldrich) pH 4.1-4.5 for 30 minutes. Since the reaction was highly light sensitive, the substrates were wrapped in aluminium foil during the Alizarin red staining. After washing with ultrapure water, 200 µL of 0.1N NaOH was added to each sample to extract the dye from the sample. The amount of dye was quantified by measuring absorbance at 548 nm wavelength. Both absorbance values at 405 nm and 548 nm were normalized against cell number from CellTiter Blue® standard curve. The number of samples for each experiment (n) was three and each experiment was repeated (N) two times.

1.4.6 Enzyme-linked immunosorbent assay (ELISA)

In order to validate RT-qPCR gene expression at protein expression level, TMV coated coverslips and uncoated coverslips were seeded with 1.0 X 10^5 cells per piece. 40 µg of TMV was added to each TMV-in-solution culture. The cultures were terminated at 8 and 24 hours after osteo-induction. CellTiter Blue® (Promega) was used to determine cell number in each sample one hour prior to cell fixation with 4% paraformaldehyde. Each of the samples was then permeabilized with 0.1% Triton-X 100 for 15 minutes and blocked in 1.5% bovine serum albumin (BSA, Sigma-Aldrich) in PBS for 1 hour at room temperature. After blocking, the cells were incubated overnight with mouse monoclonal antibody targeting BMP2 (R&D systems) at 1:100 dilution in blocking buffer. Secondary goat anti-mouse antibody conjugated with horseradish peroxidase (Cayman Chemical) was used at 1:1000 dilution for 2 hours at room temperature. After washing, 1 mL of 3,3',5,5'-tetramethylbenzidine (TMB) solution prepared from TMB ready-to-use tablet

(Amresco) was added to each sample, incubating on a rocker for 30 minutes at room temperature. The reaction was stopped by adding 500 μL of 2.0 M H_2SO_4. Absorbance at 450 nm wavelength was measured and then normalized against cell number. Protein expressions are shown as fold change relative to cells cultured on TCP without osteo-induction. The number of samples for each experiment (n) was three and each experiment was repeated (N) two times.

1.4.7 Immunofluorescence assays and image analysis

The localization of endogenously expressed BMP2 was examined by immunohistochemical staining. TMV coated coverslips and uncoated coverslips were seeded with 1.0 X 10^5 cells per piece. The cultures were terminated at 8 and 24 hours after osteo-induction. Cells were fixed in 4% paraformaldehyde at room temperature for 30 minutes. Each of the samples was then permeabilized with 0.1% Triton-X 100 for 15 minutes and blocked in 1.5% bovine serum albumin (BSA, Sigma-Aldrich) in PBS for 1 hour at room temperature. After blocking, the cells were incubated overnight with mouse monoclonal antibody targeting BMP2 (R&D Systems) at 1:100 dilution in blocking buffer. Secondary goat anti-mouse antibody conjugated with fluorescein (Chemicon) was used at 1:100 dilution for 2 hours at room temperature. Rhodamine-phalloidin (1:100 in PBS) was used to stain filamentous actin. Nuclei were stained with DAPI (4, 6-diamidino-2-phenylindole, 100 ng/mL). The samples were then mounted and sealed with clear nail polish before imaging. Images of the stained substrates were taken on Olympus IX81 fluorescent microscopy.

For imaging of actin structure and focal adhesion associated protein, vinculin, uncoated coverslips and TMV coated coverslips were seeded with 1.0×10^5 cells each. Cultures were terminated 24 hours after seeding in basal media. The samples were fixed, permeabilized, and blocked as described above. Cells were incubated with anti-vinculin mouse monoclonal antibody (Neomarkers) at 1:200 dilution in blocking buffer. Secondary goat anti-mouse antibody conjugated with fluorescein (Chemicon) was used at 1:100 dilutions for 2 hours at room temperature. Rhodamine-phalloidin (1:100 in PBS) was used to stain actin. Nuclei were stained with DAPI, and the samples were mounted and sealed with clear nail polish before imaging.

SlideBook™ 5 was used to select and analyze immunofluorescence images of vinculin. After setting the threshold for masks, the criteria used to select vinculin spots to be analyzed were XY shape factor larger than 1.5 and area size between 0.5-15 μm. The average size of vinculin for each image was calculated, followed by the calculation of average vinculin size of cells on TCP and TMV substrate and the standard deviation from average values of three individual images.

1.4.8 Statistics/data analysis

Data were expressed as mean ± standard deviation (s.d.) of the measured values for cytochemical staining quantification and ELISA. Data were analysed by ANOVA for multiple comparisons, and a post hoc test for group to group comparisons, with $p < 0.05$ considered statistically significant.

1.4.9 Cytokine array

Rat Cytokine Antibody Array (R&D Systems) was used according to the manufacturer's instructions. Culture media were collected at 24 hours after cell seeding on TCP control and TMV-coated glass. Briefly, membranes were blocked for 1 hour followed by overnight incubation at 4 °C in 1 mL of cell culture media pre-incubated with provided detection antibody cocktail. After washing, the membranes were incubated with horseradish peroxidase-conjugated streptavidin for 30 minutes. Signals were developed with Pierce ECL Western Blotting Substrate (Thermo Scientific) and detected on CL-XPosure Film (Thermo Scientific).

1.5 REFERENCES

[1] Ayres CE, Jha BS, Sell SA, Bowlin GL, Simpson DG. Nanotechnology in the design of soft tissue scaffolds: innovations in structure and function. Wiley Interdiscip Rev Nanomed Nanobiotechnol. 2010;2:20-34.

[2] Discher DE, Mooney DJ, Zandstra PW. Growth Factors, Matrices, and Forces Combine and Control Stem Cells. Science. 2009;324:1673-7.

[3] Dvir T, Timko BP, Kohane DS, Langer R. Nanotechnological strategies for engineering complex tissues. Nat Nanotechnol. 2011;6:13-22.

[4] Hynes RO. The extracellular matrix: not just pretty fibrils. Science. 2009;326:1216-9.

[5] Biggs MJP, Richards RG, McFarlane S, Wilkinson CDW, Oreffo ROC, Dalby MJ. Adhesion formation of primary human osteoblasts and the functional response of mesenchymal stem cells to 330-nm deep microgrooves. J R Soc Interface. 2008;5:1231-42.

[6] Biggs MJP, Richards RG, Gadegaard N, McMurray RJ, Affrossman S, Wilkinson CDW, et al. Interactions with nanoscale topography: Adhesion quantification and signal transduction in cells of osteogenic and multipotent lineage. J Biomed Mater Res Part A. 2009;91A:195-208.

[7] Lipski AM, Jaquiery C, Choi H, Eberli D, Stevens M, Martin I, et al. Nanoscale Engineering of Biomaterial Surfaces. Adv Mater. 2007;19:553-7.

[8] Lohmann CH, Sagun R, Sylvia VL, Cochran DL, Dean DD, Boyan BD, et al. Surface roughness modulates the response of MG63 osteoblast-like cells to 1,25-(OH)(2)D-3 through regulation of phospholipase A(2) activity and activation of protein kinase A. J Biomed Mater Res. 1999;47:139-51.

[9] Lovmand J, Justesen J, Foss M, Lauridsen RH, Lovmand M, Modin C, et al. The use of combinatorial topographical libraries for the screening of enhanced osteogenic expression and mineralization. Biomaterials. 2009;30:2015-22.

[10] Martin JY, Schwartz Z, Hummert TW, Schraub DM, Simpson J, Lankford J, et al. Effect of titanium surface roughness on proliferation, differentiation, and protein synthesis of human osteoblast-like cells (MG63). J Biomed Mater Res. 1995;29:389-401.

[11] McNamara LE, McMurray RJ, Biggs MJP, Kantawong F, Oreffo ROC, Dalby MJ. Nanotopographical control of stem cell differentiation. J Tissue Eng. 2010;1:1-13.

[12] Park J, Bauer S, Schlegel KA, Neukam FW, von der Mark K, Schmuki P. TiO_2 nanotube surfaces: 15 nm—an optimal length scale of surface topography for cell adhesion and differentiation. Small. 2009;5:666-71.

[13] Park J, Bauer S, von der Mark K, Schmuki P. Nanosize and vitality: TiO_2 nanotube diameter directs cell fate. Nano Lett. 2007;7:1686-91.

[14] Schwartz Z, Martin JY, Dean DD, Simpson J, Cochran DL, Boyan BD. Effect of titanium surface roughness on chondrocyte proliferation, matrix production, and differentiation depends on the state of cell maturation. J Biomed Mater Res. 1996;30:145-55.

[15] Jiang Y, Jahagirdar BN, Reinhardt RL, Schwartz RE, Keene CD, Ortiz-Gonzalez XR, et al. Pluripotency of mesenchymal stem cells derived from adult marrow. Nature. 2002;418:41-9.

[16] Minguell JJ, Erices A, Conget P. Mesenchymal stem cells. Exp Biol Med (Maywood). 2001;226:507-20.

[17] Pittenger MF, Mackay AM, Beck SC, Jaiswal RK, Douglas R, Mosca JD, et al. Multilineage potential of adult human mesenchymal stem cells. Science. 1999;284:143-7.

[18] Si YL, Zhao YL, Hao HJ, Fu XB, Han WD. MSCs: Biological characteristics, clinical applications and their outstanding concerns. Ageing Res Rev. 2011;10:93-103.

[19] Mackay AM, Beck SC, Murphy JM, Barry FP, Chichester CO, Pittenger MF. Chondrogenic differentiation of cultured human mesenchymal stem cells from marrow. Tissue Eng. 1998;4:415-28.

[20] Drost AC, Weng S, Feil G, Schafer J, Baumann S, Kanz L, et al. In vitro myogenic differentiation of human bone marrow-derived mesenchymal stem cells as a

potential treatment for urethral sphincter muscle repair. Ann N Y Acad Sci. 2009;1176:135-43.

[21] Oswald J, Boxberger S, Jorgensen B, Feldmann S, Ehninger G, Bornhauser M, et al. Mesenchymal stem cells can be differentiated into endothelial cells in vitro. Stem Cells. 2004;22:377-84.

[22] Gong Z, Calkins G, Cheng EC, Krause D, Niklason LE. Influence of culture medium on smooth muscle cell differentiation from human bone marrow-derived mesenchymal stem cells. Tissue Eng Part A. 2009;15:319-30.

[23] Porada CD, Almeida-Porada G. Mesenchymal stem cells as therapeutics and vehicles for gene and drug delivery. Adv Drug Deliv Rev. 2010;62:1156-66.

[24] Kaur G, Valarmathi MT, Potts JD, Jabbari E, Sabo-Attwood T, Wang Q. Regulation of osteogenic differentiation of rat bone marrow stromal cells on 2D nanorod substrates. Biomaterials. 2010;31:1732-41.

[25] Kaur G, Valarmathi MT, Potts JD, Wang Q. The promotion of osteoblastic differentiation of rat bone marrow stromal cells by a polyvalent plant mosaic virus. Biomaterials. 2008;29:4074-81.

[26] Kaur G, Wang C, Sun J, Wang Q. The synergistic effects of multivalent ligand display and nanotopography on osteogenic differentiation of rat bone marrow stem cells. Biomaterials. 2010;31:5813-24.

[27] Rosen V. BMP2 signaling in bone development and repair. Cytokine Growth Factor Rev. 2009;20:475-80.

[28] Ishibashi O, Ikegame M, Takizawa F, Yoshizawa T, Moksed MA, Iizawa F, et al. Endoglin is involved in BMP-2-induced osteogenic differentiation of periodontal

ligament cells through a pathway independent of Smad-1/5/8 phosphorylation. J Cell Physiol. 2010;222:465-73.

[29] Kawasaki T, Niki Y, Miyamoto T, Horiuchi K, Matsumoto M, Aizawa M, et al. The effect of timing in the administration of hepatocyte growth factor to modulate BMP-2-induced osteoblast differentiation. Biomaterials. 2010;31:1191-8.

[30] Lee JH, Kim CS, Choi KH, Jung UW, Yun JH, Choi SH, et al. The induction of bone formation in rat calvarial defects and subcutaneous tissues by recombinant human BMP-2, produced in Escherichia coli. Biomaterials. 2010;31:3512-9.

[31] Wang L, Huang Y, Pan K, Jiang X, Liu C. Osteogenic Responses to Different Concentrations/Ratios of BMP-2 and bFGF in Bone Formation. Ann Biomed Eng. 2010;38:77-87.

[32] Ai-Aql ZS, Alagl AS, Graves DT, Gerstenfeld LC, Einhorn TA. Molecular mechanisms controlling bone formation during fracture healing and distraction osteogenesis. J Dent Res. 2008;87:107-18.

[33] Cheng HW, Jiang W, Phillips FM, Haydon RC, Peng Y, Zhou L, et al. Osteogenic activity of the fourteen types of human bone morphogenetic proteins (BMPs). J Bone Joint Surg Am. 2003;85A:1544-52.

[34] McKay W, Peckham S, Badura J. A comprehensive clinical review of recombinant human bone morphogenetic protein-2 (INFUSE® Bone Graft). Int Orthop. 2007;31:729-34.

[35] Xu J, Li X, Lian JB, Ayers DC, Song J. Sustained and localized in vitro release of BMP-2/7, RANKL, and tetracycline from Flexbone, an elastomeric osteoconductive bone substitute. J Orthopaed Res. 2009;27:1306-11.

[36] Filion TM, Kutikov A, Song J. Chemically modified cellulose fibrous meshes for use as tissue engineering scaffolds. Bioorg Med Chem Lett. 2011;21:5067-70.

[37] Carragee EJ, Hurwitz EL, Weiner BK. A critical review of recombinant human bone morphogenetic protein-2 trials in spinal surgery: emerging safety concerns and lessons learned. Spine. 2011;11:471-91.

[38] Shields LB, Raque GH, Glassman SD, Campbell M, Vitaz T, Harpring J, et al. Adverse effects associated with high-dose recombinant human bone morphogenetic protein-2 use in anterior cervical spine fusion. Spine. 2006;31:542-7.

[39] Bruckman MA, Kaur G, Lee LA, Xie F, Sepulveda J, Breitenkamp R, et al. Surface modification of tobacco mosaic virus with "Click" chemistry. ChemBioChem. 2008;9:519-23.

[40] Schlick TL, Ding Z, Kovacs EW, Francis MB. Dual-Surface Modification of the Tobacco Mosaic Virus. J Am Chem Soc. 2005;127:3718-23.

[41] Lee LA, Nguyen HG, Wang Q. Altering the landscape of viruses and bionanoparticles. Org Biomol Chem. 2011;9:6189-95.

[42] Jiang L, Li Q, Li M, Zhou Z, Wu L, Fan J, et al. A modified TMV-based vector facilitates the expression of longer foreign epitopes in tobacco. Vaccine. 2006;24:109-15.

[43] McCormick AA, Corbo TA, Wykoff-Clary S, Nguyen LV, Smith ML, Palmer KE, et al. TMV-peptide fusion vaccines induce cell-mediated immune responses and tumor protection in two murine models. Vaccine. 2006;24:6414-23.

[44] Niu Z, Bruckman MA, Li S, Lee LA, Lee B, Pingali SV, et al. Assembly of tobacco mosaic virus into fibrous and macroscopic bundled arrays mediated by surface aniline polymerization. Langmuir. 2007;23:6719-24.

[45] Pennazio S, Roggero P. The discovery of the chemical nature of tobacco mosaic virus. Riv Biol. 2000;93:253-81.

[46] Wang X, Niu Z, Li S, Wang Q, Li X. Nanomechanical characterization of polyaniline coated tobacco mosaic virus nanotubes. J Biomed Mater Res A. 2008;87:8-14.

[47] Young M, Willits D, Uchida M, Douglas T. Plant viruses as biotemplates for materials and their use in nanotechnology. Annu Rev Phytopathol. 2008;46:361-84.

[48] Thomas WE, Discher DE, Shastri VP. Mechanical Regulation of Cells by Materials and Tissues. MRS Bull. 2010;35:578-83.

[49] Lin Y, Su Z, Xiao G, Balizan E, Kaur G, Niu Z, et al. Self-assembly of virus particles on flat surfaces via controlled evaporation. Langmuir. 2011;27:1398-402.

[50] Mendonça DBS, Miguez PA, Mendonça G, Yamauchi M, Aragão FJL, Cooper LF. Titanium surface topography affects collagen biosynthesis of adherent cells. Bone. 2011;49:463-72.

[51] Vunjak-Novakovic G, Freshney RI. Cuture of Cells for Tissue Engineering. In: Freshney RI, editor. Culture of Specialized Cells. Hoboken, New Jersey: Wiley-Liss; 2006.

[52] Kärner E, Bäckesjö C-M, Cedervall J, Sugars RV, Ährlund-Richter L, Wendel M. Dynamics of gene expression during bone matrix formation in osteogenic cultures

derived from human embryonic stem cells in vitro. Biochim Biophys Acta, Gen Subj. 2009;1790:110-8.

[53] Wu L, Lee LA, Niu Z, Ghoshroy S, Wang Q. Visualizing Cell Extracellular Matrix (ECM) Deposited by Cells Cultured on Aligned Bacteriophage M13 Thin Films. Langmuir. 2011;27:9490-6.

[54] Lenhert S, Meier MB, Meyer U, Chi L, Wiesmann HP. Osteoblast alignment, elongation and migration on grooved polystyrene surfaces patterned by Langmuir-Blodgett lithography. Biomaterials. 2005;26:563-70.

[55] Teixeira AI, Abrams GA, Bertics PJ, Murphy CJ, Nealey PF. Epithelial contact guidance on well-defined micro- and nanostructured substrates. J Cell Sci. 2003;116:1881-92.

[56] Hou C-H, Hou S-M, Tang C-H. Ultrasound increased BMP-2 expression via PI3K, Akt, c-Fos/c-Jun, and AP-1 pathways in cultured osteoblasts. J Cell Biochem. 2009;106:7-15.

[57] Bi LX, Simmons DJ, Mainous E. Expression of BMP-2 by Rat Bone Marrow Stromal Cells in Culture. Calcif Tissue Int. 1999;64:63-8.

[58] Javed A, Chen H, Ghori FY. Genetic and transcriptional control of bone formation. Oral Maxillofac Surg Clin North Am. 2010;22:283-93, v.

[59] Cambien Ba, Pomeranz M, Millet M-A, Rossi B, Schmid-Alliana A. Signal transduction involved in MCP-1 mediated monocytic transendothelial migration. Blood. 2001;97:359-66.

[60] Champagne CM, Takebe J, Offenbacher S, Cooper LF. Macrophage cell lines produce osteoinductive signals that include bone morphogenetic protein-2. Bone. 2002;30:26-31.

[61] Kim Y-S, Min K-S, Jeong D-H, Jang J-H, Kim H-W, Kim E-C. Effects of fibroblast growth factor-2 on the expression and regulation of chemokines in human dental pulp cells. J Endodont. 2010;36:1824-30.

[62] Nakamura I, Jimi E, Gerald L. Regulation of osteoclast differentiation and function by interleukin-1. Vitam Horm: Academic Press; 2006. p. 357-70.

[63] Xing ZQ, Lu CY, Hu D, Yu YY, Wang XD, Colnot C, et al. Multiple roles for CCR2 during fracture healing. Dis Model Mech. 2010;3:451-8.

[64] Rifas L. T-cell cytokine induction of BMP-2 regulates human mesenchymal stromal cell differentiation and mineralization. J Cell Biochem. 2006;98:706-14.

[65] Higashino K, Viggeswarapu M, Bargouti M, Liu H, Titus L, Boden SD. Stromal cell-derived factor-1 potentiates bone morphogenetic protein-2 induced bone formation. Tissue Eng Part A. 2011;17:523-30.

[66] Huebsch N, Arany PR, Mao AS, Shvartsman D, Ali OA, Bencherif SA, et al. Harnessing traction-mediated manipulation of the cell/matrix interface to control stem-cell fate. Nat Mater. 2010;9:518-26.

[67] Mammoto A, Ingber DE. Cytoskeletal control of growth and cell fate switching. Curr Opin Cell Biol. 2009;21:864-70.

[68] Geiger B, Bershadsky A, Pankov R, Yamada KM. Transmembrane crosstalk between the extracellular matrix and the cytoskeleton. Nat Rev Mol Cell Biol. 2001;2:793-805.

[69] Mierke C. The role of vinculin in the regulation of the mechanical properties of cells. Cell Biochem Biophys. 2009;53:115-26.

[70] García AJ, Reyes CD. Bio-adhesive Surfaces to Promote Osteoblast Differentiation and Bone Formation. J Dent Res. 2005;84:407-13.

[71] Siebers MC, ter Brugge PJ, Walboomers XF, Jansen JA. Integrins as linker proteins between osteoblasts and bone replacing materials. A critical review. Biomaterials. 2005;26:137-46.

[72] Peterson L, Burridge K. Focal adhesions and focal complexes. Oxford, UK: University Press; 2002.

[73] Katz BZ, Zamir E, Bershadsky A, Kam Z, Yamada KM, Geiger B. Physical state of the extracellular matrix regulates the structure and molecular composition of cell-matrix adhesions. Mol Biol Cell. 2000;11:1047-60.

CHAPTER 2

POSSIBLE SIGNALING PATHWAY INVOLVED IN TMV SUBSTRATE-INDUCED EARLY UPREGULATION OF BMP2

2.1 INTRODUCTION

2.1.1 Bone marrow derived mesenchymal stem cells

Stem cell fate is closely controlled by the surrounding stimuli, including both soluble and insoluble factors. How stem cells respond to different topographical cues has been extensively studied for tissue engineering and regenerative medicine applications [1-4]. Recently, it has been highlighted that the mechanical stimuli is also very important for the proliferation and differentiation of bone cells [5-7]. Bone marrow derived mesenchymal stem cells (BMSCs) were used to study material-mediated osteogenic differentiation in this chapter. BMSCs are from the non-hematopoietic sub-population of bone marrow stroma [8-10], which have the ability to self-renew and differentiate to various lineages, such as adipocytes, osteocytes, chondrocytes, hepatocytes, neurons, muscle cells, and epithelial cells [10-15].

2.1.2 Plant virus-based substrates accelerate osteogenesis

In our previous work, we have reported accelerated osteogenic differentiation for BMSCs grown on plant virus coated substrates in comparison to cells cultured on conventional tissue culture plastic (TCP) [16, 17]. Two different plant viruses were employed in those studies, i.e. spherical *Turnip yellow mosaic virus* (TYMV) and rod-like *Tobacco mosaic*

virus (TMV). In both situations, several key mRNA markers associated with bone differentiation peaked at day 14 for cells on virus-coated substrates, whereas the cells on conventional plates required an additional 7 days to reach similar expression profiles [16, 17]. Moreover, immunohistochemical staining for osteoblastic specific differentiation markers, osteocalcin, osteonectin, and osteopontin, had supported the gene expression profiles on day 14. The expression of such osteogenic markers were further enhanced upon chemically modifying the virus with phosphates as indicated by increased Ca^{2+} mineralization and even higher mRNA expression levels of osteocalcin [18]. More importantly, our recent report illustrated that the roughness of TMV-coated substrate induced an early upregulation of endogenous levels of bone morphogenetic protein-2 (BMP2), which is the most potent bone inducing agent, through the disruption of actin and the reduction in focal adhesion size [19].

2.1.3 BMP2 as a key osteogenic initiator

BMP2 is a member of bone morphogenetic protein subgroup within the transforming growth factor β (TGF-β) super family. Among the bone morphogenetic proteins (BMPs), the role of BMP2 in osteoblast differentiation and bone formation during embryonic skeletal development and postnatal bone remodelling have been extensively documented [20-24]. Although overexpression of BMP2 by genetic transfection has proven to increase bone regeneration [25-29], the regulation of endogenous BMP2 expression is still unclear. There are recent evidences that external mechanical stress can induce the upregulation of endogenous BMP2 expression, leading to a long term osteogenesis [6, 30, 31]. Kearney *et al.* [30] suggested that stress and strain induced osteogenesis through

mitogen-activated protein kinases (MAPKs), such as extracellular regulated kinase (ERK), phosphatidylinositol 3-kinase (PI3K), and p38 MAPK. In this chapter, we attempted to investigate upstream regulators of BMP2 for a better understanding about TMV substrate-induced osteogenic acceleration via an early increase in endogenous BMP2 expression. Data from various experiments, including gene microarray [16], cytokine antibody array [19], quantitative real-time PCR (RT-qPCR), and motility gene PCR array, were combined and analyzed for upstream signalling events prior to the observed BMP2 expression induction. It is believed that cytokine production may facilitate the aggregation of BMSCs to form nodules upon seeding on TMV substrate [19] and certain protein kinases could be involved to signal BMP2 upregulation in a similar way to stress-induced osteogenesis [30].

2.2 RESULTS AND DISCUSSION

2.2.1 Upregulation of cytokines prior to BMP2 upregulation

Chemokines, small chemotactic cytokines, are not only important in the migration of immune cells during injury and infection [32], but also the migration of stem cells during body development and maturation [33]. It has been illustrated that cytokines are involved in growth regulation, hematopoiesis, embryologic development, angiogenesis, stem cell trafficking and tissue localization [34]. From our previous report, BMSCs on TMV produced cytokine-induced neutrophile chemoattractant 1 and 2 (CINC-1 and -2), macrophage inflammatory protein (MIP-3α), and vascular endothelial growth factor (VEGF) on the cytokine antibody array [19]. To follow up with this result, the mRNA expression levels of these cytokines along with one additional cytokine, macrophage

chemotactic protein 1 (MCP-1), were quantified by RT-qPCR (Figure 2.1). It has been demonstrated that MCP-1 could induce BMP2 expression in macrophages [35] so it would be interesting to investigate its expression in BMSCs on TMV substrate. The result in Figure 2.1 was consistent with previously published cytokine antibody array [19], indicating an increased production of CINC-1, CINC-2, MIP-3α, VEGF, and MCP-1 in BMSCs grown on TMV substrate. There was no significant change in tissue inhibitor of metalloproteinase 1 (TIMP-1) production in both samples.

BMP2 expression was reported to reach the maximum level at 8 hours after osteoinduction [19]. However, the upregulation of these cytokines were peaked at 4 hours after osteoinduction from RT-qPCR experiment (Figure 2.1) as well as their protein expressions were detectable at 4 hours after osteoinduction [19]. It is possible that these cytokines may be expressed even earlier because 4 hours was the earliest time point in this experiment. The prior expressions of cytokines could facilitate the migration of BMSCs to form cell nodules and the subsequent uptick of BMP2 production.

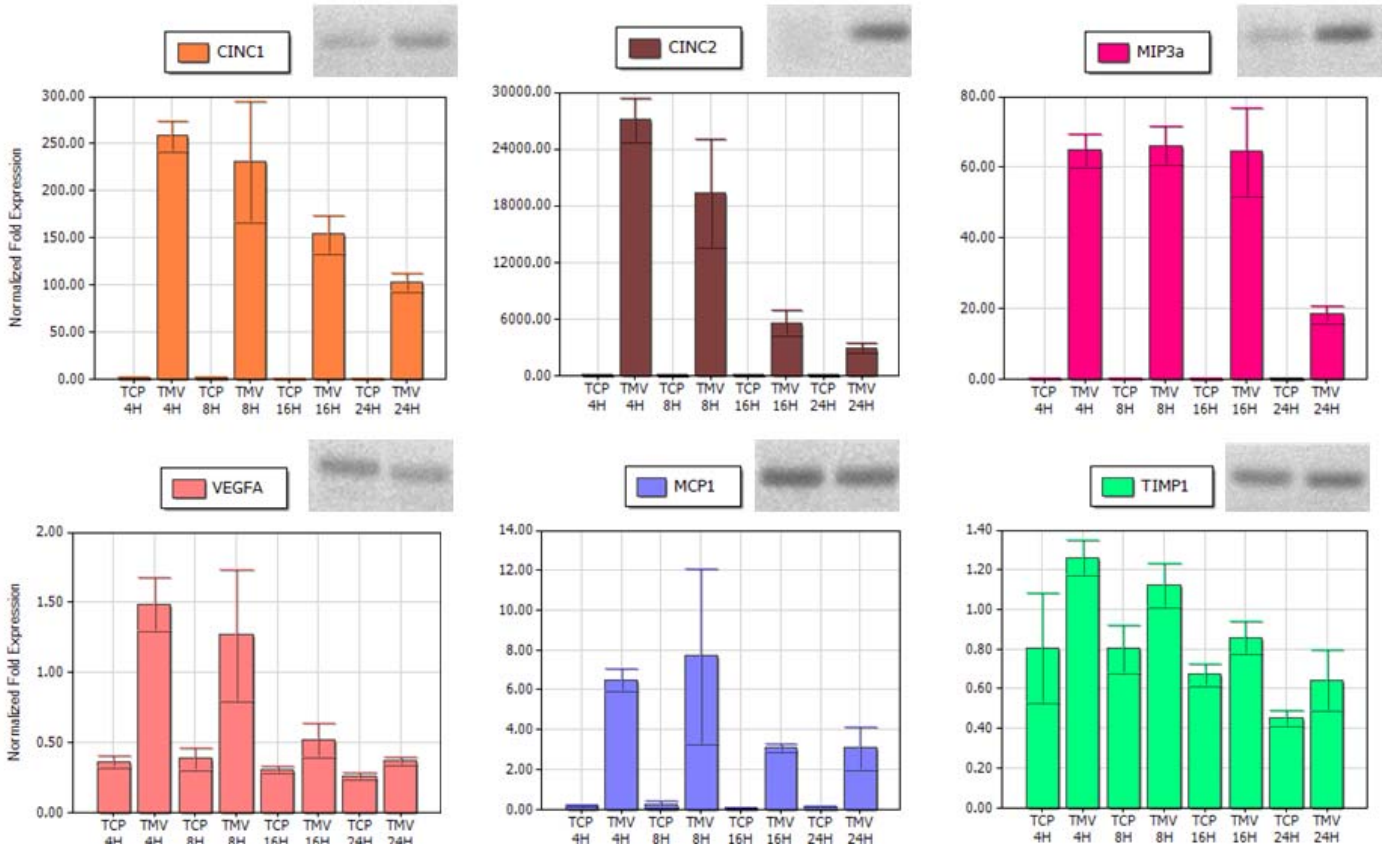

Figure 2.1 RT-qPCR analysis for cytokine gene expressions in BMSCs under osteogenic condition at 4, 8, 16, and 24 hours after osteoinduction. BMSCs were seeded on TCP or TMV substrate. At every time point, BMSCs on TMV showed increased mRNA expression levels of CINC-1, CINC-2, MIP-3α, VEGF, and MCP-1. There was no significant change in TIMP-1 mRNA expression level. The PCR product bands on 1% agarose gel were imaged, indicating single bands of specific PCR products for each gene (left: TCP, right: TMV). The error bars denote ± 1 S.D.

2.2.2 PCR array for expression changes in motility genes

In order to screen if genes involved in cell motility were involved in an early cell nodule formation induced by cytokines and the early upregulation of endogenous BMP2 expression, PCR array screening 84 key genes involved in the movement of cells was performed. The analyzed data was organized in a scattered plot with 2-fold cutoff (Figure 2.2). Genes that had less than 2-fold change were regarded as not significant and represented as black circles in Figure 2.2. There were fewer genes upregulated (red circles) compared to downregulated ones (green circles). A complete list of motility genes and their expression fold change values was organized from the most upregulated to the most downregulated in Table 2.1. The insignificant change of gene expression levels remains to have a value number in black. The significant gene upregulation has a fold-change number in red, while the significant gene downregulation has a fold-change number in blue. From Table 2.1, the upregulation value of VEGF expression level (1.43-fold) is consistent with the value from RT-qPCR in Figure 2.1. This validated the data from cell motility PCR array.

The interaction between cell and extracellular matrix (ECM) is mediated by cell surface receptors (i.e. integrins) [36]. Integrins belong to a group of heterodimeric (α and β subunits) transmembrane adhesion receptors for ECM proteins such as fibronectin and vitronectin [36]. Osteoblasts have been shown to express integrin subunits α_1, α_2, α_3, α_4, α_5, α_6, α_v, β_1, β_3, and β_5 [37]. A unique combination of α and β subunits determine which ECM molecules will be recognized by a cell. Osteogenesis was reported to involve the recognition of $\alpha_2\beta_1$ to type I collagen and $\alpha_5\beta_1$ to fibronectin [38]. Surprisingly, it was observed that the mRNA level of *itga4* was upregulated (3.08-fold), while that of *itgb1*

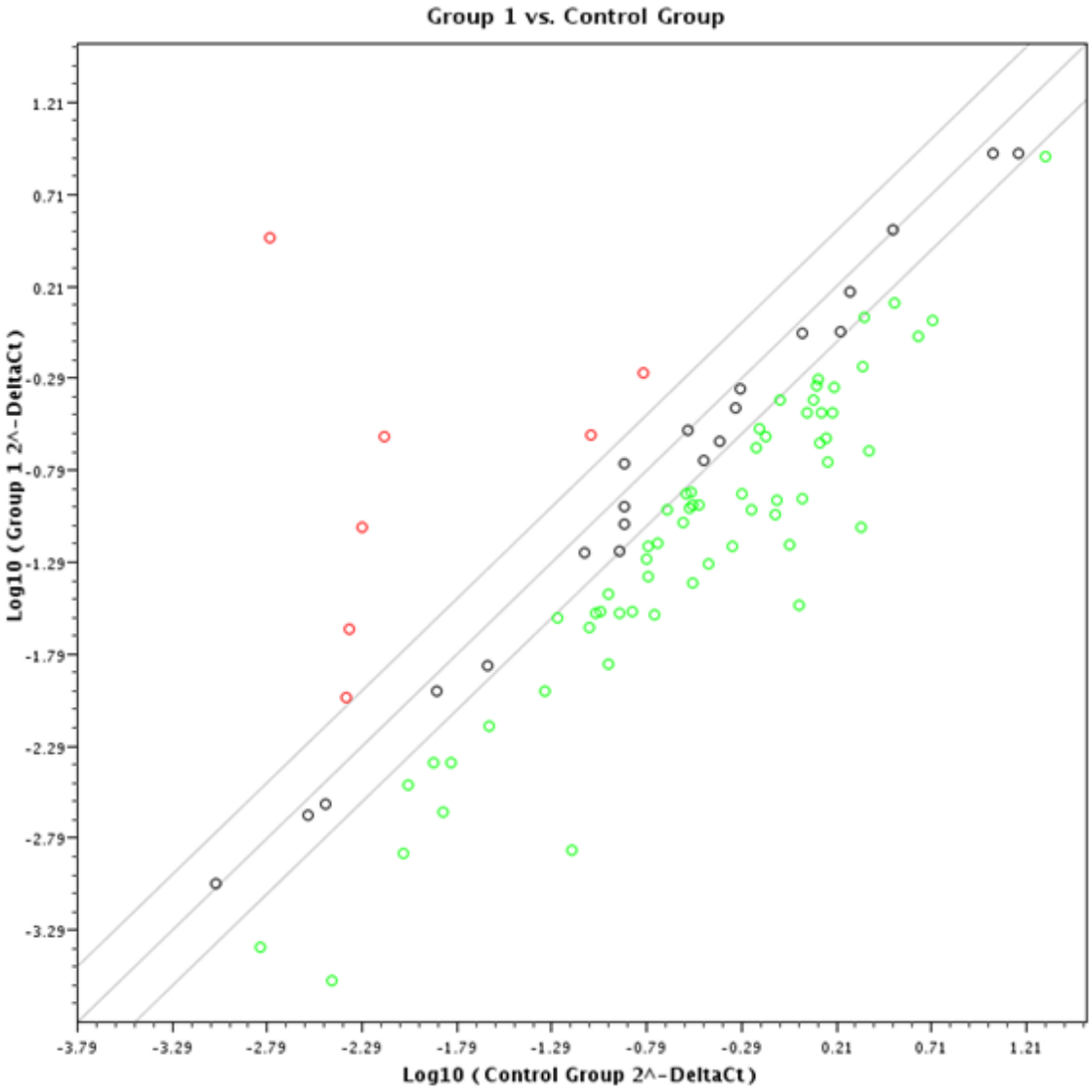

Figure 2.2 Scattered plot with 2-fold cutoff of data from rat cell motility gene PCR array. Red circles represent up-regulated genes and green circles represent down-regulated genes.

Table 2.1 A complete list of cell motility genes with corresponding expression fold change of BMSCs on TMV over those on TCP control, arranged from the most up-regulated to the most down-regulated gene expression fold change.

Gene Symbol	Description	Fold Up- or Down-Regulation
Arhgef7	Rho guanine nucleotide exchange factor (GEF) 7	1766.22
Actn3	Actinin alpha 3	37.12
Mmp9	Matrix metallopeptidase 9	15.66
Rac2	Ras-related C3 botulinum toxin substrate 2 (rho family, small GTP binding protein Rac2)	5.07
Plcg1	Phospholipase C, gamma 1	3.5
Itga4	Integrin, alpha 4	3.08
Rho	Rhodopsin	2.2
Vegfa	Vascular endothelial growth factor A	1.43
Dpp4	Dipeptidylpeptidase 4	1.06
Pten	Phosphatase and tensin homolog	-1.12
Plaur	Plasminogen activator, urokinase receptor	-1.17
Pik3ca	Phosphoinositide-3-kinase, catalytic, alpha polypeptide	-1.2
Itgb2	Integrin, beta 2	-1.23
Ptk2b	PTK2B protein tyrosine kinase 2 beta	-1.25
Itgb3	Integrin, beta 3	-1.32
Hgf	Hepatocyte growth factor	-1.33
Rnd3	Rho family GTPase 3	-1.35
Pld1	Phospholipase D1	-1.52
Rasa1	RAS p21 protein activator (GTPase activating protein) 1	-1.68
Met	Met proto-oncogene	-1.69
Vim	Vimentin	-1.73
Stat3	Signal transducer and activator of transcription 3	-1.76
Mmp2	Matrix metallopeptidase 2	-1.84
Ptk2	PTK2 protein tyrosine kinase 2	-1.97
Vcl	Vinculin	-2.09
Actr3	ARP3 actin-related protein 3 homolog (yeast)	-2.1
Wasf2	WAS protein family, member 2	-2.1
Egfr	Epidermal growth factor receptor	-2.14
Pxn	Paxillin	-2.16
Rock1	Rho-associated coiled-coil containing protein kinase 1	-2.29
Mapk1	Mitogen activated protein kinase 1	-2.33

Gene Symbol	Description	Fold Up- or Down-Regulation
Rhoa	Ras homolog gene family, member A	-2.49
Cdc42	Cell division cycle 42 (GTP binding protein)	-2.56
Rdx	Radixin	-2.66
Ptpn1	Protein tyrosine phosphatase, non-receptor type 1	-2.67
Rac1	Ras-related C3 botulinum toxin substrate 1	-2.71
Pak1	P21 protein (Cdc42/Rac)-activated kinase 1	-2.73
Vasp	Vasodilator-stimulated phosphoprotein	-2.78
Enah	Enabled homolog (Drosophila)	-2.84
Tln1	Talin 1	-2.84
Tgfb1	Transforming growth factor, beta 1	-2.91
Wasf1	WAS protein family, member 1	-2.93
Baiap2	BAI1-associated protein 2	-2.94
Myh10	Myosin, heavy chain 10, non-muscle	-3.01
Sh3pxd2a	SH3 and PX domains 2A	-3.01
Rhoc	Ras homolog gene family, member C	-3.17
Fap	Fibroblast activation protein, alpha	-3.22
Capn1	Calpain 1	-3.38
Arhgdia	Rho GDP dissociation inhibitor (GDI) alpha	-3.4
Timp2	TIMP metallopeptidase inhibitor 2	-3.42
Egf	Epidermal growth factor	-3.59
Igf1	Insulin-like growth factor 1	-3.6
Ezr	Ezrin	-3.62
Limk1	LIM domain kinase 1	-3.65
Myl9	Myosin, light chain 9, regulatory	-3.76
Svil	Supervillin	-3.83
Myh9	Myosin, heavy chain 9, non-muscle	-4.05
Prkca	Protein kinase C, alpha	-4.27
Crk	V-crk sarcoma virus CT10 oncogene homolog (avian)	-4.28
Wipf1	WAS/WASL interacting protein family, member 1	-4.57
Msn	Moesin	-4.67
Pfn1	Profilin 1	-4.88
Diaph1	Diaphanous homolog 1 (Drosophila)	-4.92
Itgb1	Integrin, beta 1	-5.01
Cttn	Cortactin	-5.76
Rhob	Ras homolog gene family, member B	-5.8
Csf1	Colony stimulating factor 1 (macrophage)	-5.96
Fgf2	Fibroblast growth factor 2	-6.19

Gene Symbol	Description	Fold Up- or Down-Regulation
Pak4	P21 protein (Cdc42/Rac)-activated kinase 4	-6.26
Bcar1	Breast cancer anti-estrogen resistance 1	-6.79
Igf1r	Insulin-like growth factor 1 receptor	-6.85
Src	V-src sarcoma (Schmidt-Ruppin A-2) viral oncogene homolog (avian)	-7.08
Capn2	Calpain 2	-7.15
Akt1	V-akt murine thymoma viral oncogene homolog 1	-7.17
Arf6	ADP-ribosylation factor 6	-7.45
Actn4	Actinin alpha 4	-8.12
Mmp14	Matrix metallopeptidase 14 (membrane-inserted)	-8.33
Cav1	Caveolin 1, caveolae protein	-9.32
Actn1	Actinin, alpha 1	-11.7
Iqub	IQ motif and ubiquitin domain containing	-13.15
Ilk	Integrin-linked kinase	-14.43
Cfl1	Cofilin 1, non-muscle	-27.3
Actr2	ARP2 actin-related protein 2 homolog (yeast)	-33.97
Mylk	Myosin light chain kinase	-47.22

was downregulated (-5.01-fold) in BMSCs on TMV surface (Table 2.1). It will be interesting to further study the involvement of integrin α_4 subunit in TMV-induced BMP2 production and subsequent acceleration in osteogenesis since there has not been any report on this relationship.

As reported previously that actin skeleton disruption could contribute to osteogenesis [19], from Table 2.1 *actn3* was highly upregulated (37.12-fold), whereas *actn4* (-8.12-fold) and *actn1* (-11.7-fold) were downregulated in BMSCs on TMV substrate. The decreased in *actn4* and *actn1* expression levels could lead to the reported actin disruption [19]. However, the increase in *actn3* expression level may result in an increase in osteogenesis rate as Yang *et al.* [39] demonstrated that α-actinin 3 deficiency was associated with reduced bone mass. Although the direct relationship between α-actinin 3 and BMP2 is still unclear, we could predict that α-actinin 3 is involved in the bone formation process.

2.2.3 BMP2 upregulation may be controlled by MAPKs and inhibitors

Most of the studies done on BMP2 are on the inductive effect of recombinant BMP2 on downstream osteogenic gene and protein expression [40-46]. Some reported on the overexpression of BMP2 to improve bone healing process [25-29, 47-50]. However, little has been published on the native regulation of BMP2. It has been documented that typically cell nodules were formed at 2-3 days after cell confluency, and the nodules started to grow larger and mineralize at 5-20 days *in vitro* [51]. During this culture period, there was a 2-3 fold increase in the expression of BMP2 mRNA at the first 5 days and the expression increased to a peak of 4-5 fold change at 10 days. After that, the

expression of BMP2 mRNA gradually decreased to the baseline level of 1 fold over the next 10 days. In our previous work, BMP2 mRNA expression had a peak at 8 hours after osteogenic induction [19], which is 10 days earlier than the typical *in vitro* culture. The early expression of BMP2 could be the reason of accelerated osteogenesis. The expression fold change observed is a result of the change in transcriptional regulation. It is believed that several protein kinases are involved in the regulation of BMP2 transcription. For example, an increase in BMP2 expression induced by nanohydroxyapatite in culture media was inhibited by treatment with a p38 MAPK inhibitor [52]. In a strain-induced synthesis of BMP2, the addition of ERK, PI3K, p38 MAPK inhibitors reduced BMP2 mRNA expression level [30]. In our system with TMV substrate-induced BMP2 upregulation, the signalling cascade could be similar with the strain-induced situation [30] because the BMP2 expression patterns were comparable. It is possible that stress is induced in BMSCs upon coming in contact with TMV substrate as disrupted actin filaments and smaller focal adhesion size were observed [19]. However, further protein kinase activation and inhibition experiments are necessary to confirm which protein kinases are involved in TMV substrate-induced BMP2 upregulation.

Potency of BMP2 is not only controlled at the transcription level, but it can also be controlled by extracellular antagonists, such as noggin and chordin, which bind to BMP2 preventing its binding to the cell surface receptors [53]. It may be insightful to investigate protein expression levels of BMP2 antagonists in order to explain the change in BMP2 activity in BMSCs on TMV substrate. Interestingly, although BMP2 belongs to the same family as TGF-β, the addition of TGF-β during the first 8 days after cell

confluency inhibited the normal increase of BMP2 mRNA expression [51]. As shown in Table 2.1, TGF-β expression level in BMSCs on TMV was lower by 2.91-fold compared to those on TCP control.

In addition to the blocking of BMP2 by its antagonists, BMP2 knockout BMSCs could serve as a control for a successful inhibition. Moreover, it is necessary to confirm BMP2 as a key regulator in TMV substrate-induced osteogenic acceleration. The use of BMP2 knockout BMSCs would provide a better understanding in the involvement of endogenous BMP2 upregulation in material-mediated bone regeneration.

2.3 CONCLUSION

The highest BMP2 mRNA and protein levels was detected in cells cultured on TMV-coated substrates after 8 hours of osteoinduction and maintained high levels of *BMP2* mRNA and protein levels even after 24 hours. Screening the media for cytokines revealed the presence of CINC-1, CINC-2, MIP-3α, and VEGF at 4 hours after osteoinduction, which is prior to the BMP2 expression peak. Gene expression analysis of these cytokines, along with MCP-1, confirmed and quantified their upregulation. There were 7 motility genes upregulated from PCR array experiment, suggesting TMV substrate promotes cell aggregation and induces an early onset BMP2 expression (Figure 2.3).

Although extensive studies with BMP2 have shown potent osteoinductive effects at early time points, additional studies on BMP2 regulation will be necessary to identify the signalling pathways involved in TMV substrate recognition and BMP2 induction. Further investigation into protein kinases and extracellular antagonists could be helpful for a better understanding of how the TMV coating can promote the endogenous

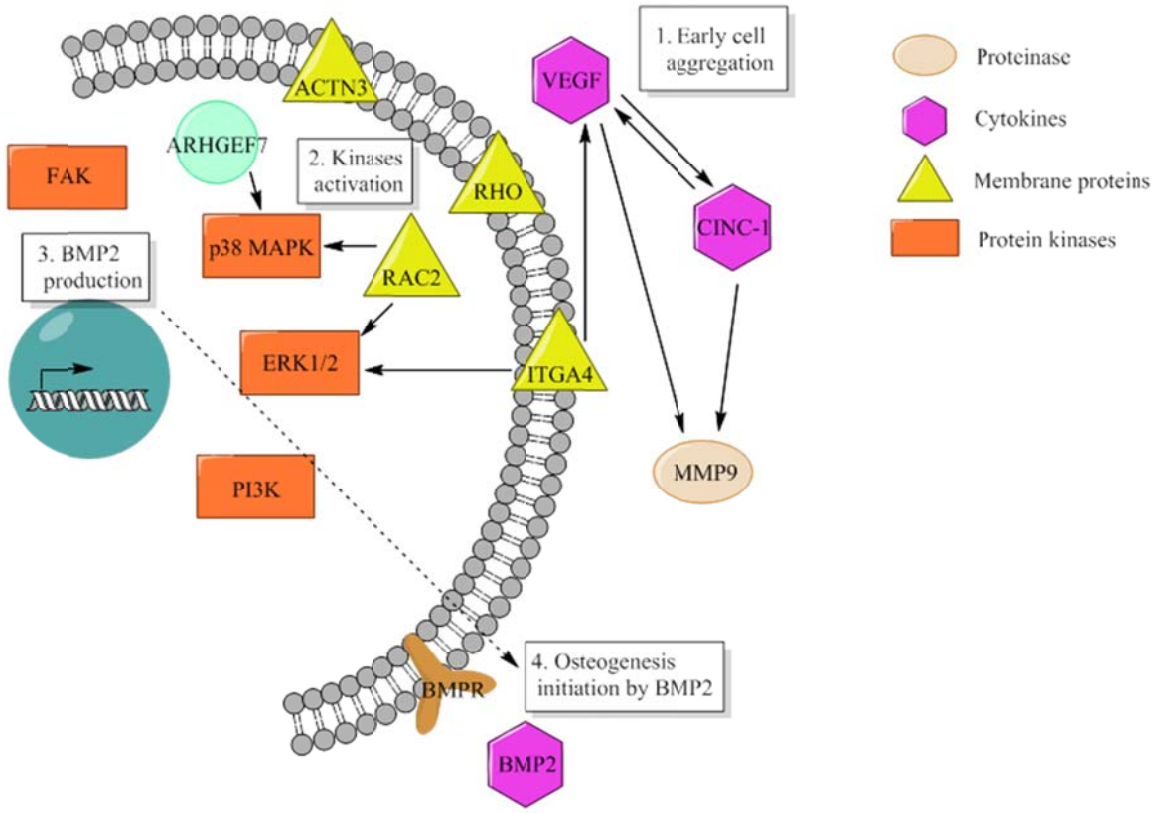

Figure 2.3 Schematic diagram predicting sequential events for TMV-induced BMP2 upregulation, leading to accelerated osteogenesis

production of BMP2. The regulation of endogenous BMP2 expression will be critical for advanced biomaterial development in bone tissue engineering applications.

2.4 EXPERIMENTAL SECTION

2.4.1 TMV Isolation

TMV was isolated and purified according to a protocol previously reported [16, 18].

2.4.2 Preparation of TMV coated substrates

3-Aminopropyltriethoxysilane (APTES) coated slides (Lab Scientific Inc.) were cut into 1.5 cm^2 wafers. Both coverslips and slide wafers were sterilized with ethanol before use. For TMV coating, the wafers and coverslips were coated with 0.2 mg/mL TMV solution diluted in water and the coated substrates were dried overnight in a sterile biosafety cabinet. The virus coverage on the wafers was characterized using tapping-mode AFM images using a NanoScope IIIA MultiMode AFM (Veeco). Si tips with a resonance frequency of approximately 300 kHz, a spring constant of about 40 N m^{-1} and a scan rate of 0.5 Hz were used.

2.4.3 BMSC isolation and expansion

Primary BMSCs were isolated from the bone marrow of young adult 80 g male Wister rats (Harlan Sprague Dawley, Inc.). The procedures were performed in accordance with the guidelines for animal experimentation by the Institutional Animal Care and Use Committee, School of Medicine, University of South Carolina. Cells were maintained in growth medium (DMEM supplemented with 10% fetal bovine serum (FBS), penicillin

(100 U/mL), streptomycin (100 µg/mL) and amphotericin B (250 ng/mL)) and passaged no more than four times after isolation. To induce osteogenesis, growth media was replaced with osteogenic media consisting of DMEM supplemented with 10% FBS, penicillin (100 u/mL), streptomycin (100 µg/mL), amphotericin B (250 ng/mL), 10 mM sodium β-glycerolphosphate, L-ascorbic acid 2-phosphate (50 µg/mL) and 10^{-8} M dexamethasone. Media was replenished every 3-4 days.

2.4.4 Quantitative real-time RT-PCR analysis (RT-qPCR)

TMV coated wafers were seeded with 4.5×10^4 cells per wafer and allowed to attach overnight in growth media. The media is replaced with osteogenic media and cultured for 4, 8, 16, and 24 hours. In addition, BMSCs with similar density were seeded on 3.8 cm^2 tissue culture plastic (TCP) in the osteogenic media, for the above mentioned time periods. The cell cultures were terminated at these time points and total RNA was subsequently extracted using RNeasy mini purification kit (Qiagen).

The quality and quantity of the extracted RNA was analyzed using Bio-Rad Experion (Bio-Rad Laboratories) and was reverse transcribed by using qScript™ cDNA Supermix (Quanta Biosciences). RT-qPCR (iQ5 real-time PCR detection system Bio-Rad Laboratories) was done by the method described as: 60 cycles of PCR (95˚C for 20 s, 58˚C for 15 s, and 72˚C for 15 s), after initial denaturation step of 5 minutes at 95˚C, by using 12.5 µL of iQ5 SYBR Green I Supermix, 2 pmol/µL of each forward and reverse primers and 0.5 µL cDNA templates in a final reaction volume of 25 µL. Glyceraldehyde 3-phosphate dehydrogenase (GAPDH) was used as the housekeeping gene. Data collection was enabled at 72˚C in each cycle and C_T (threshold cycle) values were calculated using the iQ5 optical system software version 2.1. The expression levels of

differentiated genes and undifferentiated genes were calculated using Pfaffl's method (M.W. Pfaffl, G.W. Horgan and L. Dempfle, Relative expression software tool) for group-wise comparison and statistical analysis of relative expression results in real-time PCR, using GAPDH as the reference gene. Quantification of gene expression was based on the C_T value for each sample which was calculated as the average of three replicate measurements for each sample analyzed. "Pair Wise Fixed Reallocation Randomization Test" was performed on each sample and a value of $p < 0.05$ was regarded as significant. The primers used for RT-qPCR are shown in Table 2.2. The primers were synthesized commercially (Integrated DNA Technologies, Inc.), and evaluated for an annealing temperature of 58˚C.

2.4.5 Rat cell motility gene PCR array

TCP or TMV coated wafers were seeded with 4.5×10^4 cells per sample and allowed to attach overnight in growth media. The media is replaced with osteogenic media and cultured for 4 hours. The cell cultures were terminated at these time points and total RNA was subsequently extracted (RNeasy mini purification kit, Qiagen). Rat cell motility gene PCR array was purchased from SA Biosciences (Qiagen). The experiment was performed according to the manufacturer's instructions. In brief, RNA samples were converted to cDNA using RT^2 First Strand kit (Qiagen). Synthesized cDNA was added to RT^2 qPCR SYBR Green mastermix and aliquoted to the PCR array plate containing pre-loaded primers. RT-qPCR (iQ5 real-time PCR detection system Bio-Rad Laboratories) was done by the method described as: 40 cycles of PCR (95˚C for 15 sec, and 60˚C for 1 min), after initial denaturation step of 10 minutes at 95˚C. Data was analyzed and scatter plot of gene

Table 2.2 Primers used for RT-qPCR to measure cytokine gene expression levels. CINC-1: cytokine-induced neutrophile chemoattractant 1; CINC-2: cytokine-induced neutrophile chemoattractant 2; MCP-1: macrophage chemotactic protein 1; MIP-3α: macrophage inflammatory protein; and VEGF: vascular endothelial growth factor.

Gene	Sequence (5'-3')
CINC-1	Forward: TGGATGCGTTTCATCGATGGTCGT
	Reverse: AGCCTCTCACACATTCCTCACCCT
CINC-2	Forward: AACATCCAGAGCTTGACGGTGACCC
	Reverse: CCGTTGAGGTACAGGAGCCCATGTT
GAPDH	Forward: ACTAAAGGGCATCCTGGGCTACACTGA
	Reverse: TGGGTGGTCCAGGGTTTCTTACTCCTT
MCP-1	Forward: ACACAGACAGAGGCCAGCCCAGAA
	Reverse: TGCCAGTGAATGAGTAGCAGCAGGT
MIP-3α	Forward: AGATGGCCGACGAAGCTTGTGACA
	Reverse: AAACCTCCAACCCCAGCTGTGATCA
TIMP-1	Forward: TCGACGCTGTGGGAAATGCCACA
	Reverse: AAGGCCTTTTGCTGAGCAGGGCT
VEGF	Forward: CAGGGGTCCTGGCAAAGAGAAGACA
	Reverse: TGGGGAAGGGTAAGCCACTCACACA

profile was generated by RT^2 Profiler PCR Array Data Analysis version 3.3, provided online by the manufacturer.

2.5 REFERENCES

[1] Ayres CE, Jha BS, Sell SA, Bowlin GL, Simpson DG. Nanotechnology in the design of soft tissue scaffolds: innovations in structure and function. Wiley Interdiscip Rev Nanomed Nanobiotechnol. 2010;2:20-34.

[2] Discher DE, Mooney DJ, Zandstra PW. Growth Factors, Matrices, and Forces Combine and Control Stem Cells. Science. 2009;324:1673-7.

[3] Dvir T, Timko BP, Kohane DS, Langer R. Nanotechnological strategies for engineering complex tissues. Nat Nanotechnol. 2011;6:13-22.

[4] Hynes RO. The extracellular matrix: not just pretty fibrils. Science. 2009;326:1216-9.

[5] Liedert A, Kaspar D, Blakytny R, Claes L, Ignatius A. Signal transduction pathways involved in mechanotransduction in bone cells. Biochem Biophys Res Commun. 2006;349:1-5.

[6] Mai Z, Peng Z, Wu S, Zhang J, Chen L, Liang H, et al. Single Bout Short Duration Fluid Shear Stress Induces Osteogenic Differentiation of MC3T3-E1 Cells via Integrin β1 and BMP2 Signaling Cross-Talk. PLoS One. 2013;8:e61600.

[7] Thompson WR, Rubin CT, Rubin J. Mechanical regulation of signaling pathways in bone. Gene. 2012;503:179-93.

[8] Jiang Y, Jahagirdar BN, Reinhardt RL, Schwartz RE, Keene CD, Ortiz-Gonzalez XR, et al. Pluripotency of mesenchymal stem cells derived from adult marrow. Nature. 2002;418:41-9.

[9] Minguell JJ, Erices A, Conget P. Mesenchymal stem cells. Exp Biol Med. 2001;226:507-20.

[10] Pittenger MF, Mackay AM, Beck SC, Jaiswal RK, Douglas R, Mosca JD, et al. Multilineage potential of adult human mesenchymal stem cells. Science. 1999;284:143-7.

[11] Si YL, Zhao YL, Hao HJ, Fu XB, Han WD. MSCs: Biological characteristics, clinical applications and their outstanding concerns. Ageing Res Rev. 2011;10:93-103.

[12] Mackay AM, Beck SC, Murphy JM, Barry FP, Chichester CO, Pittenger MF. Chondrogenic differentiation of cultured human mesenchymal stem cells from marrow. Tissue Eng. 1998;4:415-28.

[13] Drost AC, Weng S, Feil G, Schafer J, Baumann S, Kanz L, et al. In vitro myogenic differentiation of human bone marrow-derived mesenchymal stem cells as a potential treatment for urethral sphincter muscle repair. Ann N Y Acad Sci. 2009;1176:135-43.

[14] Oswald J, Boxberger S, Jorgensen B, Feldmann S, Ehninger G, Bornhauser M, et al. Mesenchymal stem cells can be differentiated into endothelial cells in vitro. Stem Cells. 2004;22:377-84.

[15] Gong Z, Calkins G, Cheng EC, Krause D, Niklason LE. Influence of culture medium on smooth muscle cell differentiation from human bone marrow-derived mesenchymal stem cells. Tissue Eng Part A. 2009;15:319-30.

[16] Kaur G, Valarmathi MT, Potts JD, Jabbari E, Sabo-Attwood T, Wang Q. Regulation of osteogenic differentiation of rat bone marrow stromal cells on 2D nanorod substrates. Biomaterials. 2010;31:1732-41.

[17] Kaur G, Valarmathi MT, Potts JD, Wang Q. The promotion of osteoblastic differentiation of rat bone marrow stromal cells by a polyvalent plant mosaic virus. Biomaterials. 2008;29:4074-81.

[18] Kaur G, Wang C, Sun J, Wang Q. The synergistic effects of multivalent ligand display and nanotopography on osteogenic differentiation of rat bone marrow stem cells. Biomaterials. 2010;31:5813-24.

[19] Sitasuwan P, Andrew Lee L, Bo P, Davis EN, Lin Y, Wang Q. A plant virus substrate induces early upregulation of BMP2 for rapid bone formation. Integr Biol. 2012;4:651-60.

[20] Rosen V. BMP2 signaling in bone development and repair. Cytokine Growth Factor Rev. 2009;20:475-80.

[21] Ishibashi O, Ikegame M, Takizawa F, Yoshizawa T, Moksed MA, Iizawa F, et al. Endoglin is involved in BMP-2-induced osteogenic differentiation of periodontal ligament cells through a pathway independent of Smad-1/5/8 phosphorylation. J Cell Physiol. 2010;222:465-73.

[22] Kawasaki T, Niki Y, Miyamoto T, Horiuchi K, Matsumoto M, Aizawa M, et al. The effect of timing in the administration of hepatocyte growth factor to modulate BMP-2-induced osteoblast differentiation. Biomaterials. 2010;31:1191-8.

[23] Lee JH, Kim CS, Choi KH, Jung UW, Yun JH, Choi SH, et al. The induction of bone formation in rat calvarial defects and subcutaneous tissues by recombinant human BMP-2, produced in Escherichia coli. Biomaterials. 2010;31:3512-9.

[24] Wang L, Huang Y, Pan K, Jiang X, Liu C. Osteogenic responses to different concentrations/ratios of BMP-2 and bFGF in bone formation. Ann Biomed Eng. 2010;38:77-87.

[25] Ahrens M, Ankenbauer T, Schroder D, Hollnagel A, Mayer H, Gross G. Expression of human bone morphogenetic proteins-2 or -4 in murine mesenchymal progenitor C3H10T1/2 cells induces differentiation into distinct mesenchymal cell lineages. DNA Cell Biol. 1993;12:871-80.

[26] Baltzer AW, Lattermann C, Whalen JD, Wooley P, Weiss K, Grimm M, et al. Genetic enhancement of fracture repair: healing of an experimental segmental defect by adenoviral transfer of the BMP-2 gene. Gene Ther. 2000;7:734-9.

[27] Betz OB, Betz VM, Nazarian A, Egermann M, Gerstenfeld LC, Einhorn TA, et al. Delayed administration of adenoviral BMP-2 vector improves the formation of bone in osseous defects. Gene Ther. 2007;14:1039-44.

[28] Betz OB, Betz VM, Nazarian A, Pilapil CG, Vrahas MS, Bouxsein ML, et al. Direct Percutaneous Gene Delivery to Enhance Healing of Segmental Bone Defects. J Bone Joint Surg. 2006;88:355-65.

[29] Egermann M, Baltzer AW, Adamaszek S, Evans C, Robbins P, Schneider E, et al. Direct adenoviral transfer of bone morphogenetic protein-2 cDNA enhances fracture healing in osteoporotic sheep. Hum Gene Ther. 2006;17:507-17.

[30] Kearney EM, Farrell E, Prendergast PJ, Campbell VA. Tensile Strain as a Regulator of Mesenchymal Stem Cell Osteogenesis. Ann Biomed Eng. 2010;38:1767-79.

[31] Sumanasinghe RD, Bernacki SH, Loboa EG. Osteogenic differentiation of human mesenchymal stem cells in collagen matrices: effect of uniaxial cyclic tensile strain on bone morphogenetic protein (BMP-2) mRNA expression. Tissue Eng. 2006;12:3459-65.

[32] Niggli V. Signaling to migration in neutrophils: importance of localized pathways. Int J Biochem Cell Biol. 2003;35:1619-38.

[33] Vanden Berg-Foels WS. In Situ Tissue Regeneration: Chemoattractants for Endogenous Stem Cell Recruitment. Tissue Eng Part B Rev. 2013.

[34] Beider K, Abraham M, Peled A. Chemokines and chemokine receptors in stem cell circulation. Front Biosci. 2008;13:6820-33.

[35] Champagne CM, Takebe J, Offenbacher S, Cooper LF. Macrophage cell lines produce osteoinductive signals that include bone morphogenetic protein-2. Bone. 2002;30:26-31.

[36] Geiger B, Bershadsky A, Pankov R, Yamada KM. Transmembrane crosstalk between the extracellular matrix and the cytoskeleton. Nat Rev Mol Cell Biol. 2001;2:793-805.

[37] Siebers MC, ter Brugge PJ, Walboomers XF, Jansen JA. Integrins as linker proteins between osteoblasts and bone replacing materials. A critical review. Biomaterials. 2005;26:137-46.

[38] Franceschi RT. The Developmental Control of Osteoblast-Specific Gene Expression: Role of Specific Transcription Factors and the Extracellular Matrix Environment. Crit Rev Oral Biol Med. 1999;10:40-57.

[39] Yang N, Schindeler A, McDonald MM, Seto JT, Houweling PJ, Lek M, et al. α-Actinin-3 deficiency is associated with reduced bone mass in human and mouse. Bone. 2011;49:790-8.

[40] Boyne PJ, Lilly LC, Marx RE, Moy PK, Nevins M, Spagnoli DB, et al. De novo bone induction by recombinant human bone morphogenetic protein-2 (rhBMP-2) in maxillary sinus floor augmentation. J Oral Maxillofac Surg. 2005;63:1693-707.

[41] Burkus JK, Gornet MF, Dickman CA, Zdeblick TA. Anterior lumbar interbody fusion using rhBMP-2 with tapered interbody cages. Journal of spinal disorders & techniques. 2002;15:337-49.

[42] Carragee EJ, Hurwitz EL, Weiner BK. A critical review of recombinant human bone morphogenetic protein-2 trials in spinal surgery: emerging safety concerns and lessons learned. Spine. 2011;11:471-91.

[43] Carreon LY, Glassman SD, Brock DC, Dimar JR, Puno RM, Campbell MJ. Adverse events in patients re-exposed to bone morphogenetic protein for spine surgery. Spine. 2008;33:391-3.

[44] Fiorellini JP, Howell TH, Cochran D, Malmquist J, Lilly LC, Spagnoli D, et al. Randomized study evaluating recombinant human bone morphogenetic protein-2 for extraction socket augmentation. J Periodontol. 2005;76:605-13.

[45] McKay W, Peckham S, Badura J. A comprehensive clinical review of recombinant human bone morphogenetic protein-2 (INFUSE® Bone Graft). Int Orthop. 2007;31:729-34.

[46] Shields LB, Raque GH, Glassman SD, Campbell M, Vitaz T, Harpring J, et al. Adverse effects associated with high-dose recombinant human bone morphogenetic protein-2 use in anterior cervical spine fusion. Spine. 2006;31:542-7.

[47] Ferreira E, Potier E, Vaudin P, Oudina K, Bensidhoum M, Logeart-Avramoglou D, et al. Sustained and promoter dependent bone morphogenetic protein expression by rat mesenchymal stem cells after BMP-2 transgene electrotransfer. European cells & materials. 2012;24:18-28.

[48] Li JZ, Li H, Sasaki T, Holman D, Beres B, Dumont RJ, et al. Osteogenic potential of five different recombinant human bone morphogenetic protein adenoviral vectors in the rat. Gene Ther. 2003;10:1735-43.

[49] Noël D, Gazit D, Bouquet C, Apparailly F, Bony C, Plence P, et al. Short-Term BMP-2 Expression Is Sufficient for In Vivo Osteochondral Differentiation of Mesenchymal Stem Cells. Stem Cells. 2004;22:74-85.

[50] Steinert AF, Proffen B, Kunz M, Hendrich C, Ghivizzani SC, Noth U, et al. Hypertrophy is induced during the in vitro chondrogenic differentiation of human mesenchymal stem cells by bone morphogenetic protein-2 and bone morphogenetic protein-4 gene transfer. Arthritis Res Ther. 2009;11:R148.

[51] Ghosh-Choudhury N, Harris MA, Feng JQ, Mundy GR, Harris SE. Expression of the BMP 2 gene during bone cell differentiation. Critical reviews in eukaryotic gene expression. 1994;4:345-55.

[52] Suto M, Nemoto E, Kanaya S, Suzuki R, Tsuchiya M, Shimauchi H. Nanohydroxyapatite increases BMP-2 expression via a p38 MAP kinase dependent pathway in periodontal ligament cells. Arch Oral Biol. 2013;58:1021-8.

[53] Canalis E, Economides AN, Gazzerro E. Bone Morphogenetic Proteins, Their Antagonists, and the Skeleton. Endocrine Reviews. 2003;24:218-35.

CHAPTER 3

RGD-CONJUGATED ROD-LIKE VIRAL NANOPARTICLES ON 2D SCAFFOLD IMPROVED BONE DIFFERENTIATION OF MESENCHYMAL STEM CELLS

3.1 INTRODUCTION

3.1.1 Tobacco mosaic virus as a building block for 2D scaffold generation

Plant viral nanoparticles are meta-stable, readily available, monodispersed, and structurally uniform bionanoparticles. Such plant derived viral particles have gained great interest in nano- and biomedical applications. *Tobacco mosaic virus* (TMV) is among the most commonly used plant virus, having a rod-shape measuring 300 nm in length with a diameter of 18 nm (Figure 3.1A). The viral capsid consists of 2130 identical coat protein subunits assembled in a helical structure around the single stranded genomic RNA. The production of TMV is cost effective and the resulting viral particles are highly uniform in size. TMV nanoparticles have been demonstrated as powerful building blocks that can be efficiently functionalized via both genetic [1-3] and chemical [4, 5] modifications. Due to its identical subunits and regular structure, the same modification occurs on each individual subunit to yield a polyvalent and monodispersed display of ligands within a single TMV particle.

Furthermore, TMV has been shown to be an effective scaffold that accelerates bone differentiation of stem cells when coated on a 2D substrate and provides support for cell differentiation in 3D alginate hydrogels [6-9]. While the underlying mechanism is still unclear, the level of the potent osteogenic induction protein, bone morphogenetic

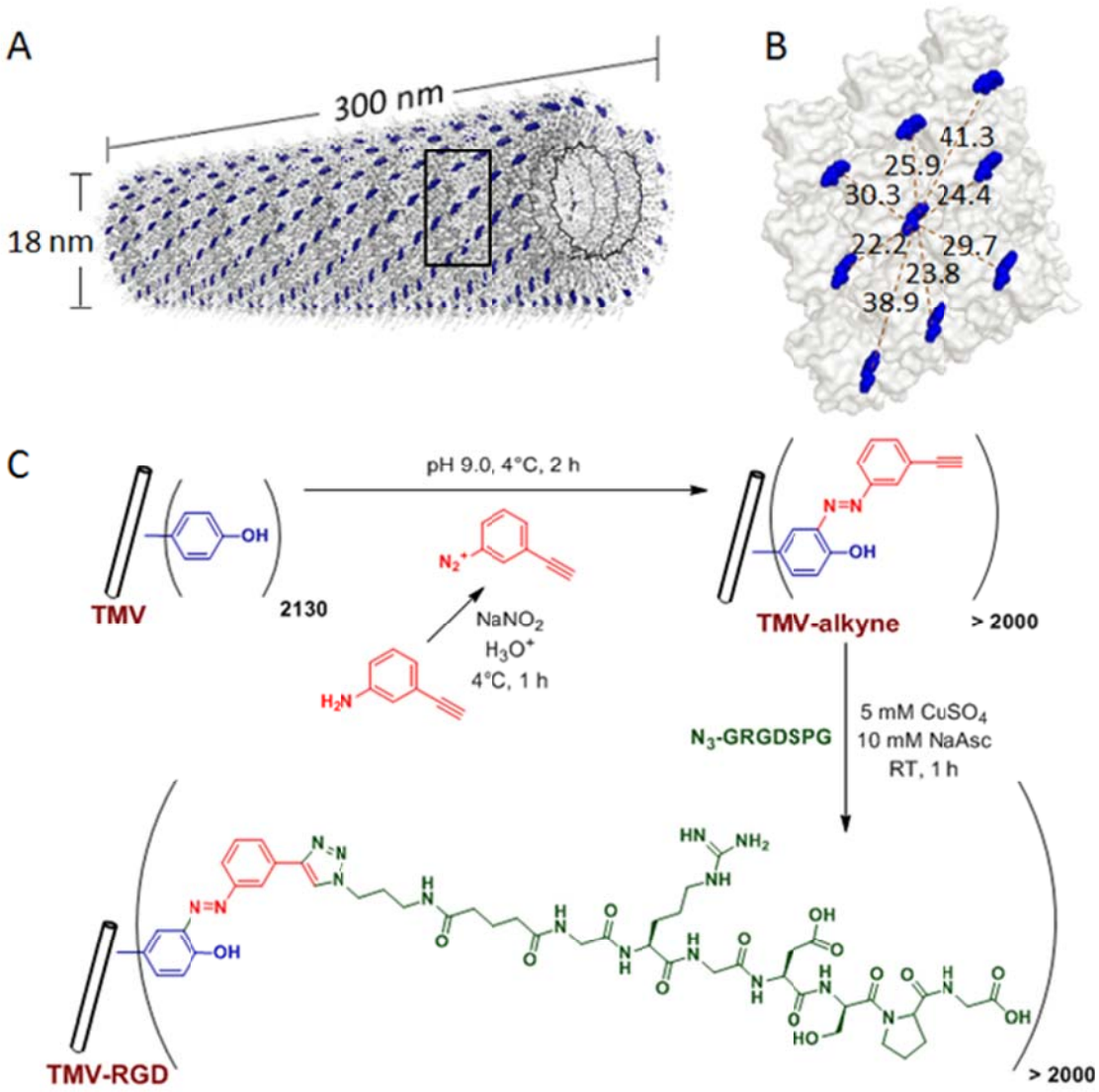

Figure 3.1 TMV structure and bioconjugation scheme. A) Computer reconstructed image showing TMV structure using PyMOL with coordinates from Protein Data Bank. The single stranded RNA inside TMV particle is represented by the black helix. The tyrosine 139 (Y139) residues of individual TMV coat proteins subunits are colored in blue while all other amino acid residues are washed out in gray. B) An enlarged portion of TMV coat protein (from the boxed area in (A)), showing possible distances (dashed red lines, measured in Angstroms) among the blue Y139. C) Scheme of the TMV bioconjugation reaction to tether RGD peptides via a CuAAC reaction to alkyne-functionalized Y139 residues.

protein 2 (BMP2), was significantly increased within 24 hours for cells cultured on substrates with TMV coating compared to cells cultured on uncoated substrates or cells supplemented with TMV in suspension [9]. One possible interpretation of this observation is that the topographical features created by TMV coating, compared to TMV in solution, plays a major role in the accelerated osteogenic differentiation. It has been previously recognized that cellular processes, such as adhesion, migration, proliferation, and apoptosis, could be influenced by biochemical and biophysical cues from the surrounding microenvironment [10]. For example, the nanoscale roughness of titanium surface implant can positively affect implant integration and bone differentiation [11-14]. In addition, the incorporation of growth factors [15-18], adhesion ligands [19-21], and osteoinductive compounds [22-25] into biomaterial surface can further accelerate the bone formation process. Given the lack of affinity of native TMV viral particles to mammalian cell surface, which resulted in low initial cell adhesion [9], we hypothesized that combining the topological features offered by TMV with cellular adhesion molecules could synergistically enhance the bone formation process of stem cells.

3.1.2 RGD incorporation to display a multivalent adhesive ligand

The tripeptide arginine-glycine-aspartic acid (RGD) present in many adhesive proteins in the ECM is a well-known general cell recognition motif via the cell surface integrin receptors [26]. These proteins include fibronectin, vitronectin, osteopontin, collagen, thrombospondin, fibrinogen, and von Willebrand factor [26]. Generally, the incorporation of RGD sequence into artificial scaffolds increases initial cell adhesion to the scaffold and cell spreading, thus improving tissue regeneration process. The spacing between

RGD motifs needs to be less than 440 nm to mediate fibroblast adhesion and spreading, and less than 140 nm to mediate focal adhesion assembly [27]. In another study, it was discovered that the RGD cluster spacings have a threshold less than 60 nm in order for NR6 fibroblasts to form focal adhesion and stress fiber [28]. Moreover, the threshold spacings are lower (closer) if there is less RGD clustering. In other words, at the same surface RGD density, the surface with RGD clusters present would provide greater cell adhesion strength [28]. Another study illustrated that integrin-mediated signalling requires RGD spacing of less than 58 nm [29]. A more recent study showed that focal adhesion complexes between cell-membrane integrins and cytoskeleton, responsible for signal transduction from external stimuli to the cell, were formed when RGD spacing is less than 44 nm in endothelial cells [30]. Specifically in the case of osteogenesis, there are several studies illustrating that the incorporation of RGD sequence into biomaterials improved bone differentiation and regeneration [20, 21, 31-33]. Especially, it was recently emphasized that a local clustering of RGD ligands is more essential than global RGD density [34, 35]. This clustering effect is believed to occur at an integrin-binding spacing less than an integrin itself, which has a size of 8-12 nm.

3.1.3 Bioconjugation via CuAAC reaction

Many viral nanoparticles have been employed to achieve RGD-displaying clustering, such as M13 bacteriophage [36-40], *Cowpea mosaic virus* [41], *Turnip yellow mosaic virus* [42, 43], including genetically modified TMV with RGD peptides [2, 8, 44]. In this study, we explore the feasibility of TMV functionalization with the copper catalyzed alkyne-azide cycloaddition (CuAAC) reaction to display RGD peptides and the influence

of RGD-presenting TMV, where RGD clustering is present (RGD spacing of 2-4 nm) (Figure 3.1B), on the osteogenic potential of bone marrow derived mesenchymal stem cells (BMSCs).

3.2 RESULTS AND DISCUSSION

3.2.1 TMV bioconjugation

The tyrosine residues (Y139) of TMV are viable for chemical ligation using electrophilic substitution reaction at the *ortho*-position of the phenol ring with diazonium salts [5]. TMV subunits are assembled in a highly regular helical structure, which resulted in uniform spacing between each subunits down to a nanometer scale. From coordinates provided by Protein Data Bank, the distance between neighboring Y139 residues of TMV coat proteins is calculated to be 2-4 nm apart as shown in Figure 3.1B. The CuAAC reaction has been confirmed to be a very efficient way to display functional groups on TMV in a controllable manner [4]. Following the reported protocol [4, 5], we first prepared the alkyne derived TMV particles (Figure 3.1C). MALDI-TOF MS analysis confirmed that >95% of the TMV capsid monomers were converted into TMV-alkyne (Figure 3.2A), consistent with a previous report [2]. MALDI-TOF MS analysis showed the correct mass shift for TMV-RGD indicating the CuAAC reaction was successful, (Figure 3.2A). The integrity of TMV-RGD was confirmed by AFM and TEM (Figure 3.2B). AFM images illustrated that the majority of TMV-RGD remained rod-shaped particles after the bioconjugation. The diameter observed under TEM ranged from 15-20 nm with lengths measuring approximately 300 nm, indicating the particles are intact after the two-step CuAAC reaction to Y139 (Figure 3.2B).

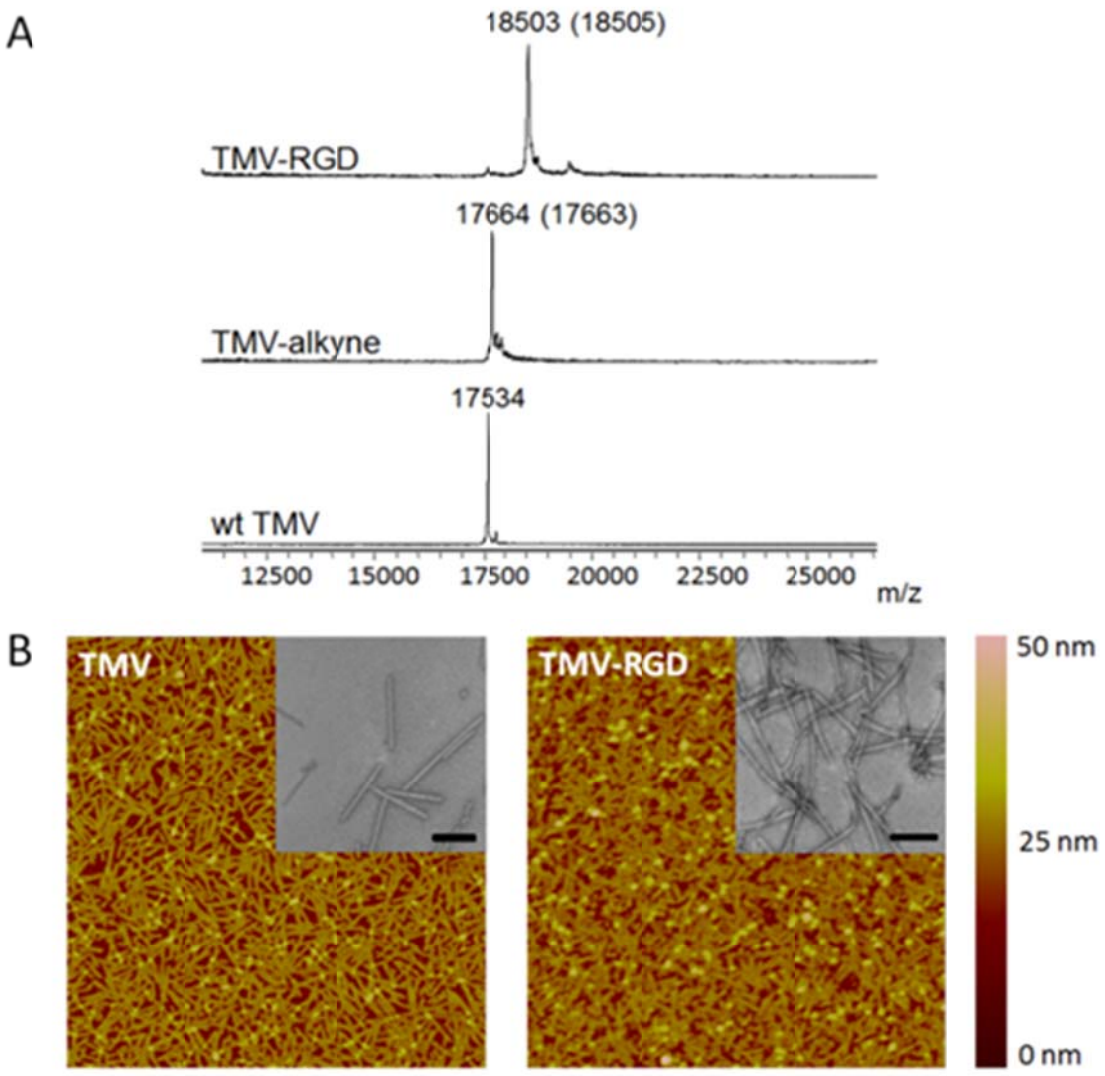

Figure 3.2 Characterization of TMV particles. **A**) MALDI-TOF MS spectra of the subunit protein of wild type TMV (17534 m/z), TMV-alkyne (17664 m/z) and the CuAAC reaction product TMV-RGD (18503 m/z). The numbers in parentheses refer to the theoretical masses. **B**) The morphology of TMV particles before (TMV) and after (TMV-RGD) bioconjugation visualized by AFM and TEM **(**insets). Scan areas of AFM are 5 µm × 5 µm; and scale bars of TEM are 200 nm.

3.2.2 BMSC adhesion on TMV and TMV-RGD

The effect of RGD-displaying TMV, as a polyvalent scaffold, on bone differentiation was explored. It has been demonstrated that unmodified TMV substrate accelerated osteogenesis by 7 days compared to standard tissue culture polystyrene (TCPS) control [6]. The chemical incorporation of phosphate functional groups to TMV further enhanced bone differentiation of BMSCs [7]. However, the interaction between BMSCs and TMV substrates were weak since the focal adhesion complexes were found to be significantly smaller than the control [9]. Since RGD ligand is known to promote cell attachment, the incorporation of RGD motifs into TMV based substrate is expected to increase the initial cell adhesion.

3.2.3 Biocompatibility

Prior to cell culture experiments, TMV and TMV-RGD were dialyzed several times against ultrapure water, due to concerns that residual Cu^{I} from the CuAAC reaction will affect cell viability. Optical images after 24 hours of cell seeding in Figure 3.3A revealed that BMSCs can adhere and spread on both TMV and TMV-RGD substrates. There were slightly more cells visualized on TMV-RGD compared to TMV coated surface. The numbers of adherent cells were calculated to elucidate the result in a quantitative manner (Figure 3.3B). As expected, the average cell numbers on TMV-RGD was higher than that of TMV. To verify that TMV-RGD does not have cytotoxicity from residual Cu^{I}, the proliferation of BMSCs on both virus scaffolds was examined over 22 days in osteogenic conditions (Figure 3.3C). The proliferation percentage of each sample was calculated based on the initial cell attachment as a 100%. BMSCs proliferated comparably well on

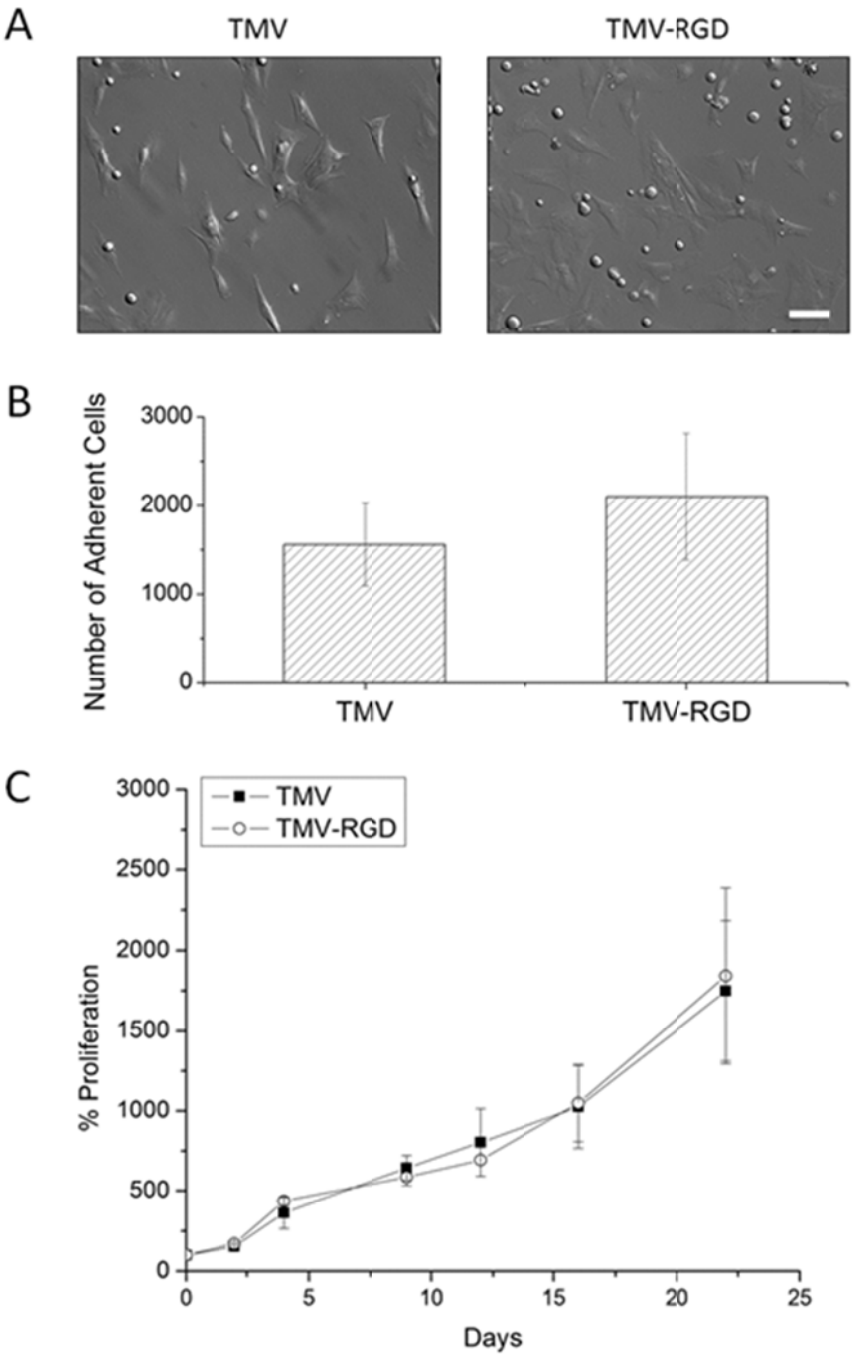

Figure 3.3 BMSC adhesion and viability on virus scaffolds. **A**) Optical images of BMSC attached on virus substrates after 24-hour seeding in primary media. Scale bar is 100 um. **B**) Number of adherent BMSCs on different virus substrates after 24-hour seeding in primary media. **C**) Proliferation percentage of BMSCs on TMV and TMV-RGD substrates over 22 days in osteogenic media. Error bars indicate ± 1 S.D.

both virus substrates, thus TMV-RGD did not exhibit any cytotoxicity to the *in vitro* cell culture.

3.2.4 Osteogenic potential of BMSCs on virus substrates

The differentiation potential of BMSCs was studied in order to substantiate the effect of RGD incorporation on osteogenesis. First, osteo-specific gene expression levels were quantified by RT-qPCR (Figure 3.4A). The expression levels are presented as fold change compared to BMSCs at day 0. There was no significant difference in the gene expression levels of alkaline phosphatase (*ALPL*), osteonectin (*SPARC*), and osteopontin (*SPP1*) over the three weeks. Another osteo-specific gene examined is osteocalcin (*BGLAP*), the most common marker of mature osteoblast, as this protein is only synthesized by fully-differentiated osteoblasts [45]. BGLAP is rich in acidic amino acids that are responsible for its high affinity to calcium ions [45], which are eventually accumulated in mineralized bone matrix by binding specifically to hydroxyapatite crystals [46]. It has been documented that *BGLAP*, which is normally peaked at day 21 on standard tissue culture plate substrate, is peaked at day 14 when BMSCs are grown on TMV scaffold, suggesting that TMV substrates accelerate the bone differentiation process by 7 days [6]. The gene expression analysis of BMSCs on unmodified TMV scaffolds in Figure 3.4A was in agreement with the previous report [6], where *BGLAP* gene expression level was peaked at day 14 indicating a complete mineralization of mature osteoblasts. As a comparison, the incorporation of RGD peptide into TMV subunits also significantly increased *BGLAP* gene expression level at day 14 (Figure 3.4A). The gene expression level of integrin-binding bone sialoprotein (*IBSP*), a secreted

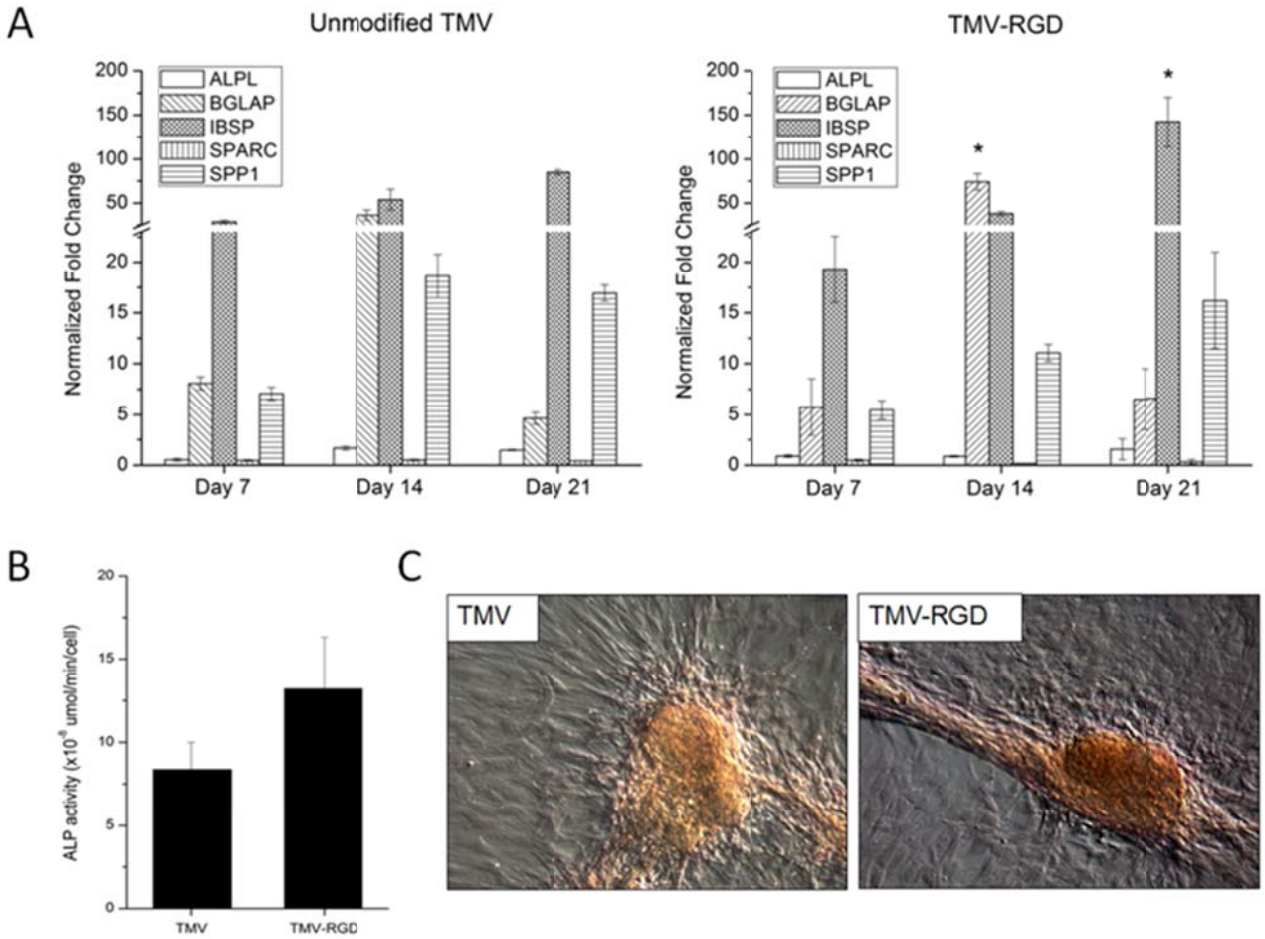

Figure 3.4 Osteogenic differentiation of BMSCs on TMV and TMV-RGD substrates. A) Osteo-specific gene expression profiles of BMSCs on TMV and TMV-RGD under osteogenic conditions over 21 days. For each sample, the profiles show 3 time points at 7, 14, and 21 days. Error bars indicate ±1 S.D. * $p < 0.05$. B) Alkaline phosphatase activity of cells on TMV and TMV-RGD at day 14. C) Optical images of Alizarin red S staining of cells cultured for 14 days on TMV or TMV-RGD substrate showing calcium deposition in red color.

ECM protein required for hydroxyapatite formation as well as collagen binding in mineralized tissues [47], was also evaluated. IBSP is synthesized just before calcification [45] and real time PCR results from the previous study indicated that BMSCs on TMV substrates had significantly higher *IBSP* mRNA expression within 24 hours while there was no change in *IBSP* mRNA expression levels in BMSCs on TCPS control [9]. In this experiment, *IBSP* expression levels in cells on both TMV and TMV-RGD were highly upregulated during the culture period (Figure 3.4A). However, BMSCs grown on TMV-RGD scaffolds expressed higher level of *IBSP* mRNA at day 21 when compared to those on native TMV scaffolds at the same time (Figure 3.4A).

In addition to the analysis of osteo specific gene expressions, alkaline phosphatase (ALP) activity was assessed. ALP is an early marker of osteogenesis and its activity mediates matrix mineralization. Although there was no difference in *ALPL* mRNA expressions at day 14 for cells grown on TMV compared to those on TMV-RGD as shown in Figure 3.4A, ALP enzyme activity assay showed a slight increase in BMSCs grown on TMV-RGD (Figure 3.4B). The staining for calcium deposition was also performed at day 14. A stronger staining was observed on TMV-RGD samples suggesting higher mineralization level (Figure 3.4C). This observation could be supported by previously mentioned increases in both *BGLAP* and *IBSP* mRNA expression levels (Figure 3.4A), possibly facilitating the formation of hydroxyapatite crystals leading to mineralized matrix.

3.3 CONCLUSION

The results demonstrate the feasibility of modulating mesenchymal stem cell differentiation on TMV-based scaffolds modified by CuAAC reaction. TMV was successfully modified with more than 95% conversion and the integrity of the virus particles was preserved. Scaffolds coated with TMV-RGD slightly improved initial BMSC adhesion, while maintaining the same cell proliferation rate with those coated with native TMV. The osteogenic differentiation of BMSCs was enhanced on TMV-RGD substrates since an increase in *BGLAP* and *IBSP* gene expression levels as well as mineralization level was observed. Future studies will focus on controlling ligand density and using a variety of ligands including small molecules and other peptides on viral scaffold to study structure-property relationship and modulate cell behaviour. It is also important that a recent development of copper-free Click reaction [48] may provide an alternative approach to chemically modify TMV without a concern about Cu^{I} contamination.

3.4 EXPERIMENTAL SECTION

3.4.1 TMV isolation, bioconjugation and characterization

TMV was isolated and purified according to a protocol previously reported [6, 7]. The schematic representation of TMV bioconjugation is shown in Figure 3.1C. The RGD-azide peptide was synthesized using solid-phase peptide synthesis. The peptides were purified with FPLC and characterized by LC/ESI mass spectrometry. The CuAAC reaction to modify tyrosine residues on the exterior surface of TMV is performed according to protocols established by Schlick *et al.*[5] and Bruckman *et al.* [4] with slight

modifications. Briefly, diazonium salt was synthesized as published previously [5]. TMV was treated with the diazonium salt generated *in situ* from 3-ethynylaniline at 4°C in a pH 9.0 buffer solution to form alkyne grafted TMV particle. Copper(I) catalyzed azide-alkyne cycloaddition (CuAAC) reaction was used to conjugate RGD-azide peptide to TMV particle [49]. The CuAAC reaction was done with concentration of TMV-alkyne at 3 mg/mL and peptide-azide at 2 mg/mL in Tris HCl buffer (10 mM, pH 7.8). After 1 hour incubation at room temperature, TMV-RGD was purified via a 10-50% sucrose gradient from which the light scattering region was collected. The modified virus was then pelleted using ultracentrifugation at 160,000 *g* for 2.5 hours at 4 ˚C. The pellet was dissolved in potassium phosphate buffer (10 mM, pH 7.4). MALDI-TOF mass spectrometry was used to confirm the modifications. The integrity of modified TMV particles was confirmed by AFM and TEM. The virus solutions were dialyzed against water prior to substrate coating.

3.4.2 Preparation of virus coated substrates

For cell culture experiments, 3-aminopropyltriethoxysilane (APTES) coated slides (Lab Scientific Inc.) were cut into 1.5 cm^2 wafers. The wafers were washed with ethanol before use. For virus coating, each wafer was coated with 0.2 mL of 0.2 mg/mL TMV or TMV-RGD solution diluted in water and the coated substrates were dried overnight in a sterile biosafety cabinet. The virus coverage on the wafers was characterized using tapping-mode AFM images using a NanoScope IIIA MultiMode AFM (Veeco). Si tips with a resonance frequency of approximately 300 kHz, a spring constant of about 40 N m^{-1} and a scan rate of 1.0 Hz were used.

3.4.3 BMSC isolation and expansion

Primary BMSCs were isolated from the bone marrow of young adult 80 g male Wister rats (Harlan Sprague Dawley, Inc.). The procedures were performed in accordance with the guidelines for animal experimentation by the Institutional Animal Care and Use Committee, School of Medicine, University of South Carolina. Cells were maintained in growth medium (DMEM supplemented with 10% fetal bovine serum (FBS), penicillin (100 U/mL), streptomycin (100 μg/mL) and amphotericin B (250 ng/mL)) and passaged no more than four times after isolation. To induce osteogenesis, growth media was replaced with osteogenic media consisting of DMEM supplemented with 10% FBS, penicillin (100 U/mL), streptomycin (100 μg/mL), amphotericin B (250 ng/mL), 10 mM sodium β-glycerophosphate, L-ascorbic acid 2-phosphate (50 μg/mL) and 10^{-8} M dexamethasone. Media was replenished every 3-4 days.

3.4.4 Cell proliferation

Substrates coated with TMV and TMV-RGD were seeded with 4×10^4 cells per substrate and cells were allowed to attach overnight in growth media. The media was then replaced with osteogenic media and cultured for 22 days. CellTiter Blue® assay (Promega) was used to determine number of cells at 0, 2, 4, 9, 12, 16, and 22 days after osteogenic induction. Cell proliferation was determined by normalizing CellTiter Blue fluorescence intensities against initial signal intensity on day 0, which is the day of osteogenic induction.

3.4.5 Quantitative real-time RT-PCR analysis

Virus coated wafers were seeded with 4×10^4 cells per wafer and cells were allowed to attach overnight in growth media. The unseeded cells were used as a control to normalize the change in gene expression. The media was replaced with osteogenic media and cultured for 7, 14, and 21 days. The cell cultures were terminated at these time points and total RNA was extracted using RNeasy mini purification kit (Qiagen). The quality and quantity of the extracted RNA was analyzed using Bio-Rad Experion (Bio-Rad Laboratories) and was reverse transcribed by using qScript™ cDNA Supermix (Quanta Biosciences). RT-qPCR (iQ5 real-time PCR detection system Bio-Rad Laboratories) was done by the method described as: 60 cycles of PCR (95˚C for 20s, 58˚C for 15 s, and 72˚C for 15s), after initial denaturation step of 5 minutes at 95˚C, by using 12.5 µL of iQ5 SYBR Green I Supermix, 2 pmol/µL of each forward and reverse primers and 0.5 µL cDNA templates in a final reaction volume of 25 µL. Glyceraldehyde 3-phosphate dehydrogenase (GAPDH) was used as the housekeeping gene. Data collection was enabled at 72˚C in each cycle and C_T (threshold cycle) values were calculated using the iQ5 optical system software version 2.1. The expression levels of differentiated genes and undifferentiated genes were calculated using Pfaffl's method (M.W. Pfaffl, G.W. Horgan and L. Dempfle, Relative expression software tool) for group-wise comparison and statistical analysis of relative expression results in real-time PCR, using GAPDH as the reference gene. Quantification of gene expression was based on the C_T value for each sample which was calculated as the average of three replicate measurements for each sample analyzed. "Pair Wise Fixed Reallocation Randomization Test" was performed on

each sample and a value of $p < 0.05$ was regarded as significant. The primers used for RT-qPCR are shown in Table 3.1.

3.4.6 Alkaline phosphatase activity

After 14 days in osteogenic cultures, CellTiter Blue® assay (Promega) was used to determine number of cells in each sample one hour prior to cell fixation. BMSCs seeded on TMV and TMV-RGD were fixed with 4% paraformaldehyde for 15 minutes at room temperature. To determine alkaline phosphatase (ALP) activity, each fixed samples were incubated in 500 μL of 1-Step™ *p*-nitrophenyl phosphate solution (Thermo Scientific) for 15 minutes at room temperature. Then the solution was transferred to a new microfuge tube with 250 μL of 2 N NaOH and the absorbance at 405 nm was measured. The measured ALP activity from each sample was normalized to the corresponding cell number.

3.4.7 Alizarin red staining

To visualize calcium deposition and to confirm osteogenic differentiation, fixed samples at day 14 were stained with 0.1% Alizarin red solution (Sigma-Aldrich) pH 4.1-4.5 for 30 minutes in the dark. The samples were washed with water (18.2 MΩ) prior to imaging.

Table 3.1 Primers used for RT-qPCR to measure gene expression levels. ALPL: alkaline phosphatase; BGLAP: osteocalcin; IBSP: integrin-binding sialoprotein; SPARC: osteonectin; SPP1: osteopontin.

Gene	Sequence (5'-3')
ALPL	Forward: ACCTCGAGCAGGAACAGAAGTTTGCT
	Reverse: TTCCATGATGGTTGCAGGGTCTGGA
BGLAP	Forward: AAAGCCCAGCGACTCT
	Reverse: CTAAACGGTGGTGCCATAGAT
GAPDH	Forward: ACTAAAGGGCATCCTGGGCTACACTGA
	Reverse: TGGGTGGTCCAGGGTTTCTTACTCCTT
IBSP	Forward: TCTGAACGGGTTTCAGCAGACGA
	Reverse: GCCATGCCCCTTGTAGTAGCTGTA
SPARC	Forward: AAACTTGGGCAAGGACGCTGTGA
	Reverse: ATGCCTCCCCTTGGCTCACCAAAAT
SPP1	Forward: GACGGCCGAGGTGATAGCTT
	Reverse: CATGGCTGGTCTTCCCGTTGC

3.5 REFERENCES

[1] Jiang L, Li Q, Li M, Zhou Z, Wu L, Fan J, et al. A modified TMV-based vector facilitates the expression of longer foreign epitopes in tobacco. Vaccine. 2006;24:109-15.

[2] Lee LA, Nguyen QL, Wu L, Horvath G, Nelson RS, Wang Q. Mutant Plant Viruses with Cell Binding Motifs Provide Differential Adhesion Strengths and Morphologies. Biomacromolecules. 2012;13:422-31.

[3] McCormick AA, Corbo TA, Wykoff-Clary S, Nguyen LV, Smith ML, Palmer KE, et al. TMV-peptide fusion vaccines induce cell-mediated immune responses and tumor protection in two murine models. Vaccine. 2006;24:6414-23.

[4] Bruckman MA, Kaur G, Lee LA, Xie F, Sepulveda J, Breitenkamp R, et al. Surface modification of tobacco mosaic virus with "Click" chemistry. ChemBioChem. 2008;9:519-23.

[5] Schlick TL, Ding Z, Kovacs EW, Francis MB. Dual-Surface Modification of the Tobacco Mosaic Virus. J Am Chem Soc. 2005;127:3718-23.

[6] Kaur G, Valarmathi MT, Potts JD, Jabbari E, Sabo-Attwood T, Wang Q. Regulation of osteogenic differentiation of rat bone marrow stromal cells on 2D nanorod substrates. Biomaterials. 2010;31:1732-41.

[7] Kaur G, Wang C, Sun J, Wang Q. The synergistic effects of multivalent ligand display and nanotopography on osteogenic differentiation of rat bone marrow stem cells. Biomaterials. 2010;31:5813-24.

[8] Luckanagul J, Lee LA, Nguyen QL, Sitasuwan P, Yang X, Shazly T, et al. Porous Alginate Hydrogel Functionalized with Virus as Three-Dimensional Scaffolds for Bone Differentiation. Biomacromolecules. 2012;13:3949-58.

[9] Sitasuwan P, Andrew Lee L, Bo P, Davis EN, Lin Y, Wang Q. A plant virus substrate induces early upregulation of BMP2 for rapid bone formation. Integr Biol. 2012;4:651-60.

[10] Curtis A, Wilkinson C. Topographical control of cells. Biomaterials. 1997;18:1573-83.

[11] Lossdörfer S, Schwartz Z, Wang L, Lohmann CH, Turner JD, Wieland M, et al. Microrough implant surface topographies increase osteogenesis by reducing osteoclast formation and activity. J Biomed Mater Res Part A. 2004;70A:361-9.

[12] Mozumder MS, Zhu J, Perinpanayagam H. Titania-polymeric powder coatings with nano-topography support enhanced human mesenchymal cell responses. J Biomed Mater Res Part A. 2012;100A:2695-709.

[13] Olivares-Navarrete R, Gittens RA, Schneider JM, Hyzy SL, Haithcock DA, Ullrich PF, et al. Osteoblasts exhibit a more differentiated phenotype and increased bone morphogenetic protein production on titanium alloy substrates than on poly-ether-ether-ketone. Spine. 2012;12:265-72.

[14] Zhuang LF, Jiang HH, Qiao SC, Appert C, Si MS, Gu YX, et al. The roles of extracellular signal-regulated kinase 1/2 pathway in regulating osteogenic differentiation of murine preosteoblasts MC3T3-E1 cells on roughened titanium surfaces. J Biomed Mater Res Part A. 2012;100A:125-33.

[15] Crouzier T, Sailhan Fdr, Becquart P, Guillot R, Logeart-Avramoglou D, Picart C. The performance of BMP-2 loaded TCP/HAP porous ceramics with a polyelectrolyte multilayer film coating. Biomaterials. 2011;32:7543-54.

[16] Kopf J, Petersen A, Duda GN, Knaus P. BMP2 and mechanical loading cooperatively regulate immediate early signalling events in the BMP pathway. BMC biology. 2012;10:37.

[17] Lee SS, Huang BJ, Kaltz SR, Sur S, Newcomb CJ, Stock SR, et al. Bone regeneration with low dose BMP-2 amplified by biomimetic supramolecular nanofibers within collagen scaffolds. Biomaterials. 2013;34:452-9.

[18] Wang X, Oyane A, Tsurushima H, Sogo Y, Li X, Ito A. BMP-2 and ALP gene expression induced by a BMP-2 gene-fibronectin-apatite composite layer. Biomed Mater. 2011;6:045004.

[19] Duggal S, Fronsdal KB, Szoke K, Shahdadfar A, Melvik JE, Brinchmann JE. Phenotype and gene expression of human mesenchymal stem cells in alginate scaffolds. Tissue Eng Part A. 2009;15:1763-73.

[20] Qu Z, Yan J, Li B, Zhuang J, Huang Y. Improving bone marrow stromal cell attachment on chitosan/hydroxyapatite scaffolds by an immobilized RGD peptide. Biomed Mater. 2011;5:065001.

[21] Shin H, Temenoff JS, Bowden GC, Zygourakis K, Farach-Carson MC, Yaszemski MJ, et al. Osteogenic differentiation of rat bone marrow stromal cells cultured on Arg–Gly–Asp modified hydrogels without dexamethasone and β-glycerol phosphate. Biomaterials. 2005;26:3645-54.

[22] Cameron K, Travers P, Chander C, Buckland T, Campion C, Noble B. Directed osteogenic differentiation of human mesenchymal stem/precursor cells on silicate substituted calcium phosphate. J Biomed Mater Res Part A. 2013;101A:13-22.

[23] Hao J, Kuroda S, Ohya K, Bartakova S, Aoki H, Kasugai S. Enhanced osteoblast and osteoclast responses to a thin film sputtered hydroxyapatite coating. J Mater Sci: Mater Med. 2011;22:1489-99.

[24] Shu R, McMullen R, Baumann MJ, McCabe LR. Hydroxyapatite accelerates differentiation and suppresses growth of MC3T3-E1 osteoblasts. J Biomed Mater Res Part A. 2003;67A:1196-204.

[25] Verma D, Katti KS, Katti DR. Osteoblast adhesion, proliferation and growth on polyelectrolyte complex-hydroxyapatite nanocomposites. Philos Transact A Math Phys Eng Sci. 2010;368:2083-97.

[26] Ruoslahti E, Pierschbacher MD. New Perspectives in Cell Adhesion: RGD and Integrins. Science. 1987;238:491-7.

[27] Massia SP, Hubbell JA. An RGD spacing of 440 nm is sufficient for integrin alpha V beta 3-mediated fibroblast spreading and 140 nm for focal contact and stress fiber formation. J Cell Biol. 1991;114:1089-100.

[28] Maheshwari G, Brown G, Lauffenburger DA, Wells A, Griffith LG. Cell adhesion and motility depend on nanoscale RGD clustering. J Cell Sci. 2000;113:1677-86.

[29] Cavalcanti-Adam EA, Micoulet A, Blümmel J, Auernheimer J, Kessler H, Spatz JP. Lateral spacing of integrin ligands influences cell spreading and focal adhesion assembly. Eur J Cell Biol. 2006;85:219-24.

[30] Le Saux G, Magenau A, Böcking T, Gaus K, Gooding JJ. The relative importance of topography and RGD ligand density for endothelial cell adhesion. PLoS One. 2011;6:e21869.

[31] Anderson JM, Vines JB, Patterson JL, Chen H, Javed A, Jun H-W. Osteogenic differentiation of human mesenchymal stem cells synergistically enhanced by biomimetic peptide amphiphiles combined with conditioned medium. Acta Biomater. 2010;7:675-82.

[32] Peng R, Yao X, Ding J. Effect of cell anisotropy on differentiation of stem cells on micropatterned surfaces through the controlled single cell adhesion. Biomaterials. 2011;32:8048-57.

[33] Shin H, Zygourakis K, Farach-Carson MC, Yaszemski MJ, Mikos AG. Modulation of differentiation and mineralization of marrow stromal cells cultured on biomimetic hydrogels modified with Arg-Gly-Asp containing peptides. J Biomed Mater Res, Part A. 2004;69A:535-43.

[34] Deeg JA, Louban I, Aydin D, Selhuber-Unkel C, Kessler H, Spatz JP. Impact of Local versus Global Ligand Density on Cellular Adhesion. Nano Lett. 2011;11:1469-76.

[35] Wang X, Yan C, Ye K, He Y, Li Z, Ding J. Effect of RGD nanospacing on differentiation of stem cells. Biomaterials. 2013;34:2865-74.

[36] Chung W-J, Merzlyak A, Yoo SY, Lee S-W. Genetically Engineered Liquid-Crystalline Viral Films for Directing Neural Cell Growth. Langmuir. 2010;26:9885-90.

[37] Merzlyak A, Indrakanti S, Lee S-W. Genetically Engineered Nanofiber-Like Viruses For Tissue Regenerating Materials. Nano Lett. 2009;9:846-52.

[38] Rong J, Lee LA, Li K, Harp B, Mello CM, Niu Z, et al. Oriented cell growth on self-assembled bacteriophage M13 thin films. Chem Commun (Cambridge, U K). 2008:5185-7.

[39] Souza GR, Christianson DR, Staquicini FI, Ozawa MG, Snyder EY, Sidman RL, et al. Networks of gold nanoparticles and bacteriophage as biological sensors and cell-targeting agents. Proc Natl Acad Sci U S A. 2006;103:1215-20.

[40] Wang J, Wang L, Li X, Mao C. Virus activated artificial ECM induces the osteoblastic differentiation of mesenchymal stem cells without osteogenic supplements. Scientific reports. 2013;3:1242.

[41] Hovlid ML, Steinmetz NF, Laufer B, Lau JL, Kuzelka J, Wang Q, et al. Guiding plant virus particles to integrin-displaying cells. Nanoscale. 2012;4:3698-705.

[42] Zan X, Sitasuwan P, Powell J, Dreher TW, Wang Q. Polyvalent display of RGD motifs on turnip yellow mosaic virus for enhanced stem cell adhesion and spreading. Acta Biomater. 2012;8:2978-85.

[43] Zeng Q, Saha S, Lee LA, Barnhill H, Oxsher J, Dreher T, et al. Chemoselective Modification of Turnip Yellow Mosaic Virus by Cu(I) Catalyzed Azide−Alkyne 1,3-Dipolar Cycloaddition Reaction and Its Application in Cell Binding. Bioconjugate Chem. 2011;22:58-66.

[44] Lee LA, Muhammad SM, Nguyen QL, Sitasuwan P, Horvath G, Wang Q. Multivalent Ligand Displayed on Plant Virus Induces Rapid Onset of Bone Differentiation. Mol Pharm. 2012;9:2121-5.

[45] Fujisawa R, Tamura M. Acidic bone matrix proteins and their roles in calcification. Front Biosci. 2012;17:1891-903.

[46] Owen TA, Aronow M, Shalhoub V, Barone LM, Wilming L, Tassinari MS, et al. Progressive development of the rat osteoblast phenotype in vitro: Reciprocal relationships in expression of genes associated with osteoblast proliferation and differentiation during formation of the bone extracellular matrix. J Cell Physiol. 1990;143:420-30.

[47] Ogata Y. Bone sialoprotein and its transcriptional regulatory mechanism. J Periodontal Res. 2008;43:127-35.

[48] Lallana E, Riguera R, Fernandez-Megia E. Reliable and Efficient Procedures for the Conjugation of Biomolecules through Huisgen Azide–Alkyne Cycloadditions. Angew Chem, Int Ed. 2011;50:8794-804.

[49] Wang Q, Chan TR, Hilgraf R, Fokin VV, Sharpless KB, Finn MG. Bioconjugation by Copper(I)-Catalyzed Azide-Alkyne [3 + 2] Cycloaddition. J Am Chem Soc. 2003;125:3192-3.

CHAPTER 4

MANIPULATION OF TMV STRUCTURE ON 2D SURFACE TO STUDY THE EFFECTS ON BONE DIFFERENTIATION

4.1 INTRODUCTION

4.1.1 Bone marrow derived mesenchymal stem cells

Stem cell fate is dependent on the surrounding stimuli, including both soluble and insoluble factors. How stem cells respond to different nanoscale cues has been extensively studied for tissue engineering and regenerative medicine applications [1-4]. There are several reports indicating that stem cell differentiation can be dictated at the nanometer level [5-14]. Bone marrow derived mesenchymal stem cells (BMSCs) are from the non-hematopoietic sub-population of bone marrow stroma [15-17], which have the ability to self-renew and differentiate to various lineages, such as adipocytes, osteocytes, chondrocytes, hepatocytes, neurons, muscle cells, and epithelial cells [17-22]. The pluripotent potential of BMSCs, ease of isolation, rapid expansion [23], and less controversial use than embryonic stem cells make this cell type an ideal source of adult stem cells to study material-mediated differentiation.

4.1.2 Plant virus-based substrate accelerates osteogenesis

Recently, we have reported accelerated osteogenic differentiation for BMSCs grown on plant virus coated substrates in comparison to cells cultured on conventional tissue culture plastic (TCP) [24, 25]. Two different plant viruses were employed in those

studies, i.e. spherical *Turnip yellow mosaic virus* (TYMV) and rod-like *Tobacco mosaic virus* (TMV). In both situations, several key mRNA markers associated with bone differentiation peaked at day 14 for cells on virus-coated substrates, whereas the cells on conventional plates required an additional 7 days to reach similar expression profiles [24, 25]. Moreover, immunohistochemical staining for osteoblastic specific differentiation markers, osteocalcin, osteonectin, and osteopontin, had supported the gene expression profiles on day 14. The expression of such osteogenic markers were further enhanced upon chemically modifying the virus with phosphates as indicated by increased Ca^{2+} mineralization and even higher mRNA expression levels of osteocalcin [26]. More importantly, our recent report illustrated that the roughness of TMV-coated substrate induced an early upregulation of endogenous levels of bone morphogenetic protein-2 (BMP2), which is the most potent bone inducing agent, through the disruption of actin and the reduction in focal adhesion size [27].

4.1.3 Tobacco mosaic virus for substrate coating

TMV is a rod-shaped particle measuring 300 nm in length with a diameter of 18 nm. The shape of the plant virus resembles the size scales of fibrillar extracellular matrix (ECM) protein, such as collagen. The viral capsid consists of 2130 identical coat protein subunits assembled in a helical structure around the single stranded genomic RNA. The production of TMV is cost effective and the resulting viral particles are highly uniform in size. The ability of TMV to be easily and uniformly manipulated via chemical [26, 28, 29] and genetic modifications [30-32] has gained traction as novel biomaterials for potential tissue engineering applications [33-38]. Herein, we attempt to manipulate TMV

nanostructure in order to study the nano-scale roughness effect on osteogenesis of BMSCs. The results suggested that nanorod structure of TMV is important to induce BMP2 upregulation.

Besides the nano-scale roughness generated from TMV coating, it is important to keep in mind that the native rod-like structure of TMV contains phosphate groups from its genomic RNA and calcium ion (Ca^{2+})-binding sites at the carboxyl cage between the RNA and the vertical helix of TMV coat protein (CP) present at the interior surface of the virus [39]. These distinct chemical properties of TMV may facilitate the bone mineralization, which are the formation of calcium phosphate crystals, and could contribute to the accelerated bone formation observed previously [25, 27]. By removing the RNA of TMV in order to disassemble TMV particles into CP subunits, the contribution of RNA phosphate groups on osteogenic differentiation can be excluded. Furthermore, it has been documented that the Ca^{2+}-binding capability of TMV is decreased when the dissociated TMV CPs formed the double-disk aggregate, due to the protein conformational change making the carboxyl cage unstable [40]. The helical aggregate of the isolated TMV CP can only preserve the Ca^{2+}-binding site at its iso-ionic point (pH 4.3-4.6) [41, 42]. Therefore, under cell culture conditions (pH higher than the iso-ionic point of TMV), TMV CP aggregate would not be able to bind Ca^{2+}.

4.2 RESULTS AND DISCUSSION

4.2.1 Preparation of TMV coat protein

The structure of TMV can be manipulated based on ionic strength and pH of solvent[43] and it has been summarized by Klug *et al.* [44]. Firstly, TMV whose structure is stabilized by its internal RNA was broken apart into CP in acetic acid and RNA was removed. Then TMV CP was suspended in either 10 mM Tris-HCl buffer (TMV CP in Tris) or water (TMV CP in water). Figure 4.1 presents AFM and TEM images of native TMV compared to TMV CP in Tris and TMV CP in water. Native TMV showed rod-shape nanoparticles with an average length of 300 nm, whereas TMV CP in Tris showed individual CP subunits without assembly and TMV CP in water showed long nanofibers with lengths more than 1 μm.

4.2.2 BMSC morphologies on different virus structures

The morphological differences of BMSCs on TCP, silanized glass with or without TMV of different structures were imaged at day 14 after seeding. BMSCs grown in osteogenic media all showed calcium nodule formation while those grown on TCP in growth media did not (Figure 4.2). The morphological images were not sufficient to distinguish osteogenic potential of substrates coated with different TMV structures.

4.2.3 Osteo-specific gene expressions

The ability of TMV substrate to accelerate osteogenesis of BMSCs from 21 days to 14 days has been documented previously [24]. Osteogenic gene markers were studied to study osteogenic potential of TMV with different nanostructure. *BGLAP*, or osteocalcin, is a marker of mature osteoblast. As expected, cells on native TMV coating showed the highest expression level of *BGLAP*, while cells on TCP and silanized glass controls did

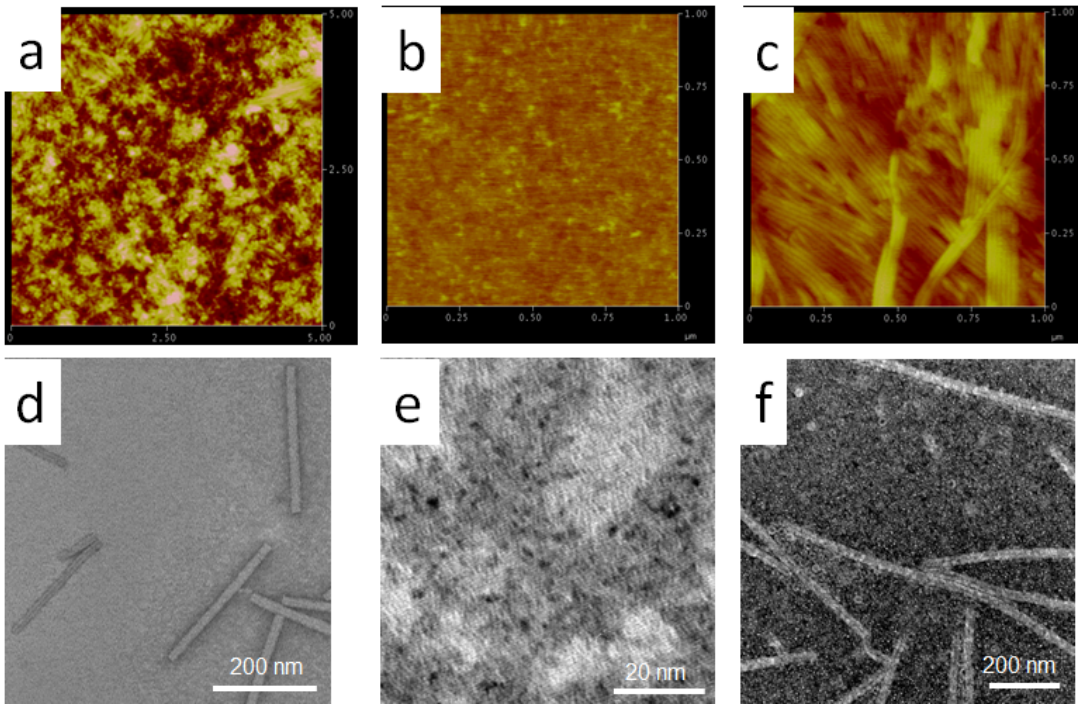

Figure 4.1 TMV structures visualized by AFM (a-c) and TEM (d-f): native TMV (a, d), TMV CP in Tris (b, e), and TMV CP in water (c, f). The AFM scanning size is 5 µm × 5 µm for (a) and 1 µm × 1 µm for (b, c). The scale bars represent 200 nm for (d, f) and 20 nm for (e).

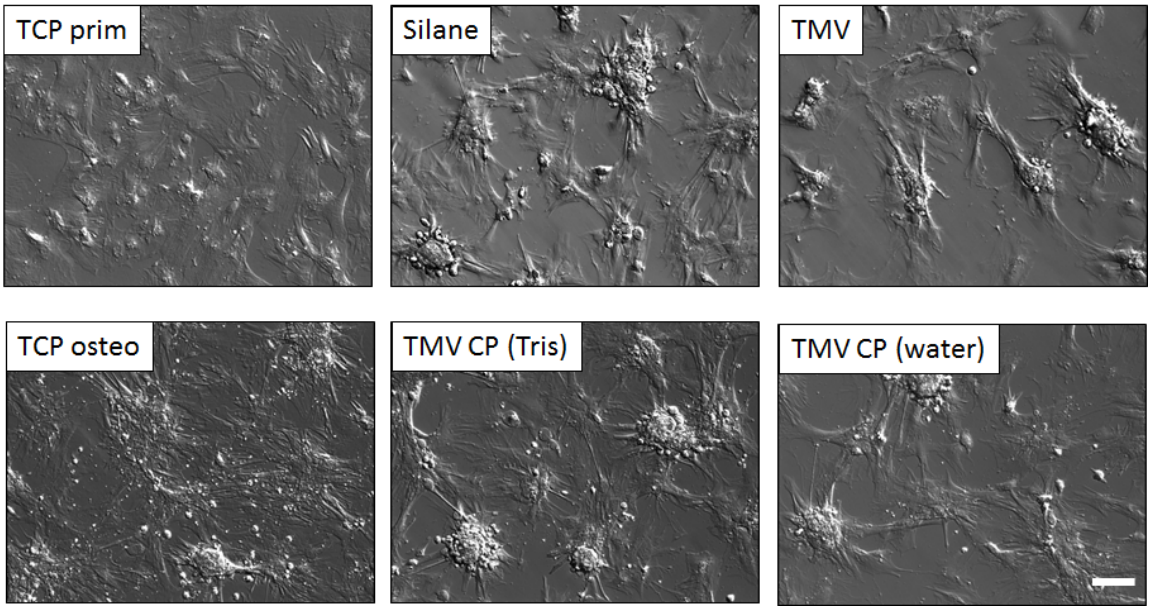

Figure 4.2 Differential interference contrast (DIC) images of BMSCs on TCP, silanized glass and TMV substrates at day 14 after seeding. All culture was in osteogenic media, except TCP prim which was in growth media. Scale bar is 100 µm.

not show an increase in *BGLAP* expression level (Figure 4.3). BMSCs on TMV CP in Tris and TMV CP in water had a slight increase in BGLAP expression, but not as high as native TMV (Figure 4.3). In addition to increased BGLAP, mRNA levels for integrin-binding sialoprotein (*IBSP*), a secreted extracellular matrix protein required for hydroxyapatite formation, increased in all samples compared to uninduced BMSCs on TCP control (Figure 4.3). *IBSP* expression level was the highest in BMSCs on native TMV, suggesting that the rod-shape nanostructure of TMV plays a major role in improving bone regeneration process. There was no difference in osteopontin (*SPP1*) mRNA levels at day 14 after osteo-induction. It was hypothesized that TMV CP in water would result in a similar effect to native TMV because it formed long nanofibers, however it didn't behave the same way as intact TMV.

4.2.4 Instability of TMV CP reassembled in water

The stability of virus coating with native TMV, TMV CP in Tris, and TMV CP in water were tested since gene expression experiment was unexpected. The surface coating of TMV and TMV CP in Tris remained the same after incubation in phosphate buffered saline (PBS) at cell culture conditions for 24 hours (Figure 4.4). However, the surface topography of TMV CP in water changed after PBS incubation, indicating that the reassembled TMV CP nanofibers without RNA could disassemble even after coated on silanized glass (Figure 4.4). This instability of TMV CP in water explained the unexpected result which was similar to disassembled TMV CP in Tris (Figure 4.3).

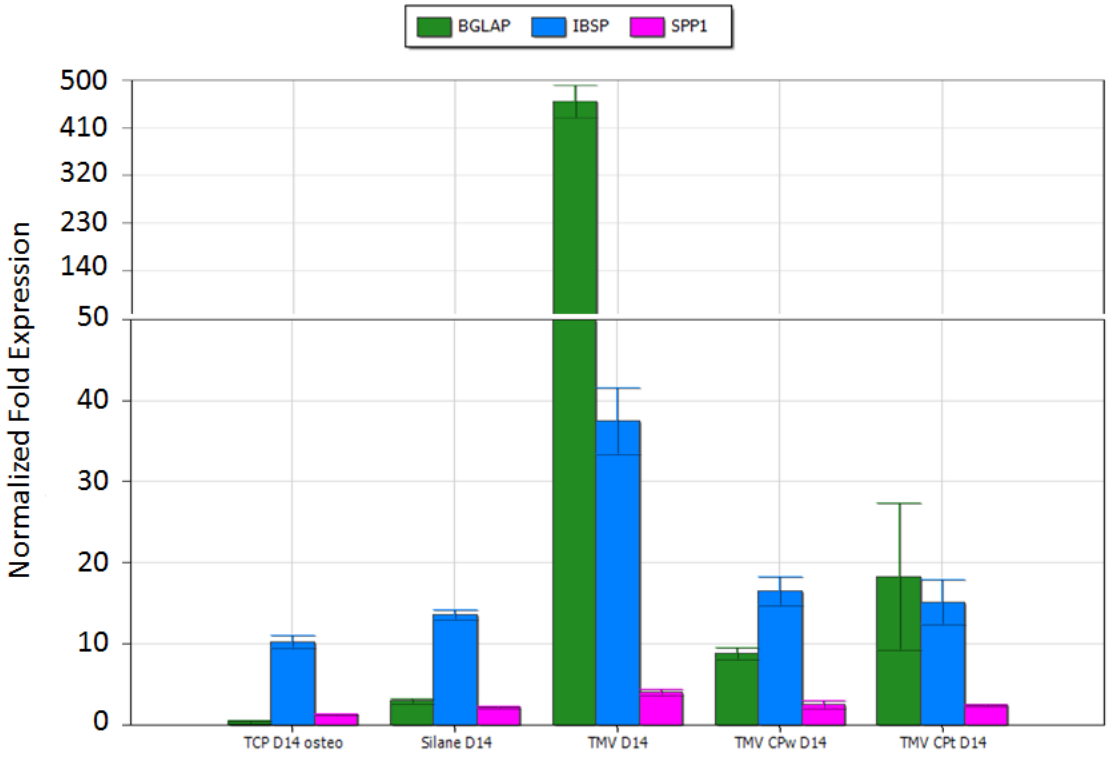

Figure 4.3 RT-qPCR analysis for osteo-specific gene expression of BMSCs under osteogenic conditions for 14 days.

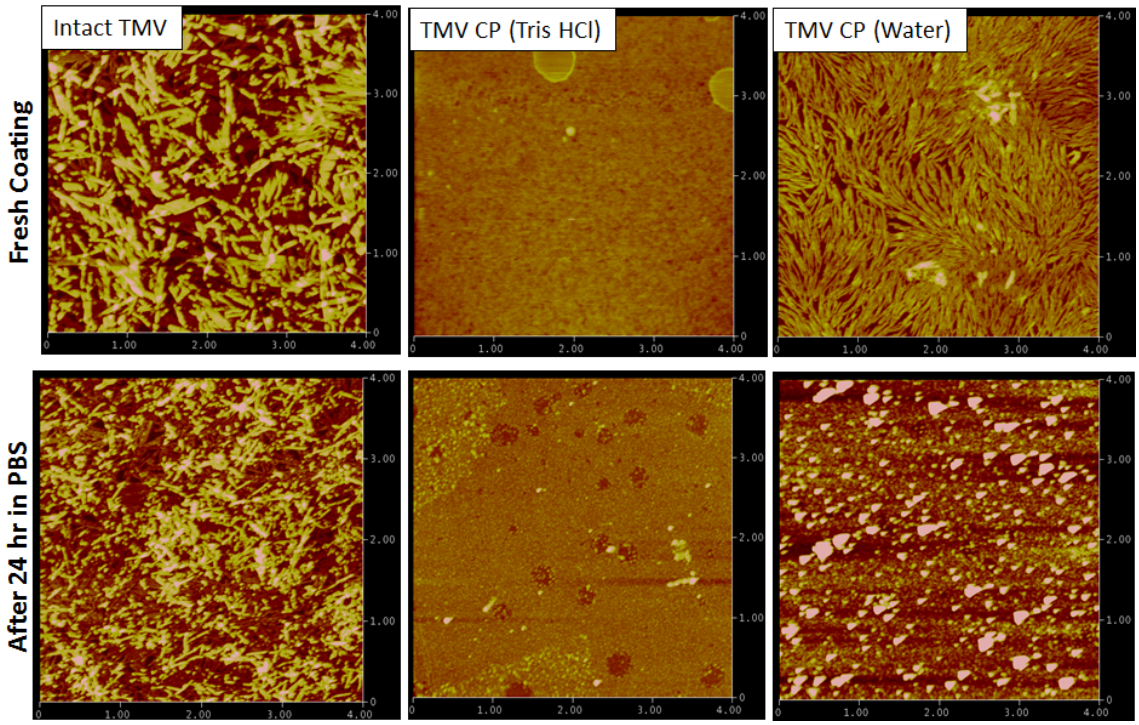

Figure 4.4 AFM images representing coating of different TMV structures before and after incubation with PBS for 24 hours at 37°C. The scan size is 4 µm × 4 µm for all images.

4.2.5 Thermal denaturation of TMV in water to form spherical nanoparticles (SNPs)

Recently, it has been demonstrated that TMV is able to change shape from nanorods into SNPs by thermal denaturation [45]. However, it was not well documented which solvent was used during the denaturation process. Here, TMV was suspended in either 0.1 M Kphos pH 7.8 or water at different virus concentrations to identify conditions in which SNPs can be generated. Figure 4.5 showed that SNPs were only formed when TMV was suspended in water. The size of SNPs was not depending on the virus concentration because AFM and DLS showed the same size of SNPs at all virus concentrations. Viral nanoparticles were visualized with TEM (Figure 4.6).

4.2.6 Stability of TMV SNP for cell culture experiment

The stability of TMV SNP coating was tested by incubating in PBS at cell culture conditions and AFM was performed to check the coating surfaces before and after PBS incubation. From Figure 4.7, it could be seen that SNPs were still on the surface after the incubation, which confirmed the coating stability.

4.2.7 BMSC morphologies at 24 hours after seeding

BMSCs exhibited different morphologies upon attaching onto TCP, silane, TMV, TMV CP, and TMV SNP at 24 hours after seeding. Cells attached well and spread out on TCP, silane, and TMV CP, which are flat and smooth (Figure 4.8). On the other hand, cells on TMV showed the formation of nodules as reported previously [27]. Surprisingly, TMV SNP coating that has higher surface roughness resulted in loose cell attachment and no

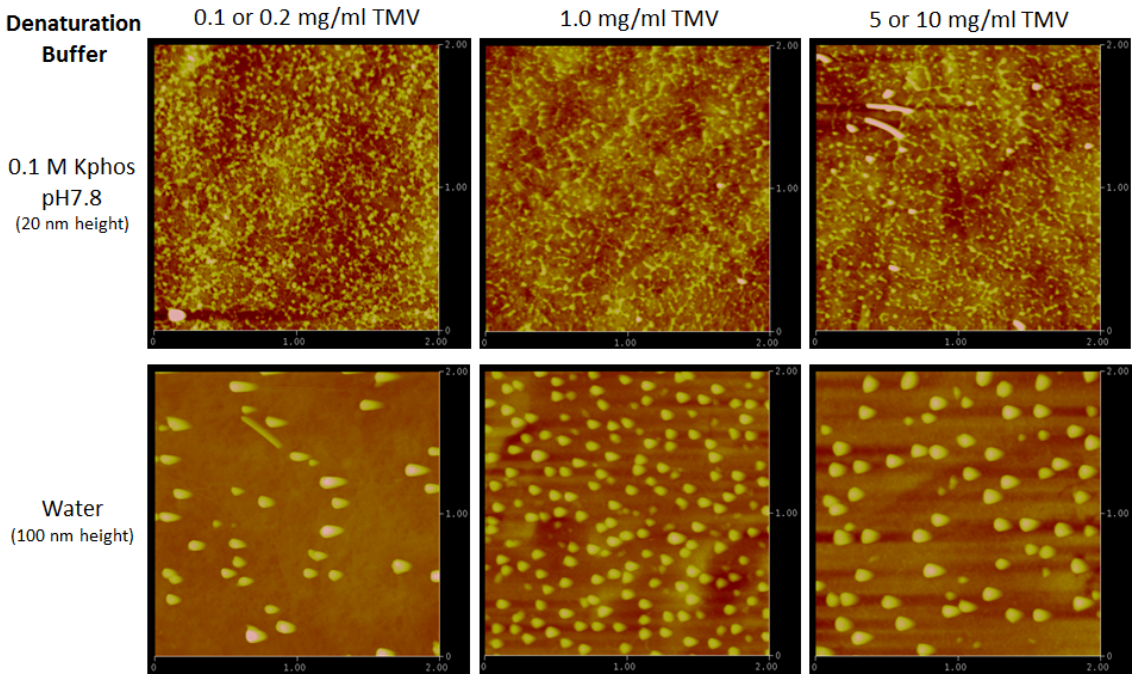

Figure 4.5 AFM images representing thermal denatured TMV in 0.1 M Kphos pH 7.8 (top row) and TMV in water (bottom row) at different virus concentrations; 0.1-0.2 mg/mL, 1 mg/mL, and 5 or 10 mg/mL. Thermal denaturation of TMV in water result in the formation of SNPs. The scan size is 2 µm × 2 µm. The height profiles are 20 nm for top row and 100 nm for bottom row.

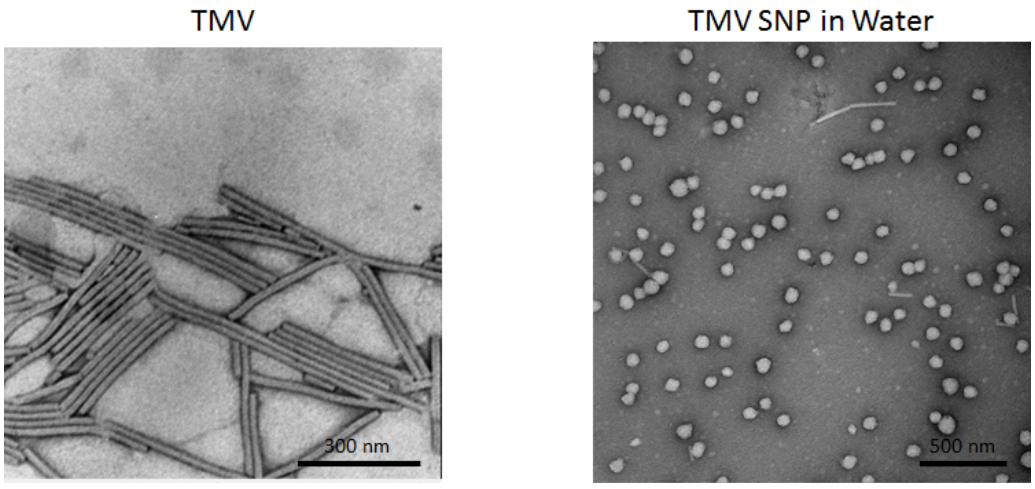

Figure 4.6 TEM images of native TMV nanorods and TMV SNP generated in water. The scale bars are 300 nm for TMV and 500 nm for TMV SNP.

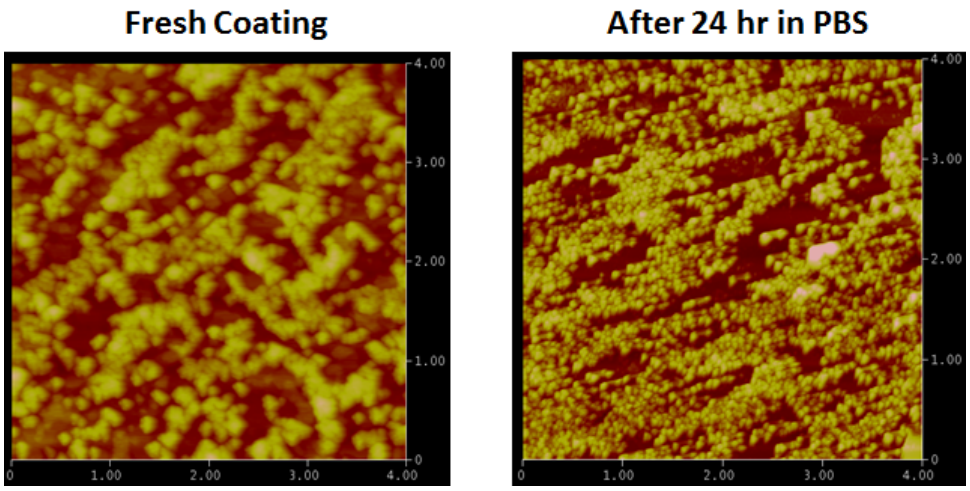

Figure 4.7 AFM images of TMV SNP coating on silane glass before and after incubation with PBS for 24 hours at 37°C. The scan size is 4 μm × 4 μm and the height profile is 100 nm.

spreading (Figure 4.8). It is believed that too high surface roughness is not optimal for adhesion of certain cell types. The osteogenic potential of BMSCs on TMV SNP substrate could not be studied because the cells slowly detached from culture surface over time.

4.3 CONCLUSION

TMV nanostructure can be manipulated by reassembling TMV CP in solvents with different ionic strength and pH. TMV CP is kept in individual subunits when dissolved in salt buffer with pH higher than 8.0 and it reassembled into long nanofibers when reducing ionic strength and lower pH (e.g. water). Since this assembling process is reversible, the coating of TMV CP in water was not stable in PBS and cell culture conditions, resulting in similar cellular responses to TMV CP in Tris. Moreover, TMV nanorods can be transformed into SNPs by thermal denaturation. SNPs were generated with homogenous size distribution in water, not depending on virus concentration. The coating of TMV SNPs was confirmed to be stable for cell culture experiment, however, BMSCs did not attach well due to the high surface roughness of SNP coating.

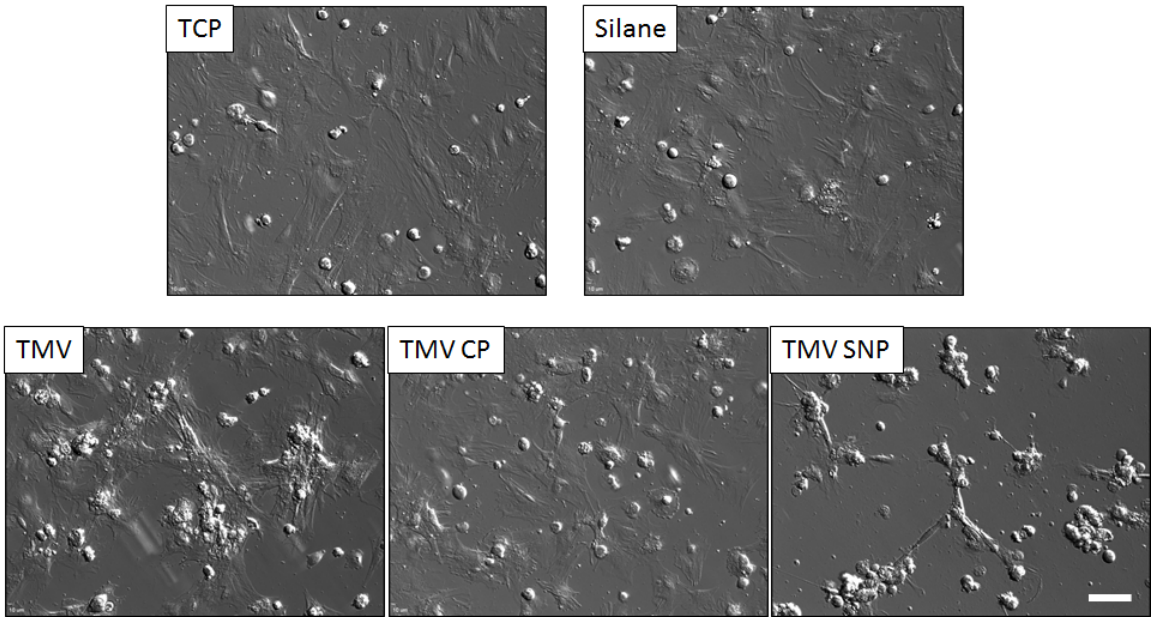

Figure 4.8 Differential interference contrast (DIC) images of BMSCs on TCP, silanized glass (silane), TMV, TMV CP in Tris (TMV CP), and TMV SNP substrates at 24 hours after seeding. Scale bar is 100 µm.

4.4 EXPERIMENTAL SECTION

4.4.1 TMV Isolation

TMV was isolated and purified according to a protocol previously reported [24, 26].

4.4.2 TMV CP isolation

Two volumes of concentrated acetic acid were added to 1 volume of 10-30 mg/mL of TMV in 10 mM potassium phosphate buffer pH 7.4. The mixture was incubated on ice for 15 minutes and RNA was pelleted down at full speed at 4˚C for 10 min. The supernatant was further desalted into 1% acetic acid by FPLC using Sephadex G-25 (Sigma Aldrich) column. Then 1 mL aliquots of 100 mM Kphos pH 7.4 were added to the collected TMV CP fraction until the solution became cloudy. The solution was incubated at 4˚C for 1-2 hours and then TMV CP precipitate was pelleted down at 15,000 *g* at 4˚C for 10 minutes. TMV CP pellet was resuspended in 0.1 M potassium hydroxide with 10 mM dithiothreitol and dialyzed against 100 mM Tris-HCl pH 8.0 or water at 4˚C overnight.

4.4.3 Generation of TMV SNP

Native TMV was diluted in either 0.1 M Kphos buffer pH 7.8 or water at concentrations of 0.1, 0.2, 1, 5, 10 mg/mL. The virus solutions were heated at 98°C for at least 10 minutes as previously reported [45]. The cloudy solutions were obtained, but the solutions with 0.1 M Kphos buffer resulted in more precipitation.

4.4.4 Virus coating and imaging

APTES coated slides (Lab Scientific Inc.) were cut into 1.5 cm^2 wafers and were sterilized with ethanol before use. For surface coating, the wafers were coated with 0.2 mg/mL TMV, TMV SNP, or TMV CP diluted in water or 10 mM Tris-HCl pH 8.0 buffer. The coated substrates were dried overnight in a sterile biosafety cabinet. The virus coverage on the wafers was characterized using tapping-mode atomic force microscope (AFM) images using a NanoScope IIIA MultiMode AFM (Veeco). Si tips with a resonance frequency of approximately 300 kHz, a spring constant of about 40 N m^{-1} and a scan rate of 0.5 Hz were used. TMV nanoparticles were stained with 2% uranyl acetate and visualized by transmission electron microscope (TEM).

Wafers coated with TMV, TMV CP in Tris, and TMV CP in water were incubated in PBS at 37°C for 24 hours. Before AFM imaging to check stability of virus coating, the wafers were washed with water and dry with nitrogen stream.

4.4.5 BMSC isolation and expansion

Primary BMSCs were isolated from the bone marrow of young adult 80 g male Wister rats (Harlan Sprague Dawley, Inc.). The procedures were performed in accordance with the guidelines for animal experimentation by the Institutional Animal Care and Use Committee, School of Medicine, University of South Carolina. Cells were maintained in growth medium (DMEM supplemented with 10% fetal bovine serum (FBS), penicillin (100 U/mL), streptomycin (100 μg/mL) and amphotericin B (250 ng/mL)) and passaged no more than four times after isolation. To induce osteogenesis, growth media was

replaced with osteogenic media consisting of DMEM supplemented with 10% FBS, penicillin (100 u/mL), streptomycin (100 μg/mL), amphotericin B (250 ng/mL), 10 mM sodium β-glycerolphosphate, L-ascorbic acid 2-phosphate (50 μg/mL) and 10^{-8} M dexamethasone. Media was replenished every 3-4 days.

4.4.6 Quantitative real-time RT-PCR analysis (RT-qPCR)

TCP, APTES glass wafer (silane), silane coated with TMV, TMV CP in Tris, and TMV CP in water were seeded with 4.0×10^4 cells per wafer and allowed to attach overnight in growth media. The media is replaced with osteogenic media and cultured for 14 days, except some TCP samples were kept in growth media to be a control for normalization. The cell cultures were terminated at this time point and total RNA was subsequently extracted using (RNeasy mini purification kit, Qiagen).

The quality and quantity of the extracted RNA was analyzed using Bio-Rad Experion (Bio-Rad Laboratories) and was reverse transcribed by using qScript™ cDNA Supermix (Quanta Biosciences). RT-qPCR (iQ5 real-time PCR detection system Bio-Rad Laboratories) was done by the method described as: 60 cycles of PCR (95°C for 20s, 58°C for 15 s, and 72°C for 15s), after initial denaturation step of 5 minutes at 95°C, by using 12.5 μL of iQ5 SYBR Green I Supermix, 2 pmol/μL of each forward and reverse primers and 0.5 μL cDNA templates in a final reaction volume of 25 μL. Glyceraldehyde 3-phosphate dehydrogenase (GAPDH) was used as the housekeeping gene. Data collection was enabled at 72°C in each cycle and C_T (threshold cycle) values were calculated using the iQ5 optical system software version 2.1. The expression levels of differentiated genes and undifferentiated genes were calculated using Pfaffl's method

(M.W. Pfaffl, G.W. Horgan and L. Dempfle, Relative expression software tool) for group-wise comparison and statistical analysis of relative expression results in real-time PCR, using GAPDH as the reference gene. The primers used for RT-qPCR are shown in Table 4.1. The primers were synthesized commercially (Integrated DNA Technologies, Inc.), and evaluated for an annealing temperature of 58°C.

Table 4.1 Primers used for RT-qPCR to measure gene expression levels. BGLAP: osteocalcin; IBSP: integrin-binding sialoprotein; SPP1: osteopontin.

Gene	Sequence (5'-3')
BGLAP	Forward: AAAGCCCAGCGACTCT
	Reverse: CTAAACGGTGGTGCCATAGAT
IBSP	Forward: TCTGAACGGGTTTCAGCAGACGA
	Reverse: GCCATGCCCCTTGTAGTAGCTGTA
GAPDH	Forward: ACTAAAGGGCATCCTGGGCTACACTGA
	Reverse: TGGGTGGTCCAGGGTTTCTTACTCCTT
SPP1	Forward: GACGGCCGAGGTGATAGCTT
	Reverse: CATGGCTGGTCTTCCCGTTGC

4.5 REFERENCES

[1] Ayres CE, Jha BS, Sell SA, Bowlin GL, Simpson DG. Nanotechnology in the design of soft tissue scaffolds: innovations in structure and function. Wiley Interdiscip Rev Nanomed Nanobiotechnol. 2010;2:20-34.

[2] Discher DE, Mooney DJ, Zandstra PW. Growth Factors, Matrices, and Forces Combine and Control Stem Cells. Science. 2009;324:1673-7.

[3] Dvir T, Timko BP, Kohane DS, Langer R. Nanotechnological strategies for engineering complex tissues. Nat Nanotechnol. 2011;6:13-22.

[4] Hynes RO. The extracellular matrix: not just pretty fibrils. Science. 2009;326:1216-9.

[5] Biggs MJP, Richards RG, McFarlane S, Wilkinson CDW, Oreffo ROC, Dalby MJ. Adhesion formation of primary human osteoblasts and the functional response of mesenchymal stem cells to 330-nm deep microgrooves. J R Soc Interface. 2008;5:1231-42.

[6] Biggs MJP, Richards RG, Gadegaard N, McMurray RJ, Affrossman S, Wilkinson CDW, et al. Interactions with nanoscale topography: Adhesion quantification and signal transduction in cells of osteogenic and multipotent lineage. J Biomed Mater Res Part A. 2009;91A:195-208.

[7] Lipski AM, Jaquiery C, Choi H, Eberli D, Stevens M, Martin I, et al. Nanoscale Engineering of Biomaterial Surfaces. Adv Mater. 2007;19:553-7.

[8] Lohmann CH, Sagun R, Sylvia VL, Cochran DL, Dean DD, Boyan BD, et al. Surface roughness modulates the response of MG63 osteoblast-like cells to 1,25-(OH)(2)D-3 through regulation of phospholipase A(2) activity and activation of protein kinase A. J Biomed Mater Res. 1999;47:139-51.

[9] Lovmand J, Justesen J, Foss M, Lauridsen RH, Lovmand M, Modin C, et al. The use of combinatorial topographical libraries for the screening of enhanced osteogenic expression and mineralization. Biomaterials. 2009;30:2015-22.

[10] Martin JY, Schwartz Z, Hummert TW, Schraub DM, Simpson J, Lankford J, et al. Effect of titanium surface roughness on proliferation, differentiation, and protein synthesis of human osteoblast-like cells (MG63). J Biomed Mater Res. 1995;29:389-401.

[11] McNamara LE, McMurray RJ, Biggs MJP, Kantawong F, Oreffo ROC, Dalby MJ. Nanotopographical control of stem cell differentiation. J Tissue Eng. 2010;1:1-13.

[12] Park J, Bauer S, Schlegel KA, Neukam FW, von der Mark K, Schmuki P. TiO_2 nanotube surfaces: 15 nm—an optimal length scale of surface topography for cell adhesion and differentiation. Small. 2009;5:666-71.

[13] Park J, Bauer S, von der Mark K, Schmuki P. Nanosize and vitality: TiO_2 nanotube diameter directs cell fate. Nano Lett. 2007;7:1686-91.

[14] Schwartz Z, Martin JY, Dean DD, Simpson J, Cochran DL, Boyan BD. Effect of titanium surface roughness on chondrocyte proliferation, matrix production, and differentiation depends on the state of cell maturation. J Biomed Mater Res. 1996;30:145-55.

[15] Jiang Y, Jahagirdar BN, Reinhardt RL, Schwartz RE, Keene CD, Ortiz-Gonzalez XR, et al. Pluripotency of mesenchymal stem cells derived from adult marrow. Nature. 2002;418:41-9.

[16] Minguell JJ, Erices A, Conget P. Mesenchymal stem cells. Exp Biol Med. 2001;226:507-20.

[17] Pittenger MF, Mackay AM, Beck SC, Jaiswal RK, Douglas R, Mosca JD, et al. Multilineage potential of adult human mesenchymal stem cells. Science. 1999;284:143-7.

[18] Si YL, Zhao YL, Hao HJ, Fu XB, Han WD. MSCs: Biological characteristics, clinical applications and their outstanding concerns. Ageing Res Rev. 2011;10:93-103.

[19] Mackay AM, Beck SC, Murphy JM, Barry FP, Chichester CO, Pittenger MF. Chondrogenic differentiation of cultured human mesenchymal stem cells from marrow. Tissue Eng. 1998;4:415-28.

[20] Drost AC, Weng S, Feil G, Schafer J, Baumann S, Kanz L, et al. In vitro myogenic differentiation of human bone marrow-derived mesenchymal stem cells as a potential treatment for urethral sphincter muscle repair. Ann N Y Acad Sci. 2009;1176:135-43.

[21] Oswald J, Boxberger S, Jorgensen B, Feldmann S, Ehninger G, Bornhauser M, et al. Mesenchymal stem cells can be differentiated into endothelial cells in vitro. Stem Cells. 2004;22:377-84.

[22] Gong Z, Calkins G, Cheng EC, Krause D, Niklason LE. Influence of culture medium on smooth muscle cell differentiation from human bone marrow-derived mesenchymal stem cells. Tissue Eng Part A. 2009;15:319-30.

[23] Porada CD, Almeida-Porada G. Mesenchymal stem cells as therapeutics and vehicles for gene and drug delivery. Adv Drug Deliv Rev. 2010;62:1156-66.

[24] Kaur G, Valarmathi MT, Potts JD, Jabbari E, Sabo-Attwood T, Wang Q. Regulation of osteogenic differentiation of rat bone marrow stromal cells on 2D nanorod substrates. Biomaterials. 2010;31:1732-41.

[25] Kaur G, Valarmathi MT, Potts JD, Wang Q. The promotion of osteoblastic differentiation of rat bone marrow stromal cells by a polyvalent plant mosaic virus. Biomaterials. 2008;29:4074-81.

[26] Kaur G, Wang C, Sun J, Wang Q. The synergistic effects of multivalent ligand display and nanotopography on osteogenic differentiation of rat bone marrow stem cells. Biomaterials. 2010;31:5813-24.

[27] Sitasuwan P, Andrew Lee L, Bo P, Davis EN, Lin Y, Wang Q. A plant virus substrate induces early upregulation of BMP2 for rapid bone formation. Integr Biol. 2012;4:651-60.

[28] Bruckman MA, Kaur G, Lee LA, Xie F, Sepulvecla J, Breitenkamp R, et al. Surface modification of tobacco mosaic virus with "Click" chemistry. ChemBioChem. 2008;9:519-23.

[29] Schlick KH, Udelhoven RA, Strohmeyer GC, Cloninger MJ. Binding of mannose-functionalized dendrimers with pea (Pisum sativum) lectin. Mol Pharm. 2005;2:295-301.

[30] Lee LA, Nguyen HG, Wang Q. Altering the landscape of viruses and bionanoparticles. Org Biomol Chem. 2011;9:6189-95.

[31] Jiang L, Li Q, Li M, Zhou Z, Wu L, Fan J, et al. A modified TMV-based vector facilitates the expression of longer foreign epitopes in tobacco. Vaccine. 2006;24:109-15.

[32] McCormick AA, Corbo TA, Wykoff-Clary S, Nguyen LV, Smith ML, Palmer KE, et al. TMV-peptide fusion vaccines induce cell-mediated immune responses and tumor protection in two murine models. Vaccine. 2006;24:6414-23.

[33] Niu Z, Bruckman MA, Li S, Lee LA, Lee B, Pingali SV, et al. Assembly of tobacco mosaic virus into fibrous and macroscopic bundled arrays mediated by surface aniline polymerization. Langmuir. 2007;23:6719-24.

[34] Pennazio S, Roggero P. The discovery of the chemical nature of tobacco mosaic virus. Riv Biol. 2000;93:253-81.

[35] Wang X, Niu Z, Li S, Wang Q, Li X. Nanomechanical characterization of polyaniline coated tobacco mosaic virus nanotubes. J Biomed Mater Res A. 2008;87:8-14.

[36] Young M, Willits D, Uchida M, Douglas T. Plant viruses as biotemplates for materials and their use in nanotechnology. Annu Rev Phytopathol. 2008;46:361-84.

[37] Lin Y, Balizan E, Lee LA, Niu Z, Wang Q. Self-assembly of rodlike bio-nanoparticles in capillary tubes. Angew Chem Int Ed Engl. 2010;49:868-72.

[38] Lin Y, Su Z, Xiao G, Balizan E, Kaur G, Niu Z, et al. Self-assembly of virus particles on flat surfaces via controlled evaporation. Langmuir. 2011;27:1398-402.

[39] Stubbs G, Warren S, Holmes K. Structure of RNA and RNA binding site in tobacco mosaic virus from 4-A map calculated from X-ray fibre diagrams. Nature. 1977;267:216-21.

[40] Bloomer AC, Champness JN, Bricogne G, Staden R, Klug A. Protein disk of tobacco mosaic virus at 2.8 A resolution showing the interactions within and between subunits. Nature. 1978;276:362-8.

[41] Gallagher WH, Lauffer MA. Calcium ion binding by isolated tobacco mosaic virus coat protein. J Mol Biol. 1983;170:921-9.

[42] Gallagher WH, Lauffer MA. Calcium ion binding by isolated tobacco mosaic virus coat protein. J Mol Biol. 1983;170:921-9.

[43] Shire SJ, McKay P, Leung DW, Cachianes GJ, Jackson E, Wood WI, et al. Preparation and properties of recombinant DNA derived tobacco mosaic virus coat protein. Biochemistry. 1990;29:5119-26.

[44] Klug A. The Tobacco Mosaic Virus Particle: Structure and Assembly. Philos Trans R Soc Lond B Biol Sci. 1999;354:531-5.

[45] Atabekov J, Nikitin N, Arkhipenko M, Chirkov S, Karpova O. Thermal transition of native tobacco mosaic virus and RNA-free viral proteins into spherical nanoparticles. J Gen Virol. 2011;92:453-6.

CHAPTER 5

OPTIMIZING TMV COATING ON POLYELECTROLYTE MULTILAYER FILMS

5.1 INTRODUCTION

5.1.1 Material-mediate differentiation of stem cells

Stem cells have the ability to self-renew and differentiate into various lineages, such as adipocytes, osteocytes, chondrocytes, hepatocytes, neurons, muscle cells, and epithelial cells [1-6]. The fate determination is depicted by the surrounding microenvironment, including both soluble and insoluble factors. The property of culture substrates *in vitro* is one of the insoluble factors that can affect cellular responses. There are several reports indicating that stem cell differentiation can be dictated at the nanometer level [7-16]. Recently, we have reported accelerated osteogenic differentiation for stem cells grown on plant virus coated substrates in comparison to cells cultured on conventional tissue culture plastic (TCP) [17, 18]. Two different plant viruses were employed in those studies, i.e. spherical *Turnip yellow mosaic virus* (TYMV) and rod-like *Tobacco mosaic virus* (TMV). However, the preparation of plant virus substrates was based on evaporation of solvent during drying at room temperature, which resulted in uncontrollable and inhomogeneous surface.

5.1.2 Layer-by-Layer deposition technique

In order to generate an even monolayer of plant viral nanoparticle in a controllable and reproducible manner for future cell culture experiments, electrostatically driven layer-by-

layer deposition (LbL) was employed. The LbL technique has attracted much interest due to its simplicity, flexibility, and robustness [19]. The LbL assembly mechanism is complicated, and depends on several factors such as solvent quality [20], temperature [21, 22], salt concentration [23], pH [24], and polyelectrolyte charge density [25]. Polyelectrolytes are a group of macromolecules with properties of both polymers and electrolytes. The LbL technique was first used to form polyelectrolyte multilayer films (PEMs) in the early 1990s [19, 26], based on the fact that polycations and polyanions can interact and form polyelectrolyte complexes [27]. In this chapter, we demonstrate the effects of salt concentration and pH on TMV adsorption. Under salt-free conditions, PEM thickness and mass rise linearity with the number of deposited layers N, whereas at high salt conditions PEM thickness and mass increase exponentially with N [28]. The pH adjustment of polymer solutions causes a change in the degree of polymer functional group ionization, depending on the pK_a of the polymer [24]. Since the deposition process is a surface charge dominated adsorption process, the pH adjustment of dipping solutions can change the thickness of PEM layers. Therefore, the addition of salt into polymer solutions and the pH adjustment to near the isoelectric point (pI) of the polymer solution should increase the amount of TMV adsorbed. The chemical structures of polymers used in this chapter are presented in Figure 5.1.

5.2 RESULTS AND DISCUSSION

5.2.1 TMV on PDDA with salt was more stable than TMV on (PDDA/PSS)$_{3.5}$

Firstly, we tested two strong polyelectrolytes, poly(dimethyldiallylammonium chloride) (PDDA) and poly(styrene sulfonate) (PSS) for PEM assembly. The first layer of

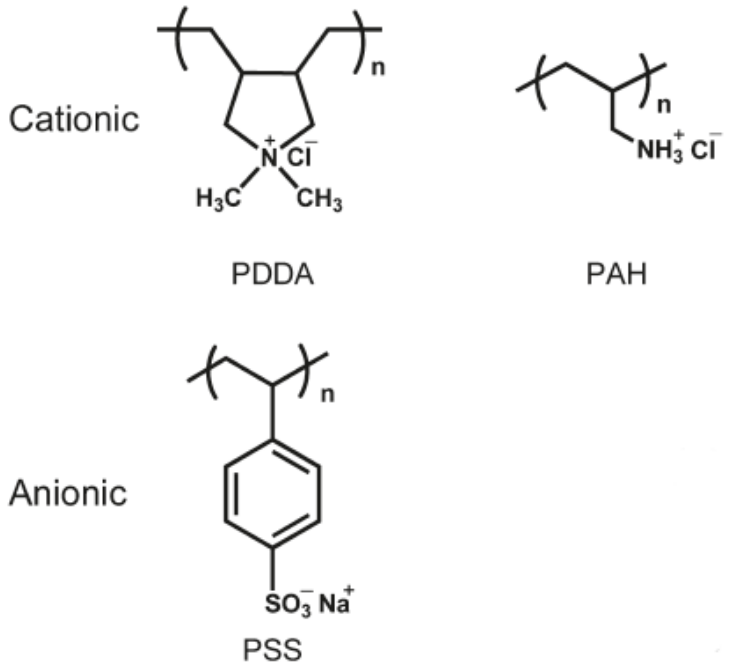

Figure 5.1Chemical structures of the cationic and anionic polyelectrolytes used in this study.

polycation coating is required to reverse the surface charge of the glass substrate from negatively charged to positively charged. One sample was only 1 layer of PDDA with 2 M NaCl and another was $(PDDA/PSS)_{3.5}$ without salt. Freshly prepared samples with TMV top layer on these two samples showed similar topography using AFM (Figure 5.2 a, d). TMV was adsorbed with full coverage on both PEM surfaces because PDDA is a strong polycation and TMV is negatively charged at neutral pH. However, after an incubation in PBS for 1 and 2 days at cell culture conditions to test the surface stability TMV on PDDA with NaCl remained (Figure 5.2 b, c) while TMV on $(PDDA/PSS)_{3.5}$ was mostly washed out from PEMs (Figure 5.2 e, f). The results indicated that the addition of salt to dipping solution increases the binding strength of TMV onto PEMs. The effect is very strong even with just one layer of PDDA.

Since PBS (approximately 150 mM) has much lower ionic strength compare to 2 M NaCl, PDDA solution was adjusted down to 100 mM NaCl in order to improve PEMs biocompatibility. Surface topography of TMV on PDDA with 100 mM NaCl was imaged by AFM (Figure 5.3 a) and it resembled that of PDDA with 2 M NaCl in Figure 5.2 a. This suggested that the concentration of salt did not affect TMV adsorption on PDDA. To confirm its stability, the surface was incubated in cell culture medium under cell culture conditions and imaged by AFM after 1 day. TMV was still visible on PDDA surface after medium incubation (Figure 5.3 b). However, this material showed poor biocompatibility (data not shown) which may be due to the strong polycation like PDDA.

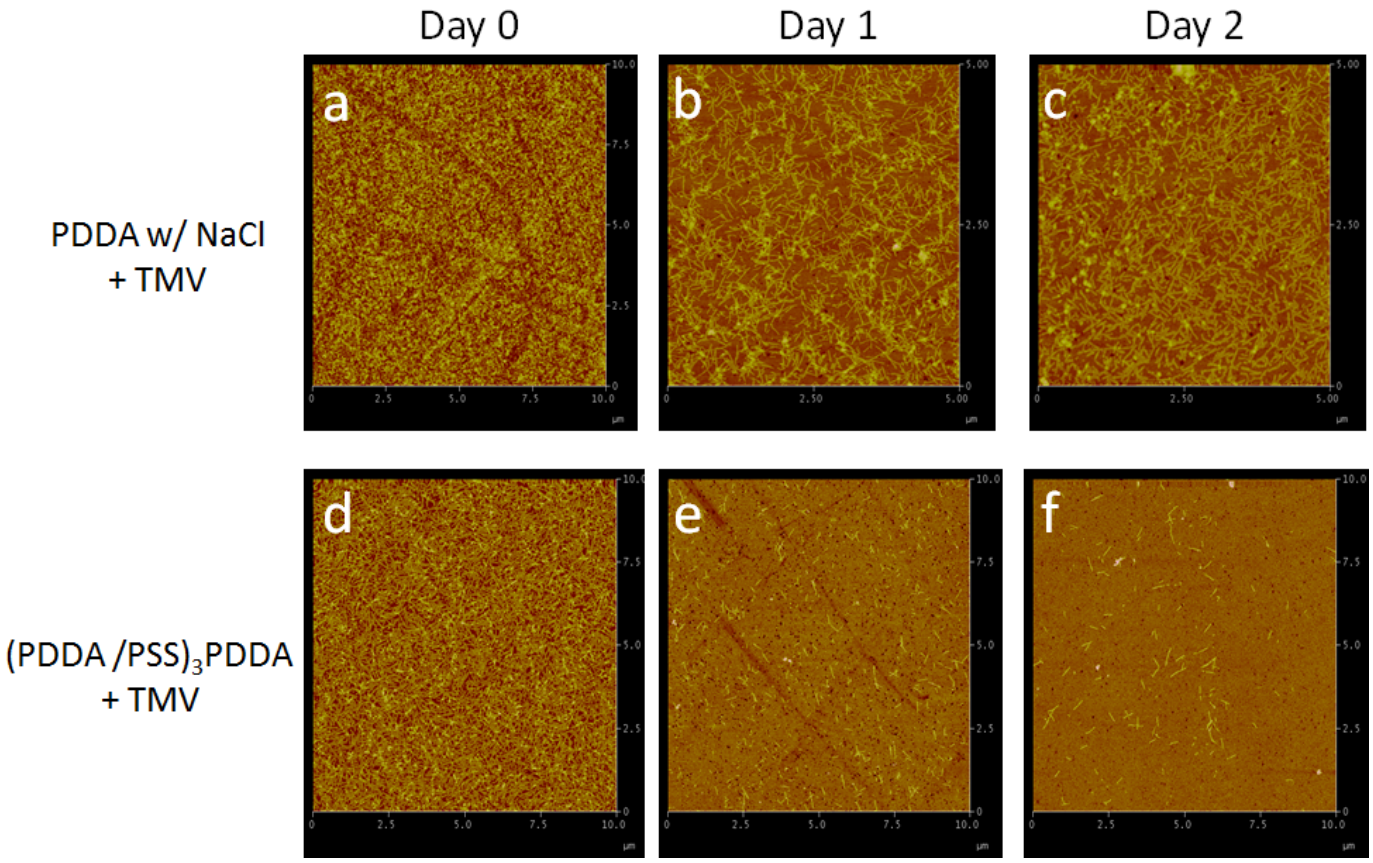

Figure 5.2 AFM images of PEMs assembled from PDDA and $(PDDA/PSS)_{3.5}$. PDDA assembled in the presence of 2 M NaCl and then TMV before (a) and 1 day (b) and 2 days (c) after PBS incubation. $(PDDA/PSS)_{3.5}$ without salt and then TMV before (d) and 1 day (e) and 2 days (f) after PBS incubation. The scan sizes are 10 µm × 10 µm for (a, d-f) and 3 µm × 3 µm for (b-c).

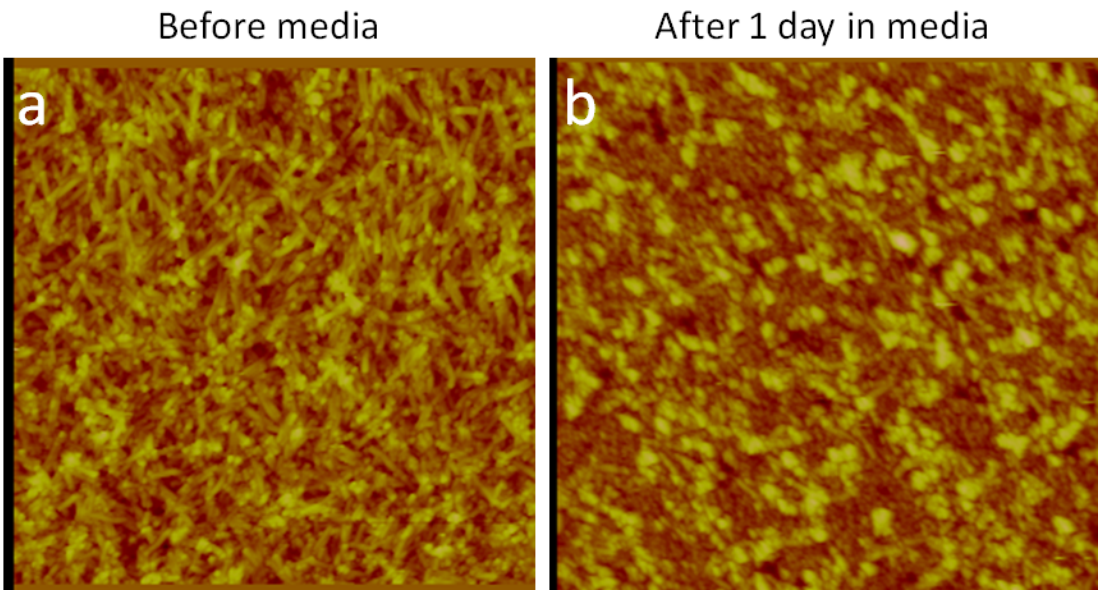

Figure 5.3 AFM images of TMV on PDDA with 100 mM NaCl before (a) and after (b) 1 day in cell culture medium. The scan size is 3 μm × 3 μm.

5.2.2 Coating of TMV on PAH at different pH values

A strong polycation PDDA was switched to poly(allylamine hydrochloride) (PAH) in order to improve biocompatibility for a future stem cell culture experiment. To further simplify the surface fabrication for cell culture, the direct coating of PAH on TCP was optimized by investigating the effect of PAH solution at different pH values ranging from 4.0 to 13.0 on TMV adsorption. From AFM images, TMV particles were visible on PAH on TCP, while TMV did not stick to TCP surface without PAH coating (Figure 5.4 a). The coverage of TMV on PAH at pH 11.0 and 13.0 was more than that at pH 4.0. To quantify the amount of TMV on PAH surface, the interior of TMV particles was modified with fluorescein and the fluorescent intensity was measured for each sample. The fluorescent intensity was the highest for PAH at pH 11.0 (Figure 5.4 b).

5.2.3 Varying ionic strength and pH of TMV solution

TMV adsorption is not only affected by the pH of PAH solution, but also ionic strength and pH of TMV solution itself. For this study, PAH was coated at a fixed pH of 5.0, which is the pH of PAH solution in water without any further pH adjustment. Five different conditions of TMV solutions varying in ionic strengths and pH values were tested. These included water, 10 mM Kphos buffer (pH 5.0 or 8.0), and 100 mM Kphos buffer (pH 5.0 or 8.0). AFM images revealed that there was little to no TMV particles adsorbed when the virus is in water, while there was a full coverage of TMV on PAH when the virus was in either 10 or 100 mM Kphos buffer at pH 5.0 (Figure 5.5 a). An increase in ionic strength and a decrease in pH of TMV solution enhanced TMV adsorption onto the PAH layer.

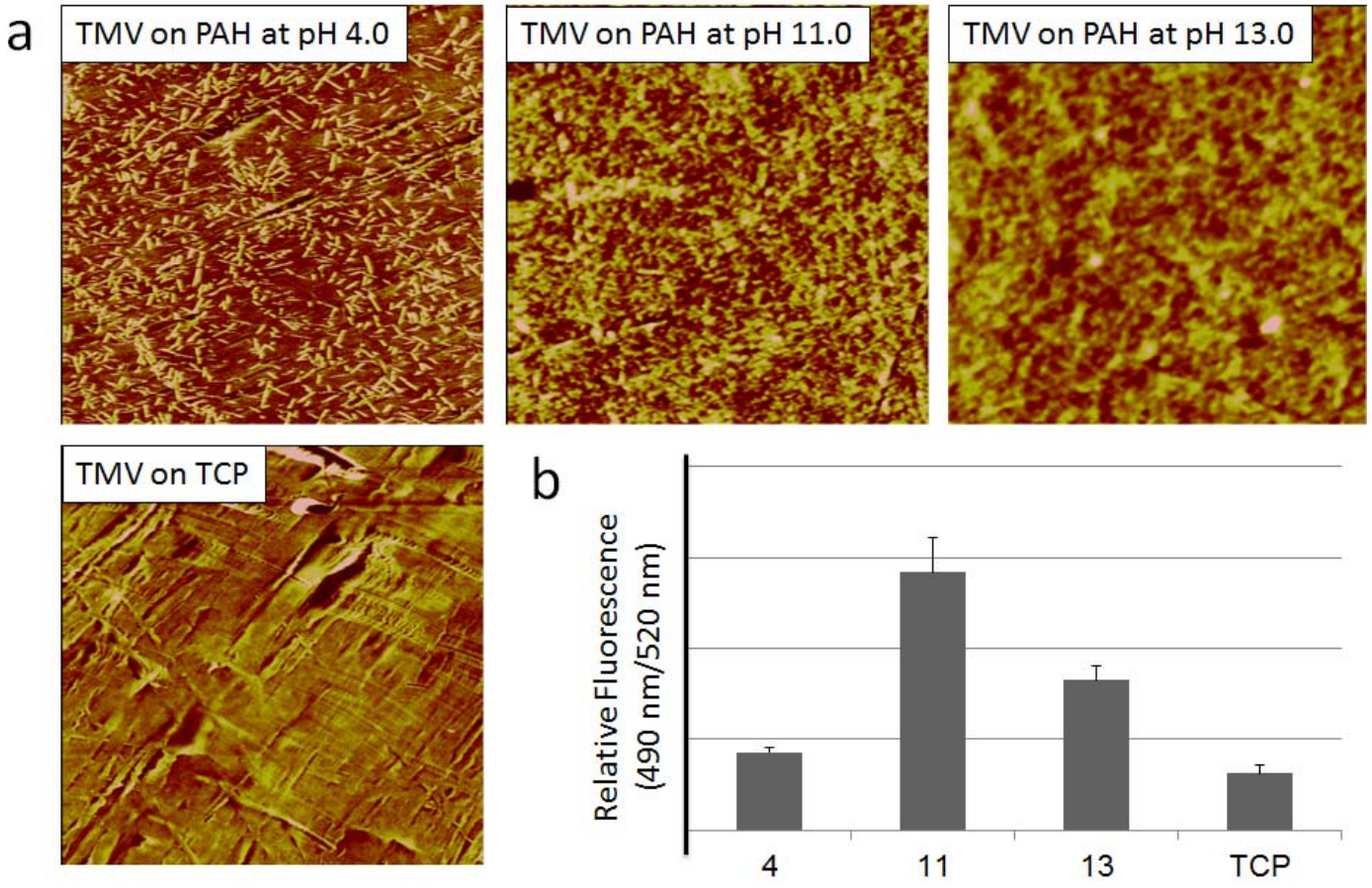

Figure 5.4 TMV coverage on PAH coated on TCP at different pH's. (a) AFM images of TMV on TCP or PAH at different pH's (4.0, 11.0, and 13.0). All scan size is 10 μm × 10 μm. (b) TMV particles were modified with fluorescein to the interior surface and coated on TCP or PAH at different pH's (4.0, 11.0, and 13.0).

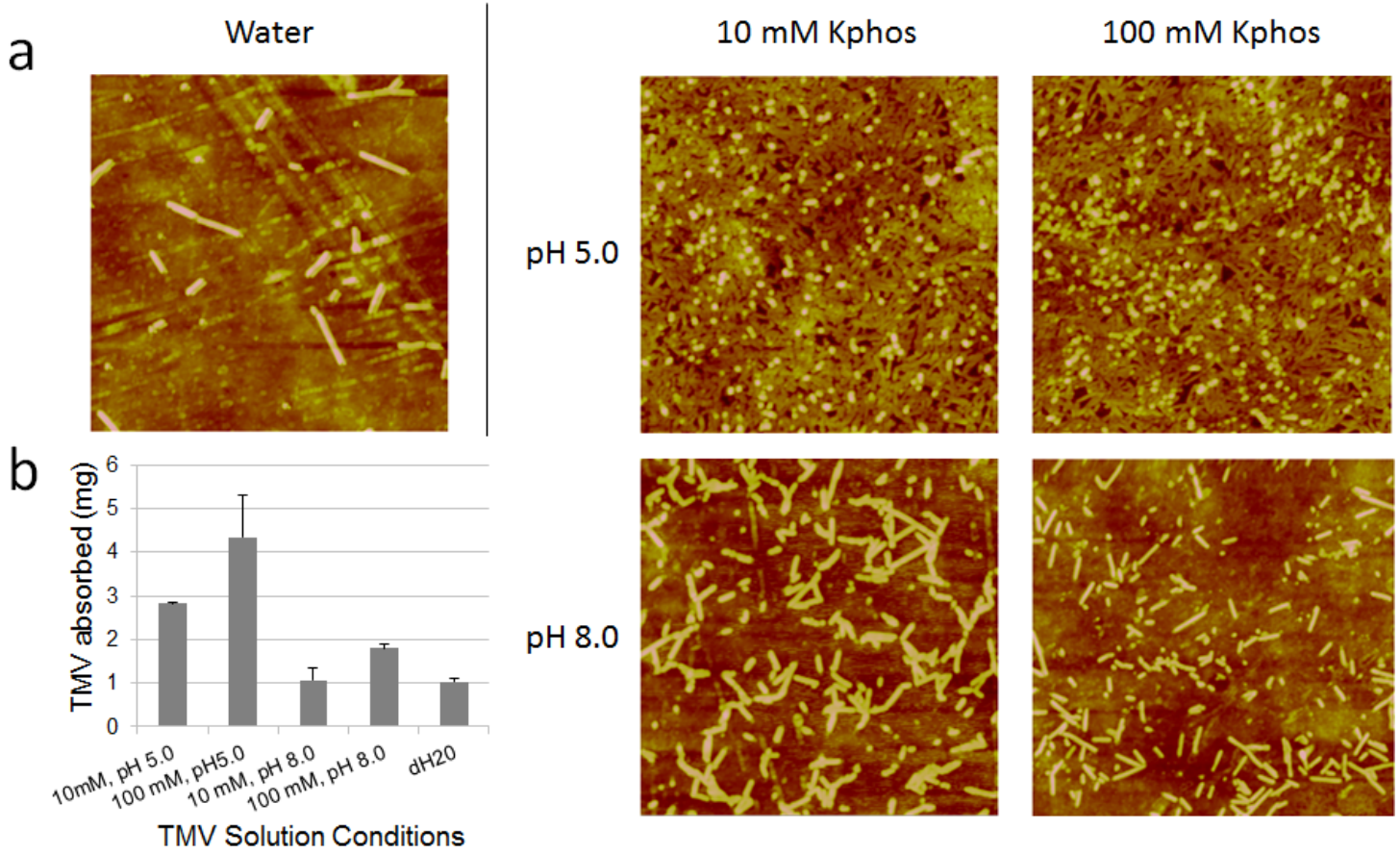

Figure 5.5 TMV coverage of different solvent for TMV on PAH at pH 5.0. (a) AFM images of TMV on PAH at pH 5.0 by using TMV suspended in water, 10 mM Kphos buffer (pH 5.0 or 8.0), or 100 mM Kphos buffer (pH 5.0 or 8.0). All scan size is 4 μm × 4 μm. (b) TMV particles were modified with fluorescein to the interior surface and coated on PAH at pH 5.0.

When comparing AFM images of samples prepared from TMV solution with different salt concentrations but the same pH value, there was no obvious difference in the amount of TMV adsorbed. To quantify the actual amount of TMV present on each surface, TMV particles modified with fluorescein were used and fluorescent intensity was recorded for each sample. Figure 5.5 b indicated that TMV in 100 mM Kphos buffer pH 5.0 was adsorbed the most on PAH made from PAH solution at pH 5.0. This is because the pH of TMV solution determined the charge density of the previously adsorbed PAH layer [24]. PAH is more protonated at pH 5.0 compared to pH 8.0, and therefore induced a stronger electrostatic force towards TMV particles, which are negatively charged. Thus, the simplest and optimal PAH/TMV coating conditions are to use PAH at pH 5.0 and TMV solution in 100 mM Kphos buffer pH 5.0. It is necessary to test the film stability and biocompatibility before future stem cell culture experiments. There is a possibility of exploring natural polyelectrolytes, such as poly-L-lysine, poly-D-lysine, chitosan and alginate, instead of synthetic polyelectrolytes mentioned in this chapter for better biocompatibility of TMV-based film.

5.3 CONCLUSION

In this work, PEMs were fabricated via LbL technique in order to generate a stable and homogenous monolayer of TMV substrate for future cell culture experiments. Although PDDA and PSS, strong polyelectrolytes, resulted in a high amount of TMV adsorbed, they exhibited a poor biocompatibility with stem cells *in vitro*. Nonetheless, it was demonstrated that the addition of salt to PDDA solution enhanced the PDDA/TMV film stability greatly. The PEM fabrication using PAH was explored in order to increase the

biocompatibility, and the PEM was generated directly on TCP surface to simplify a production of cell culture material. The pH increase of PAH solution to 11.0 showed to significantly increase TMV adsorption compared to that of lower pH values and uncoated TCP. Moreover, the salt concentration and pH of TMV solution could be adjusted to further improve the virus coating. The addition of salt into virus solution increased the amount of TMV adsorbed on PAH made at a fixed pH of 5.0. The lower pH value of 5.0 also showed higher adsorption of TMV than the higher pH value of 8.0. Although the optimal conditions for PAH/TMV film fabrication were suggested, the stability and biocompatibility of this film still need to be tested. The LbL technique has demonstrated to be a promising method to produce stable and highly reproducible viral particle-based biomaterials.

5.4 EXPERIMENTAL SECTION

5.4.1 TMV Isolation

TMV was isolated and purified according to a protocol previously reported [17, 29].

5.4.2 Preparation of PEMs coated with TMV

Round glass coverslips (18 mm, VWR) were cleaned by piranha solution (7:3 mixture of 98% H_2SO_4 and 30% H_2O_2) at 75 °C for 2 hours, followed by three washes with water (Millipore Synergy UV system, 18.2 MΩ.cm) and sonication. The glass coverslips were washed and dried with a stream of nitrogen gas.

PDDA (Mw ~ 100,000), PSS (Mw ~ 70,000), and PAH (Mw ~ 58,000) were purchased from Sigma-Aldrich. PDDA solution was prepared at 1 mg/mL with or

without NaCl at 100 mM or 2 M final concentration. PSS solution was prepared at 2 mg/mL in water. PAH solution was prepared at 1 mg/mL in water and pH was adjusted using HCl or NaOH. PEM films were prepared followed the previous report [30]. In brief, the glass coverslip was immersed into PDDA solution for 20 minutes, then alternatively immersed into PSS solution for 20 until 7 layers were obtained (with PDDA as the outmost layer). For PAH experiments, PAH solution was dropped into TCP well plate and incubate for 30 minutes and the wells were washed with water. The coated plates were dried more than 24 hours at room temperature. Then, the surface of coverslip and well plate was immersed in 1 mg/mL of TMV solution (100 mM Kphos buffer pH 7.4, unless stated) for 20 minutes and the substrate was thoroughly washed using water between each layer. The virus coverage on the coverslips was characterized using tapping-mode AFM images using a NanoScope IIIA MultiMode AFM (Veeco). Si tips with a resonance frequency of approximately 300 kHz, a spring constant of about 40 N m^{-1} and a scan rate of 0.5 Hz were used.

5.4.3 Quantification of TMV adsorption

An interior surface of TMV was modified with fluorescein amine by using EDC/HOBT coupling reported by Schlick *et al*. [31]. The fluorescently labeled virus particles were purified by ultracentrifugation at 45,000 rpm for 1.5 h (4 °C; Beckman 70.2 Ti). The pellet was resuspended in 100 mM Kphos buffer (pH 7.0) and used to determine surface coating density by measuring fluorescence on plate reader (ex/em 490/520 nm, Molecular Devices, SpectraMax M2e).

5.5 REFERENCES

[1] Pittenger MF, Mackay AM, Beck SC, Jaiswal RK, Douglas R, Mosca JD, et al. Multilineage potential of adult human mesenchymal stem cells. Science. 1999;284:143-7.

[2] Si YL, Zhao YL, Hao HJ, Fu XB, Han WD. MSCs: Biological characteristics, clinical applications and their outstanding concerns. Ageing Res Rev. 2011;10:93-103.

[3] Mackay AM, Beck SC, Murphy JM, Barry FP, Chichester CO, Pittenger MF. Chondrogenic differentiation of cultured human mesenchymal stem cells from marrow. Tissue Eng. 1998;4:415-28.

[4] Drost AC, Weng S, Feil G, Schafer J, Baumann S, Kanz L, et al. In vitro myogenic differentiation of human bone marrow-derived mesenchymal stem cells as a potential treatment for urethral sphincter muscle repair. Ann N Y Acad Sci. 2009;1176:135-43.

[5] Oswald J, Boxberger S, Jorgensen B, Feldmann S, Ehninger G, Bornhauser M, et al. Mesenchymal stem cells can be differentiated into endothelial cells in vitro. Stem Cells. 2004;22:377-84.

[6] Gong Z, Calkins G, Cheng EC, Krause D, Niklason LE. Influence of culture medium on smooth muscle cell differentiation from human bone marrow-derived mesenchymal stem cells. Tissue Eng Part A. 2009;15:319-30.

[7] Biggs MJP, Richards RG, McFarlane S, Wilkinson CDW, Oreffo ROC, Dalby MJ. Adhesion formation of primary human osteoblasts and the functional response of mesenchymal stem cells to 330-nm deep microgrooves. J R Soc Interface. 2008;5:1231-42.

[8] Biggs MJP, Richards RG, Gadegaard N, McMurray RJ, Affrossman S, Wilkinson CDW, et al. Interactions with nanoscale topography: Adhesion quantification and signal transduction in cells of osteogenic and multipotent lineage. J Biomed Mater Res Part A. 2009;91A:195-208.

[9] Lipski AM, Jaquiery C, Choi H, Eberli D, Stevens M, Martin I, et al. Nanoscale Engineering of Biomaterial Surfaces. Adv Mater. 2007;19:553-7.

[10] Lohmann CH, Sagun R, Sylvia VL, Cochran DL, Dean DD, Boyan BD, et al. Surface roughness modulates the response of MG63 osteoblast-like cells to 1,25-(OH)(2)D-3 through regulation of phospholipase A(2) activity and activation of protein kinase A. J Biomed Mater Res. 1999;47:139-51.

[11] Lovmand J, Justesen J, Foss M, Lauridsen RH, Lovmand M, Modin C, et al. The use of combinatorial topographical libraries for the screening of enhanced osteogenic expression and mineralization. Biomaterials. 2009;30:2015-22.

[12] Martin JY, Schwartz Z, Hummert TW, Schraub DM, Simpson J, Lankford J, et al. Effect of titanium surface roughness on proliferation, differentiation, and protein synthesis of human osteoblast-like cells (MG63). J Biomed Mater Res. 1995;29:389-401.

[13] McNamara LE, McMurray RJ, Biggs MJP, Kantawong F, Oreffo ROC, Dalby MJ. Nanotopographical control of stem cell differentiation. J Tissue Eng. 2010;1:1-13.

[14] Park J, Bauer S, Schlegel KA, Neukam FW, von der Mark K, Schmuki P. TiO_2 nanotube surfaces: 15 nm—an optimal length scale of surface topography for cell adhesion and differentiation. Small. 2009;5:666-71.

[15] Park J, Bauer S, von der Mark K, Schmuki P. Nanosize and vitality: TiO_2 nanotube diameter directs cell fate. Nano Letters. 2007;7:1686-91.

[16] Schwartz Z, Martin JY, Dean DD, Simpson J, Cochran DL, Boyan BD. Effect of titanium surface roughness on chondrocyte proliferation, matrix production, and differentiation depends on the state of cell maturation. J Biomed Mater Res. 1996;30:145-55.

[17] Kaur G, Valarmathi MT, Potts JD, Jabbari E, Sabo-Attwood T, Wang Q. Regulation of osteogenic differentiation of rat bone marrow stromal cells on 2D nanorod substrates. Biomaterials. 2010;31:1732-41.

[18] Kaur G, Valarmathi MT, Potts JD, Wang Q. The promotion of osteoblastic differentiation of rat bone marrow stromal cells by a polyvalent plant mosaic virus. Biomaterials. 2008;29:4074-81.

[19] Decher G. Fuzzy Nanoassemblies: Toward Layered Polymeric Multicomposites. Science. 1997;277:1232-7.

[20] Dubas ST, Schlenoff JB. Factors Controlling the Growth of Polyelectrolyte Multilayers. Macromolecules. 1999;32:8153-60.

[21] Tan HL, McMurdo MJ, Pan G, Van Patten PG. Temperature Dependence of Polyelectrolyte Multilayer Assembly. Langmuir. 2003;19:9311-4.

[22] Büscher K, Graf K, Ahrens H, Helm CA. Influence of Adsorption Conditions on the Structure of Polyelectrolyte Multilayers. Langmuir. 2002;18:3585-91.

[23] Clark SL, Montague MF, Hammond PT. Ionic Effects of Sodium Chloride on the Templated Deposition of Polyelectrolytes Using Layer-by-Layer Ionic Assembly. Macromolecules. 1997;30:7237-44.

[24] Yoo D, Shiratori SS, Rubner MF. Controlling Bilayer Composition and Surface Wettability of Sequentially Adsorbed Multilayers of Weak Polyelectrolytes. Macromolecules. 1998;31:4309-18.

[25] Glinel K, Moussa A, Jonas AM, Laschewsky A. Influence of Polyelectrolyte Charge Density on the Formation of Multilayers of Strong Polyelectrolytes at Low Ionic Strength. Langmuir. 2002;18:1408-12.

[26] Decher G, Hong JD, Schmitt J. Buildup of ultrathin multilayer films by a self-assembly process: III. Consecutively alternating adsorption of anionic and cationic polyelectrolytes on charged surfaces. Thin Solid Films. 1992;210–211, Part 2:831-5.

[27] Fuoss RM, Sadek H. Mutual Interaction of Polyelectrolytes. Science. 1949;110:552-4.

[28] Zan XJ, Peng B, Hoagland DA, Su ZH. Polyelectrolyte uptake by PEMs: Impact of salt concentration. Polymer Chemistry. 2011;2:2581-9.

[29] Kaur G, Wang C, Sun J, Wang Q. The synergistic effects of multivalent ligand display and nanotopography on osteogenic differentiation of rat bone marrow stem cells. Biomaterials. 2010;31:5813-24.

[30] Zan XJ, Su ZH. Incorporation of Nanoparticles into Polyelectrolyte Multilayers via Counterion Exchange and in situ Reduction. Langmuir. 2009;25:12355-60.

[31] Schlick TL, Ding Z, Kovacs EW, Francis MB. Dual-Surface Modification of the Tobacco Mosaic Virus. J Am Chem Soc. 2005;127:3718-23.

CHAPTER 6

POLYVALENT DISPLAY OF RGD MOTIFS ON TURNIP YELLOW MOSAIC VIRUS FOR ENHANCED STEM CELL ADHESION AND SPREADING[1]

6.1 INTRODUCTION

6.1.1 Plant virus-based scaffold for stem cell differentiation

Mesenchymal stem cells (MSCs) represent an important alternative source of cells for tissue regeneration due to their ability to differentiate into various phenotypes, such as chondrocytes [1, 2], skeletal muscle cells [3], osteoblasts [4, 5], and vascular muscle cells [6]. MSCs reside in specialized niches within various tissues and can be isolated, cultured and expanded *in vitro* [7]. The differentiation of MSCs into various phenotypes can be triggered by the micro-environment around the cells [8]. To better understand how MSCs respond to environmental cues, a number of nanomaterials and a variety of nanofabrication methods have been employed to control the differentiation pathways of MSC [9-14]. Our previous studies have shown that culturing bone marrow stem cells (BMSCs) on plant viruses, including *Tobacco mosaic virus* (TMV) and *Turnip yellow mosaic virus* (TYMV), can enhance cell differentiation [15-17]. Enhanced osteocalcin expression and levels of osteogenic differentiation were significantly augmented by the presence of virus coatings on 2D substrate in comparison to cells grown under standard conditions (from 21-28 days to 9-14 days), resulting in earlier mineralization of the cells. Furthermore, we found that the differentiation was preceded by an upregulated

[1] Zan X, Sitasuwan P, Powell J, Dreher TW, Wang Q. 2012. *Acta Biomater*. 8: 2978-85.
Reprinted here with permission of publisher (Appendix B).

expression of the bone morphogenetic protein 2 (BMP-2) gene, which encodes a key morphogenetic protein involved in bone formation, for cells cultured on native TMV within 8 h of osteo-induction [18]. However, plant virus-based substrates can often influence the differentiation of modest numbers of cells due to the lack of cell-binding motifs on the viral capsid.

6.1.2 RGD as an adhesive ligand

Numerous studies have shown that the enhancement of the endothelial and osteoblast adhesion can be achieved by immobilizing adhesive peptides on the substrate surface [19-21]. The tri-peptide motif RGD is often exploited for tissue regeneration applications due to its adhesion properties [21-26]. It has been reported that RGD-tailored bionanoparticles, produced either via genetic modification or chemical conjugation, can improve the cell-binding affinity dramatically [27-37]. For example, using a Cu(I) catalyzed azide-alkyne cycloaddition (CuAAC) reaction, synthetic RGD peptides have been conjugated to wild type TYMV, resulting in the promotion of adhesion, spreading, and proliferation of NIH-3T3 fibroblast cells [38]. We report here our work in replacing native coat protein (CP) residues within TYMV, through mutagenesis for display of RGD on the virus surface. Once assembled, this multivalent display of the desired RGD epitope enables the adhesion properties of BMSCs to be studied with predictive nanometer RGD-spacing.

6.1.3 TYMV as a scaffold building block

TYMV is a non-enveloped 28 nm plant virus composed of 180 copies of a 20 kDa CP that encapsidates a 6.3 kb monopartite genome. The subunits assemble together with T = 3 symmetry that results in an icosahedral capsid with prominent protrusions of pentameric and hexameric capsomeres on the viral surface (Figure 6.1 a) [39, 40]. TYMV is an attractive material for cell culturing studies as the virus can be propagated and purified through relatively simple means. In addition, the solved crystal structure of both the virion [40] and empty form of the particle [41] enables targeted mutagenesis of specific coat protein residues that reside either on the surface, interface or interior. A series of RGD mutants were created based on previous crystal structure analysis of surface exposed regions [40]. One of these mutants, TYMV-RGD44, in which residues 44-46 (TKD) were partially replaced to produce RGD (Figure 6.1 a), assembled and was infectious. Measurements of the 180 RGD motifs within the 28 nm particle predict intra-spacing of 2.1 nm (hexamers) and 2.3 nm (pentamers) between RGD motifs. The layer by layer (LBL) technique has previously been confirmed to be an effective way to incorporate viral particles into thin films with the integrity of the 3D viral structures well maintained [42-47]. We therefore use the LBL method to attach TYMV particles onto substrates in order to study the initial cell-substrate interaction of BMSCs.

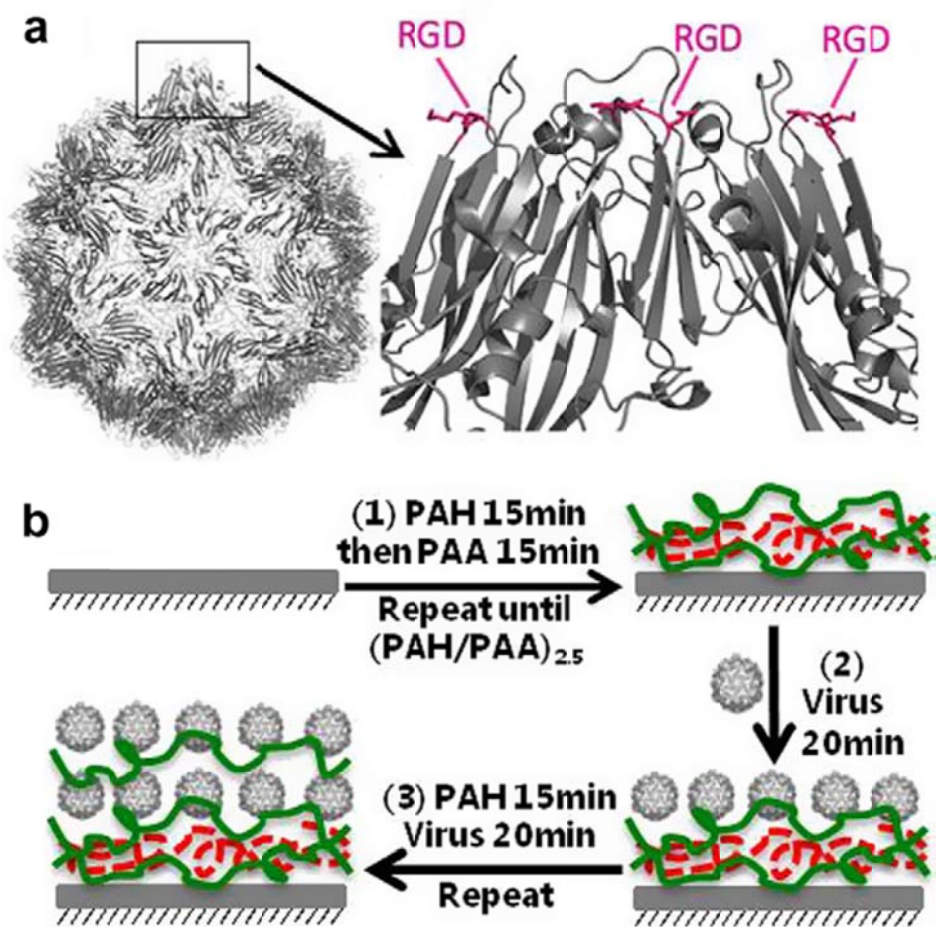

Figure 6.1 (a) Structure of TYMV with coat protein depiction based on elements of secondary structure (flattened arrows: β-sheet); highlighted region shows the location of RGD substitution (pink) within a given capsomere (one subunit has been removed for clarity in viewing RGD). Models were generated using PyMol (http://www.pymol.org) with coordinates obtained from RCSB Protein Data Bank (http://www.pdb.org). (b) Schematic illustrations of the stepwise growth of TYMV composite films using the LBL method. The green and red lines are PAH and PAA, respectively, and the gray sphere is virus particle (TYMV-wt or TYMV-RGD44).

6.2 RESULTS AND DISCUSSION

6.2.1 Generation of TYMV-RGD44

Various sites of the TYMV CP, including sites 44-46, 55-57, 61-63, 102-104, and 161-164 were tested for introducing RGD sequences. These sites were selected based on their surface availability deduced from the solved virion crystal structure [40]. TYMV-RGD44, with RGD placed at residues 44-46, was the only variant able to support infection and form stable virions. However, symptom development was slightly delayed and virus yield was decreased 10-fold relative to TYMV-wt. Attempts at generating infectious mutant virus with RGD at the other sites were unsuccessful, as virus was highly unstable and/or failed to move systemically within the plant (data not shown).

To determine whether TYMV-RGD44 retained the physical properties of TYMV-wt, virus preparations were analyzed by sucrose gradient ultracentrifugation (Figure 6.2a). The sedimentation rates of mutant and wild type viruses were similar, and empty particles (fractions 12-14) were present in each case [48]. Full RNA-containing virions migrated faster towards the bottom of the gradient. Both full and empty particles for TYMV-RGD44 and TYMV-wt were similar in diameter, with electron micrograph measurements in close agreement to the expected 28 nm (Figure 6.2a). CsCl gradients of virions showed TYMV-wt banding at a peak density of 1.413 g/mL, similar to published values (Figure 6.2b) [49]. TYMV-RGD44 migrated to a similar density (Figure 6.2b). The similar behavior of TYMV-RGD44 and TYMV-wt in these analyses suggests that the RGD insertion did not result in any global structural perturbation.

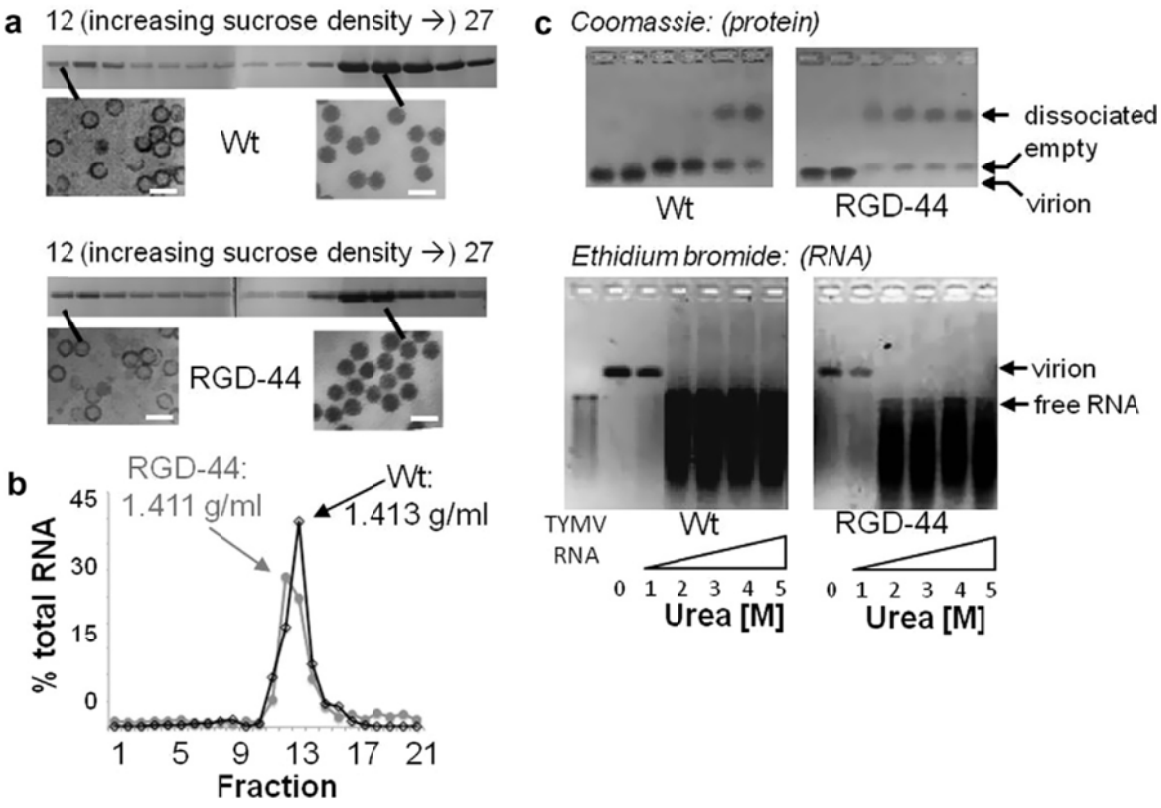

Figure 6.2 (a) TYMV-wt and TYMV-RGD44 were fractionated by 5–30% sucrose gradient ultracentrifugation, and fractions 12 to 27 were collected for analysis by SDS–PAGE with Coomassie Blue staining. Samples from fractions 12 and 24 were visualized by transmission electron microscopy (TEM), confirming the presence of 28 nm empty and full particles. Scale bars are 50 nm. (b) Cesium chloride gradient analysis of TYMV-wt and TYMV-RGD44 virions. Ten-drop fractions were collected and RNA isolated by phenol chloroform extraction. RNA shown as a percentage based on total RNA isolated from all 24 fractions. (c) 1% agarose gel electrophoresis to monitor the stability and electrophoretic mobility of virus stained for protein (top) or with ethidium bromide to monitor encapsidated versus released RNA (bottom), lane 1 (TYMV RNA) as a positive control.

The stability of virions, pooled from sucrose purified fractions 22-27, was also analyzed by agarose gel electrophoresis (Figure 6.2c) [50]. Two sets of gels, run in parallel were stained with either Coomassie to monitor protein (Figure 6.2c, top) or ethidium bromide to monitor encapsidated/released viral RNA (Figure 6.2c, bottom). Virus was pre-incubated in the denaturant urea for 30 min at 50 °C before electrophoresis. At 0 M (no urea) and 1 M treatments, TYMV-wt and TYMV-RGD44 virions ran as a single band and to similar positions. Based on the surface charge characteristics of both viruses the removal of the wild-type lysine at position 45 of the coat protein but the addition of an arginine at position 44 for TYMV-RGD44 resulted in a highly similar charge profile on the capsid surface and therefore similar electrophoretic migrations. At 2 M urea treatment, the protein band in the Coomassie gels was shifted slightly higher than at 1 M urea, a phenomenon previously attributed to TYMV being in an empty particle form but without encapsidated RNA [51]. The 2 M urea ethidium bromide gel was in good agreement with the Coomassie gel as the RNA, now ejected, ran in a similar manner as a TYMV RNA control (Figure 6.2c, first lane). For TYMV-RGD44 a second protein component began to appear at 2M urea, which for TYMV-wt did not appear until 4M urea treatment. While the nature of this second higher band has previously not been described, its appearance at higher urea conditions suggests some type of dissociated capsid state. These agarose gel findings imply that while the TYMV-RGD44 virus is stable in its purified state, it is less stable than its wild-type counterpart.

6.2.2 Fabrication of TYMV composite films using the LBL method

Since the isoelectric point (pI) of native TYMV-wt is approximately 3.7, the virus is negatively charged at neutral pH. Similar to previous reports on *Cowpea mosaic virus* (CPMV) [52, 53], the deposition of TYMV-wt can be readily achieved with the LBL method. To obtain a uniformly and stably positively charged surface, the substrate (quartz, silicon wafer, or QCM resonator) was coated with $(PAH/PAA)_{2.5}$, the virus deposition was triggered by immersing the $(PAH/PAA)_{2.5}$ in viral solution. The TYMV-wt adsorption behavior was studied firstly and the QCM data for TYMV-wt (0.1 mg/mL, pH 7.0) and PAH depositions are presented in Figure 6.3a. For each newly adsorbed TYMV-wt layer the average frequency shift is -186 ± 23 Hz. However, for each PAH layer, the frequency shift is 31 ± 4 Hz, suggesting that minor amounts of adsorbed TYMV-wt were peeled off during exposure to the PAH solution. The oscillatory increase of frequency shift with the number of layers indicates the continuous growth and successive deposition of TYMV-wt/PAH, which was also confirmed by UV-vis spectroscopy (Figure 6.3b). Because there was no adsorption of PAH in the UV-visible region, the absorbance of the multilayer films is primarily attributed to the deposition of TYMV, with the 260 nm peak reflecting the presence of RNA of the TYMV-wt particle [54]; this was used to monitor the amount of TYMV-wt in composite films (Figure 6.3b). A linear relationship between absorbance intensity and the number of bilayers was observed (Figure 6.3b, inset), indicating the linear growth of TYMV-wt deposition with the assembly cycles.

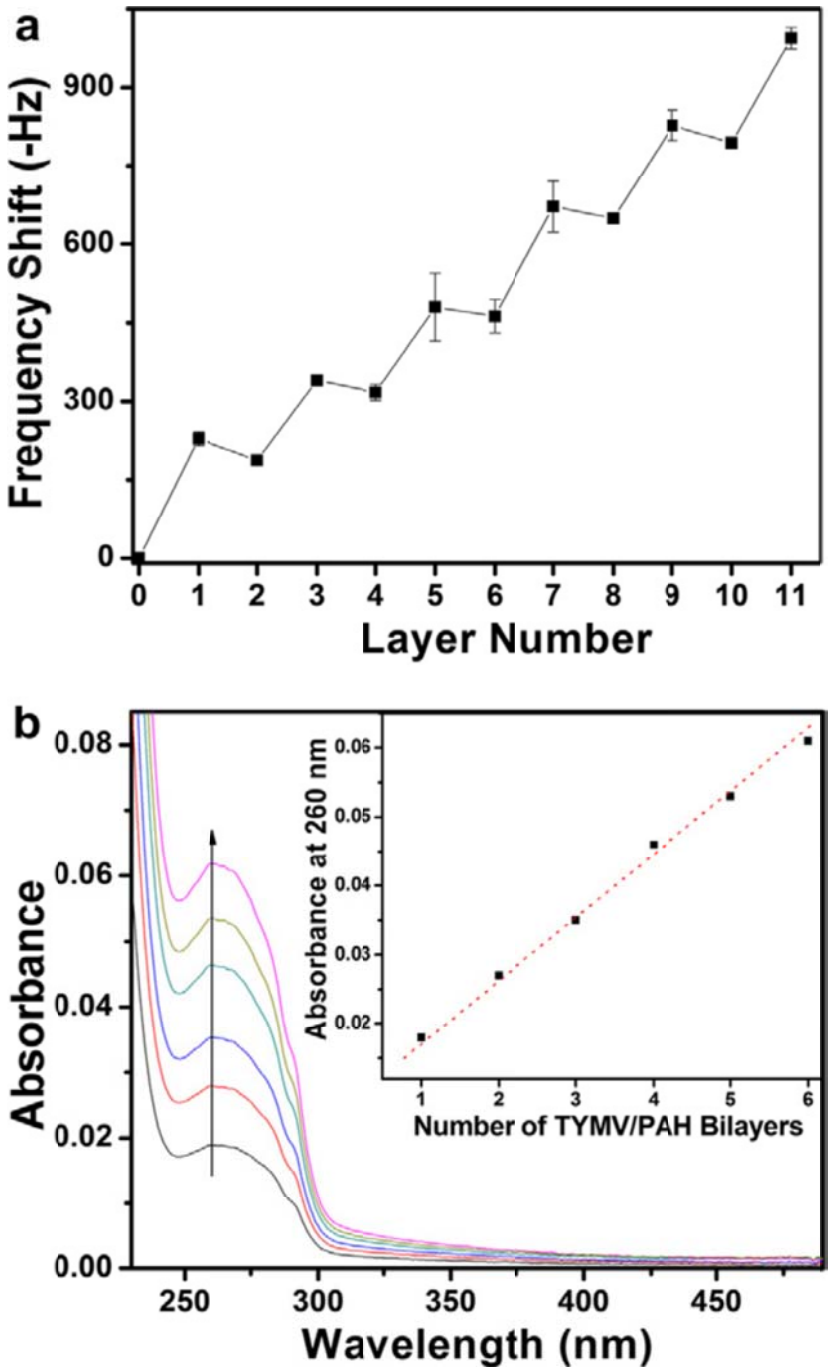

Figure 6.3 (a) QCM frequency shift for the alternating adsorption of TYMV-wt and PAH (pH 7.0) on silver QCM resonators after a $(PAH/PAA)_{2.5}$ coating. The odd layers are TYMV-wt and the even layers PAH. (b) UV–visible spectra of $(TYMV\text{-}wt/PAH)_n$ multilayers (n = 1–6). Inset plots the absorbance at 260 nm as a function of the number of bilayers.

As TYMV is a weak polyelectrolyte, it is expected that the pH value could greatly affect the adsorption process [52]. While fixing the pH of the PAH solution at 7.0, the deposition of TYMV-wt was studied by QCM using virus suspensions of different pH values from 3.2 to 7.0 (Fig. 6.4 a). Fig. 6.4 b shows the average frequency for each TYMV layer deposited at different pH. As predicted, the maximum TYMV deposition was achieved at pH 4.0 (near pI) [52, 55]. During the TYMV deposition, the interaction between TYMV-wt and substrate, as well as the interactions among TYMV-wt particles, govern the amount of deposited virus. For pH above the pI of TYMV-wt, the negative charge density of TYMV increases with pH, which favors the interaction between TYMV-wt and substrate. However, the increased charge also increases the electrostatic repulsion between virus particles, prohibiting higher surface coverage. Near the pI (pH 4.0), the electrostatic repulsion between TYMV-wt particles reaches a minimum, leading to maximum particle deposition. Based on the Sauerbrey equation [56], the mass of TYMV can be calculated. Assuming 1 g/cm^3 as the density of TYMV-wt and a monolayer adsorption with sphere-packing, we estimate the coverage of TYMV-wt under different pH, which were 151 ± 8% (pH 4.0), 115 ± 4% (pH 5.0), 52 ± 2% (pH 7.0) and 8 ± 0.3% (pH 3.2) respectively.

As no additional negatively-charged residues were introduced into the TYMV-RGD44 particle, two similar pH-dependent zeta potentials curves were observed for TYMV-wt and TYMV-RGD44 (Figure 6.4c), and the pIs of TYMV-wt and TYMV-RGD44 are 3.4 and 3.7 respectively. Since the LBL deposition is strongly dependent on the surface charge of virus particles, the LBL deposition of TYMV-RGD44 with PAH at pH 4.0 is very similar to that of TYMV-wt as shown in Figure 6.4d. Therefore, this

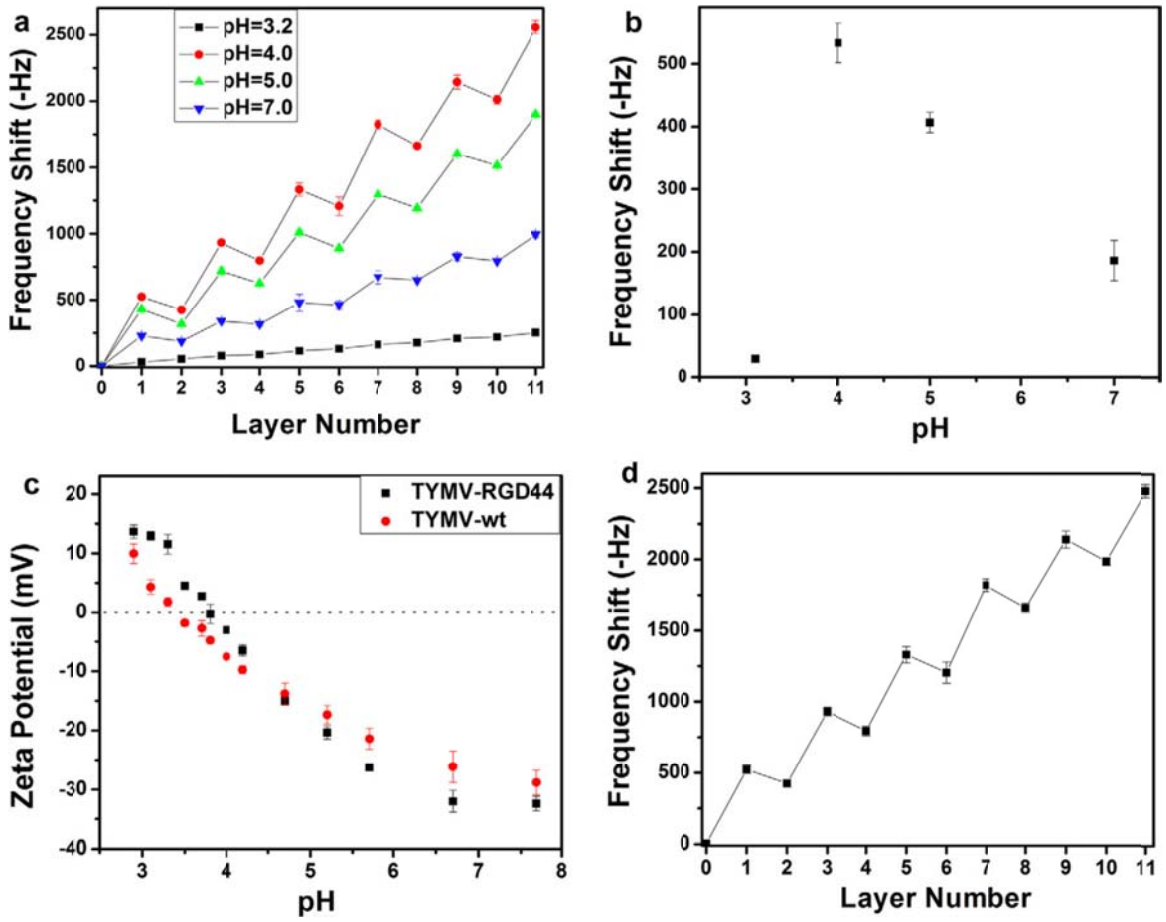

Figure 6.4 (a) QCM frequency shift for the alternating adsorption of TYMV-wt at different pH and PAH (pH 7.0) on silver QCM resonators. (b) Average frequency shift of QCM in one TYMV-wt layer at different pH of TYMV solution. (c) The dependence of zeta potential on the pH value. (d) QCM frequency shift for the alternating adsorption of TYMV-RGD44 (pH 4.0) and PAH (pH 7.0) on silver QCM resonators. The odd layers are TYMV and the even layers PAH for (a) and (c).

condition (C_{virus} = 0.1 mg/mL, pH 4.0, C_{PAH} = 1 mg/mL, pH 7.0) was used for preparing samples for cell culture studies.

Since the morphology of the film can greatly influence the cell behavior, the film topography was assessed by AFM (Figure 6.5). After the deposition of $(PAH/PAA)_{2.5}$ on silicon wafer, one layer of virus deposition at pH 7 only results in partial coverage (Fig. 5a). From the AFM image, the coverage is estimated to be ~ 46%, which agrees well with the above QCM data (i.e. 52 ± 2%). At pH 4.0, near the pI of TYMV-wt, with single virus deposition, the surface is fully covered with viral particles, and the surface coating is granular with the viral clusters formed on the order of hundreds of nanometers (Figure 6.5b). As additional layers of viral adsorption with polyelectrolyte progressed, more aggregations of TYMV can be observed (Figure 6.5c), with an increasing RMS to 7.4 nm. Compared with TYMV-RGD44 with the same layer number, the topology and its RMS are very similar to TYMV-wt (Figure 6.5d). The virus coated surface was stable even after being immersed in PBS buffer at 37 ºC for 48 h as shown by AFM analysis (Figure 6.5e). In addition, QCM test showed a frequency shift of 41 ± 4 Hz, indicating very little TYMV was desorbed. Therefore, both AFM and QCM data suggested that the majority of virus particles remain in the composite films, indicating that these composite films were stable enough for cell culturing studies.

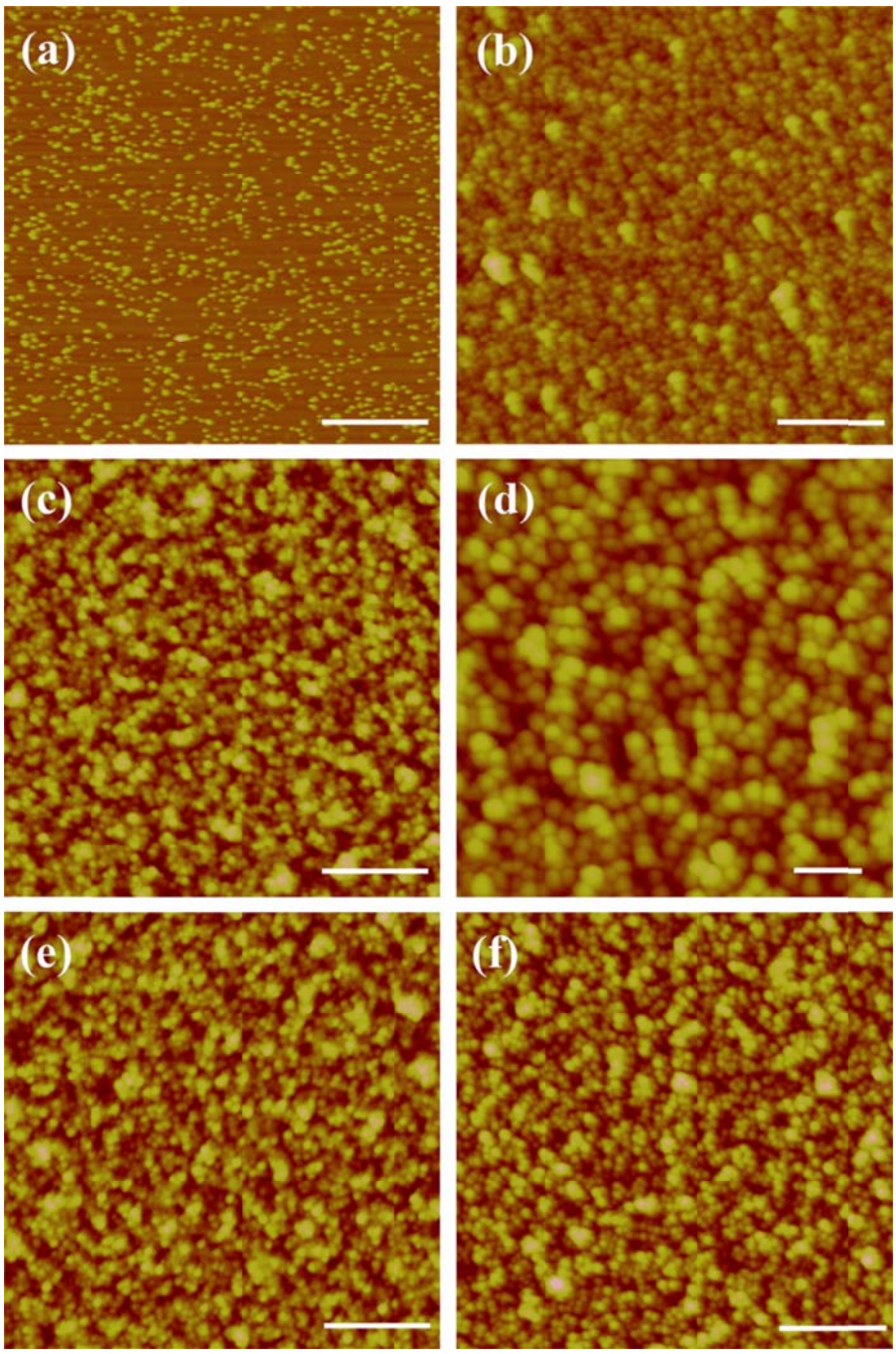

Figure 6.5 AFM images of different film surfaces: (a) $(PAH/TYMV\text{-}wt)_1$ prepared at pH 7.0, RMS = 2.5 nm; (b) $(PAH/TYMV\text{-}wt)_1$ prepared at pH 4.0, RMS = 4.2 nm; (c) $(PAH/TYMVwt)_3$ prepared at pH 4.0, RMS = 7.4 nm; (d) $(PAH/TYMV\text{-}wt)_3$ prepared at pH 4.0 at a higher magnification, scale bar = 100 nm; (e) $(PAH/TYMV\text{-}RGD)_3$ prepared at pH 4.0, RMS = 7.1 nm; and (f) $(PAH/TYMV\text{-}wt)_3$ prepared at pH 4.0 and immersed into PBS at 37 ºC for 48 h, RMS = 6.9 nm. The scale bars are 500 nm for (a–c) and (e–f).

6.2.3 BMSC adhesion and spreading

The effect of TYMV-RGD44 on the BMSC behavior was studied at 5 and 24 h after seeding. $(PAH/PAA)_{2.5}$ surface without virus layers has been reported to be biocompatible [57]. This surface was tested with BMSCs prior to our experiment. Although cells can attach and spread on $(PAH/PAA)_{2.5}$, fewer cells are observed on this LBL surface compared to a standard tissue culture plastic (data not shown). The incorporation of virus layers reduced BMSC attachment and spreading confirming a full coverage of virus on the material surface (data not shown). After 5 h incubation, a higher number of cells adhered on TYMV-RGD44 coated substrate compared to TYMV-wt under the same conditions (Figure 6.6a-d). Moreover, the cell spreading on TYMV-RGD44 films was also enhanced after 24 h culturing (Figure 6.6e-h). In order to quantify the effect of TYMV-RGD44 on cell adhesion, cell counts were determined, showing a much higher cell number with the TYMV-RGD44 coating (Figure 6.7a). This suggests that the RGD epitope on TYMV-RGD44 is functioning as a cell adhesion site. With the longer culturing time (24 h), the overall cell numbers increased, but the effect of TYMV-RGD44 on cell adhesion was less dramatic. These results indicate that the RGD has a greater effect at the earlier stages of cell adhesion, which agrees well with previous studies [19]. For both TYMV-wt and TYMV-RGD44 (Figure 6.7a) as the top layer, the increased viral layers could slightly increase the cell adhesion.

After initial adhesion observed at 5 h (Figure 6.6 a-d), the cells began to fully spread by 24 h (Figure 6.6 e-h). The TYMV-RGD44 coating can promote much better cell spreading over the surface than that of wild type (Figure 6.7b). In order to elucidate the influence of TYMV-RGD on cell spreading clearly, the average area per cell was

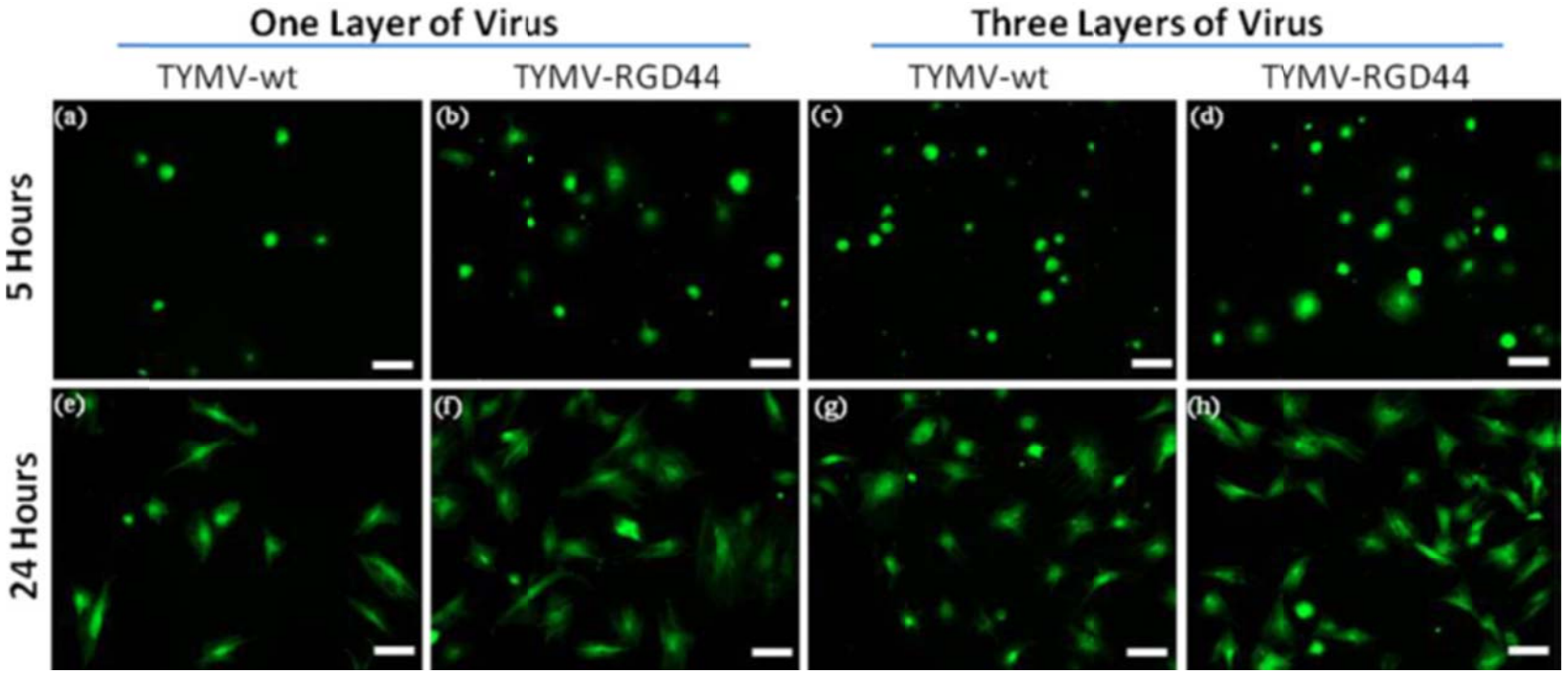

Figure 6.6 Fluorescent images of BMSC attachment and spreading (green) on different samples at 5 and 24 h after seeding. (a–d) Show initial cell adhesion after 5 h and (e–h) show cell spreading after 24 h. (a, e) one layer of TYMV-wt; (b, f) one layer of TYMV-RGD44; (c, g) three layers of TYMV-wt; (d, h) three layers of TYMV-RGD44. The scale bars are 100 μm.

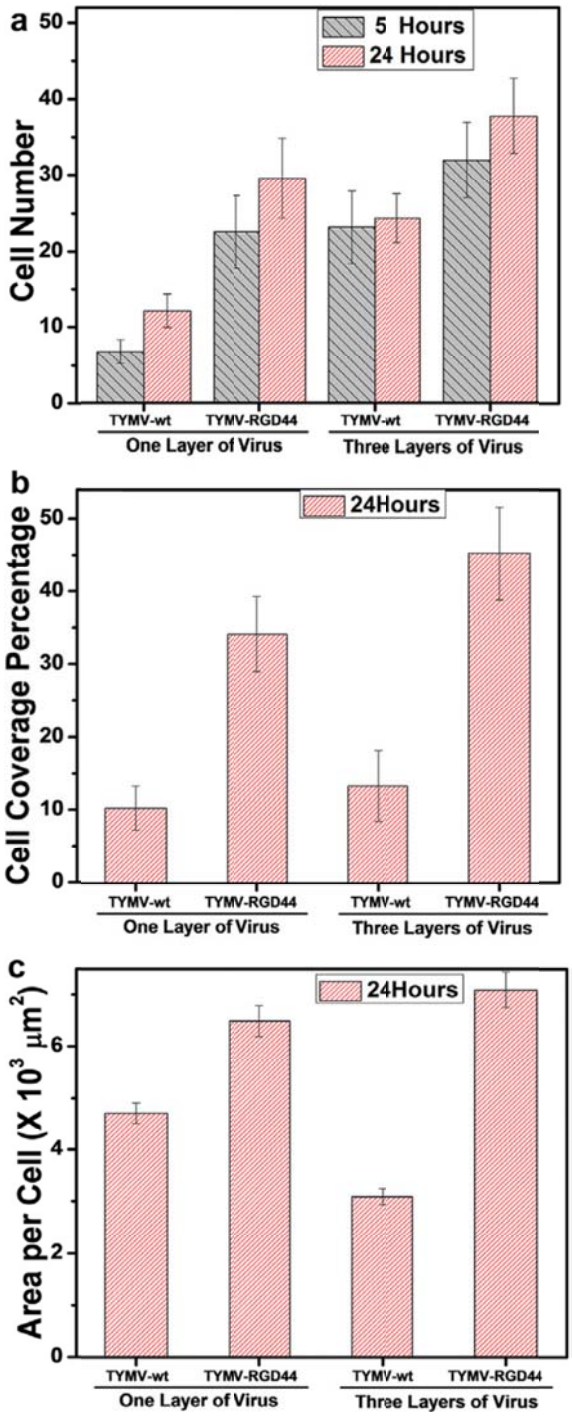

Figure 6.7 (a) BMSC attachment on TYMV-wt or TYMV-RGD44 coated substrates calculated from fluorescent images at 5 and 24 h after seeding. (b) Average percentage of cell coverage, showing the extent of BMSC spreading on different substrates at 24 h. (c) Average single cell area at 24 h, showing improved BMSC spreading on TYMV-RGD44 substrates when compared to TYMV-wt.

calculated by dividing the cell coverage area with the cell number, as shown in Figure 6.7c. With one viral layer, the area per cell on TYMV-wt coated surface is 4.7×10^3 μm^2 as compared to 6.5×10^3 μm^2 for TYMV-RGD44. The difference in cell spreading between TYMV-wt and TYMV-RGD44 coated surface becomes more obvious with three layers of viral coating.

6.3 CONCLUSION

It is believed that cell adhesion and spreading are mediated by the interaction between cell membrane receptors and protein domains present in the extracellular matrix (ECM). RGD as the most prominent cell adhesive peptide, its density and spatial distribution plays an important role in the spreading process. In our study, TYMV was genetically modified with an RGD substitution within the coat protein (CP) at residues 44-46 for display of RGD on the viral capsid surface. The estimated RGD spacing within a TYMV capsomere, based on the solved crystal structure, is approximately 19 angstroms (1.9 nm apart) [40]. Composite films composed of the wild type or mutant TYMV particles were fabricated by facile LBL deposition of virus particles and PAH. The coverage of virus can be readily controlled by adjusting the pH of the virus solution, with maximum deposition near the virus pI. Cell response studies showed that TYMV-RGD44 can enhance the adhesion of BMSCs at an early stage and promote cell spreading, which indicates that high RGD clustering within a confined area (viral capsid in our case) provides an ideal environment for cell adhesion and spreading. Clearly, the ability to engineer RGD with nanometer precision in a multivalent manner, optimize its deposition on composite thin films and test the resulting interactions with BMSC's provides a

framework for the testing of additional RGD-based viral scaffolds. The differentiation process of BMSCs on this genetically engineered biomaterial will be investigated further to discover its potential clinical applications in regenerative medicine.

6.4 EXPERIMENTAL SECTION

6.4.1 Materials

Poly(acrylic acid) (PAA), poly(allylamine hydrochloride) (PAH), sodium hydroxide (NaOH) and hydrogen chloride (HCl) were purchased from Sigma-Aldrich. Microscope cover glass slides (18 mm), quartz and silicon wafers were purchased from VWR. AT-cut quartz crystals were manufactured by Beijing Ziweixing Microelectronic Company. Deionized water (18.2 MΩ.cm) used for rinsing and preparing all the solutions was obtained from a Millipore Simplicity 185 purification unit.

6.4.2 Generation of TYMV-RGD44

To create TYMV-RGD44 mutant, the Stratagene Quickchange PCR mutagenesis approach was utilized with a TA-vector harboring the CP sequence (pGEM-TYMV-CP) as template. A unique *Sac*II restriction site was placed within the RGD coding sequence to enable convenient screening by restriction digestion. pGEM-TYMV-CP was digested with the restriction enzymes *Eco*RI and *Sma*I which enabled ligation of part of the CP coding region (residues 1-139) into a plasmid used for *Agrobacterium*-mediated infection, pCB302-TyW, through standard cloning techniques [58]. After plant infection, the identity of purified TYMV-RGD44 virus was verified by sequencing of RT-PCR product from a phenol-chloroform extracted genomic RNA template.

6.4.3 Isolation and virion properties of TYMV-wt and TYMV-RGD44

TYMV-wt and TYMV-RGD44 were purified via the Bentonite method [54]. Virus particles were further purified by centrifugation in 5-30% sucrose gradients (SW-41 rotor, 2 h and 45 min at 28,000 rpm) in 10 mM Na/KPO_4 1 mM $MgSO_4$ (pH 7.6) before use. To further characterize TYMV-wt and TYMV-RGD 44, CsCl gradient ultracentrifugation (in 30 mM sodium acetate, 1 mM $MgCl_2$ pH 6.0) was performed as previously described [49]. The electrophoretic mobility of virions was analyzed on Tris-acetate 1% agarose gels (pH 8.3) stained with either ethidium bromide for RNA or Coomassie R-250 for protein.

6.4.4 Substrate treatment

Quartz and silicon wafers were immersed in slightly boiled piranha solution (3:1 mixture of 98% H_2SO_4 and 30% H_2O_2) for 20 min followed by ultrasonication three times in pure water with extensive rinsing and drying with a stream of N_2. The resonator of the quartz crystal microbalance (QCM) was washed with ethanol and water, with drying in a stream of N_2.

6.4.5 LBL technique

The virus/polyelectrolyte films were fabricated as depicted in Fig. 1b. Firstly, polyelectrolyte multilayer films were deposited by sequential dipping of a substrate in PAH (1.0 mg/mL pH 7.0) and PAA (1.0 mg/mL pH 7.0) aqueous solutions for 15 min each, until it reaches $(PAH/PAA)_{2.5}$, where the value 2.5 indicates the number of bilayers. Next, the $(PAH/PAA)_{2.5}$ coated substrate was alternatively immersed in virus solution

(0.1 mg/mL) with different pH value for 20 min and PAH solution (1.0 mg/mL, pH 7.0) for 15 min. Water was used to rinse in between each deposition step until the desired number of layers was obtained.

6.4.6 BMSC isolation and expansion

Primary BMSCs were isolated from the bone marrow of young adult 80 g male Wistar rats (Harlan Sprague Dawley, Inc.). The procedures were performed in accordance with the guidelines for animal experimentation by the Institutional Animal Care and Use Committee, School of Medicine, University of South Carolina. In brief, cells were flushed from tibia and femur using a syringe needle. The cell suspension was then cultured on tissue culture plastic for 10 days to allow attachment, with consistent washing every three days. The attached cells were passaged and maintained in Dulbecco's Modified Eagle Medium (DMEM) growth medium supplemented with 10% fetal bovine serum (FBS), penicillin (100 μg/mL), streptomycin (100 μg/mL) and amphotericin B (250 ng/mL). Cells were passaged no more than four times after isolation before experimental use.

6.4.7 Cell adhesion and spreading

TYMV substrates were seeded with 4.0×10^4 cells per sample and cultured for either 5 or 24 h in growth medium. Before cell culture termination, each sample was stained with 4 μg/mL of Calcein AM (BD Biosciencse) in culture media for 30 min at 37˚C. The cells were washed with Hyclone Dulbecco's phosphate buffered saline (DPBS; Thermo Scientific) twice and fixed in 4% paraformaldehyde for 30 min at room temperature.

Images of the stained substrates were visualized on Olympus IX81 fluorescent microscopy. Cell coverage percent and cell number per image frame were calculated using Image J software. Ten images were taken from each sample and each substrate condition was repeated with three individual samples.

6.4.8 Characterization

A homemade QCM was used to detect the mass of the deposited layer using a 9 MHz quartz electrode coated with Ag on both sides. The QCM frequency shifts were monitored with a Protek C3100 universal frequency counter, and the mass of the deposited layer was calculated from the Sauerbrey equation [56]. Viral particles (empty and full) were visualized on glow-discharged Formvar-carbon coated copper grids (Ted Pella) by negative staining with 2% phosphotungstic acid in a Philips CM-12 transmission electron microscope at 80 kEV. The surface morphology was observed by atomic force microscopy using a NanoScope IIIA MultiMode AFM (Veeco) under the tapping mode. UV-vis spectra of the thin films deposited on quartz slides were collected on a Shimadzu UV-2450 spectrophotometer.

6.5 REFERENCES

[1] Mackay AM, Beck SC, Murphy JM, Barry FP, Chichester CO, Pittenger MF. Chondrogenic differentiation of cultured human mesenchymal stem cells from marrow. Tissue Engineering. 1998;4:415-28.

[2] Mackay AM, Beck SC, Pittenger MF. Human mesenchymal stem cells progress to hypertrophic chondrocytes under specific conditions in vitro. Mol Biol Cell. 1998;9:173-8.

[3] Ferrari G. Skeletal muscle regeneration by bone marrow-derived myogenic progenitors (vol 280, pg 1528, 1998). Science. 1998;281:923-7.

[4] Benayahu D, Kletter Y, Zipori D, Wientroub S. Bone-Marrow Derived Stromal Cell-Line Expressing Osteoblastic Phenotype Invitro and Osteogenic Capacity Invivo. J Cell Physiol. 1989;140:1-7.

[5] Calvert JW, Marra KG, Cook L, Kumta PN, DiMilla PA, Weiss LE. Characterization of osteoblast-like behavior of cultured bone marrow stromal cells on various polymer surfaces. J Biomed Mater Res. 2000;52:279-84.

[6] Nesti LJ, Jackson WM, Shanti RM, Koehler SM, Aragon AB, Bailey JR, et al. Differentiation Potential of Multipotent Progenitor Cells Derived from War-Traumatized Muscle Tissue. J Bone Joint Surg Am. 2008;90A:2390-8.

[7] Owen M, Friedenstein AJ. Stromal Stem-Cells - Marrow-Derived Osteogenic Precursors. Ciba Foundation Symposia. 1988;136:42-60.

[8] Fisher JP, Kim K, Yeatts A, Dean D. Stereolithographic Bone Scaffold Design Parameters: Osteogenic Differentiation and Signal Expression. Tissue Engineering Part B-Reviews. 2010;16:523-39.

[9] Orza A, Soritau O, Olenic L, Diudea M, Florea A, Ciuca DR, et al. Electrically Conductive Gold-Coated Collagen Nanofibers for Placental-Derived Mesenchymal Stem Cells Enhanced Differentiation and Proliferation. ACS Nano. 2011;5:4490-503.

[10] Nam JM, Namgung S, Kim T, Baik KY, Lee M, Hong S. Fibronectin-Carbon-Nanotube Hybrid Nanostructures for Controlled Cell Growth. Small. 2011;7:56-61.

[11] Hong S, Baik KY, Park SY, Heo K, Lee KB. Carbon Nanotube Monolayer Cues for Osteogenesis of Mesenchymal Stem Cells. Small. 2011;7:741-5.

[12] Lee KB, Solanki A, Shah S, Memoli KA, Park SY, Hong S. Controlling Differentiation of Neural Stem Cells Using Extracellular Matrix Protein Patterns. Small. 2010;6:2509-13.

[13] Jang MJ, Namgung S, Hong S, Nam Y. Directional neurite growth using carbon nanotube patterned substrates as a biomimetic cue. Nanotechnology. 2010;21:1-6.

[14] Park Y, Park SY, Park SY, Namgung S, Kim B, Im J, et al. Carbon nanotube monolayer patterns for directed growth of mesenchymal stem cells. Adv Mater. 2007;19:2530-3.

[15] Kaur G, Valarmathi MT, Potts JD, Jabbari E, Sabo-Attwood T, Wang Q. Regulation of osteogenic differentiation of rat bone marrow stromal cells on 2D nanorod substrates. Biomaterials. 2010;31:1732-41.

[16] Kaur G, Valarmathi MT, Potts JD, Wang Q. The promotion of osteoblastic differentiation of rat bone marrow stromal cells by a polyvalent plant mosaic virus. Biomaterials. 2008;29:4074-81.

[17] Kaur G, Wang C, Sun JA, Wang QA. The synergistic effects of multivalent ligand display and nanotopography on osteogenic differentiation of rat bone marrow stem cells. Biomaterials. 2010;31:5813-24.

[18] Sitasuwan P, Andrew Lee L, Bo P, Davis EN, Lin Y, Wang Q. A plant virus substrate induces early upregulation of BMP2 for rapid bone formation. Integr Biol. 2012;4:651-60.

[19] Qu ZW, Yan JL, Li BQ, Zhuang JP, Huang YM. Improving bone marrow stromal cell attachment on chitosan/hydroxyapatite scaffolds by an immobilized RGD peptide. Biomed Mater. 2010;5:065001-4.

[20] Massia SP, Hubbell JA. Human Endothelial-Cell Interactions with Surface-Coupled Adhesion Peptides on a Nonadhesive Glass Substrate and 2 Polymeric Biomaterials. J Biomed Mater Res. 1991;25:223-42.

[21] Chollet C, Chanseau C, Remy M, Guignandon A, Bareille R, Labrugere C, et al. The effect of RGD density on osteoblast and endothelial cell behavior on RGD-grafted polyethylene terephthalate surfaces. Biomaterials. 2009;30:711-20.

[22] Benoit DSW, Anseth KS. The effect on osteoblast function of colocalized RGD and PHSRN epitopes on PEG surfaces. Biomaterials. 2005;26:5209-20.

[23] Feng Y, Mrksich M. The Synergy Peptide PHSRN and the Adhesion Peptide RGD Mediate Cell Adhesion through a Common Mechanism†. Biochemistry. 2004;43:15811-21.

[24] Irvine DJ, Ruzette A-VG, Mayes AM, Griffith LG. Nanoscale Clustering of RGD Peptides at Surfaces Using Comb Polymers. 2. Surface Segregation of Comb Polymers in Polylactide. Biomacromolecules. 2001;2:545-56.

[25] Koo LY, Irvine DJ, Mayes AM, Lauffenburger DA, Griffith LG. Co-regulation of cell adhesion by nanoscale RGD organization and mechanical stimulus. J Cell Sci. 2002;115:1423-33.

[26] Massia SP, Hubbell JA. An Rgd Spacing of 440nm Is Sufficient for Integrin Alpha-V-Beta-3-Mediated Fibroblast Spreading and 140nm for Focal Contact and Stress Fiber Formation. J Cell Biol. 1991;114:1089-100.

[27] Sen Gupta S, Kuzelka J, Singh P, Lewis WG, Manchester M, Finn MG. Accelerated bioorthogonal conjugation: A practical method for the Ligation of diverse functional molecules to a polyvalent virus scaffold. Bioconjugate Chem. 2005;16:1572-9.

[28] Manchester M, Singh P. Virus-based nanoparticles (VNPs): Platform technologies for diagnostic imaging. Adv Drug Deliv Rev. 2006;58:1505-22.

[29] Lee LA, Niu ZW, Wang Q. Viruses and Virus-Like Protein Assemblies-Chemically Programmable Nanoscale Building Blocks. Nano Research. 2009;2:349-64.

[30] Flenniken ML, Willits DA, Harmsen AL, Liepold LO, Harmsen AG, Young MJ, et al. Melanoma and lymphocyte cell-specific targeting incorporated into a heat shock protein cage architecture. Chem Biol. 2006;13:161-70.

[31] Bruckman MA, Kaur G, Lee LA, Xie F, Sepulvecla J, Breitenkamp R, et al. Surface modification of tobacco mosaic virus with "Click" chemistry. ChemBioChem. 2008;9:519-23.

[32] Strable E, Johnson JE, Finn MG. Natural nanochemical building blocks: Icosahedral virus particles organized by attached oligonucleotides. Nano Lett. 2004;4:1385-9.

[33] Wu LY, Zang JF, Lee LA, Niu ZW, Horvatha GC, Braxtona V, et al. Electrospinning fabrication, structural and mechanical characterization of rod-like virus-based composite nanofibers. J Mater Chem. 2011;21:8550-7.

[34] Pokorski JK, Hovlid ML, Finn MG. Cell Targeting with Hybrid Q beta Virus-Like Particles Displaying Epidermal Growth Factor. ChemBioChem. 2011;12:2441-7.

[35] Kaltgrad E, O'Reilly MK, Liao L, Han S, Paulson JC, Finn MG. On-virus construction of polyvalent glycan ligands for cell-surface receptors. J Am Chem Soc. 2008;130:4578-9.

[36] Miermont A, Barnhill H, Strable E, Lu X, Wall KA, Wang Q, et al. Cowpea mosaic virus capsid: A promising carrier for the development of carbohydrate based antitumor Vaccines. Chemistry-a European Journal. 2008;14:4939-47.

[37] Destito G, Yeh R, Rae CS, Finn MG, Manchester M. Folic acid-mediated targeting of cowpea mosaic virus particles to tumor cells. Chem Biol. 2007;14:1152-62.

[38] Zeng QB, Saha S, Lee A, Barnhill H, Oxsher J, Dreher T, et al. Chemoselective modification of turnip yellow mosaic virus by Cu(I) catalyzed azide-alkyne 1,3-dipolar cycloaddition reaction and its application in cell binding. Bioconjugate Chem. 2011;22:58-66.

[39] Klug A, Finch JT, Franklin RE. Structure of Turnip Yellow Mosaic Virus. Nature. 1957;179:683-4.

[40] Canady MA, Larson SB, Day J, McPherson A. Crystal structure of turnip yellow mosaic virus. Nature Structural Biology. 1996;3:771-81.

[41] van Roon AMM, Bink HHJ, Plaisier JR, Pleij CWA, Abrahams JP, Pannu NS. Crystal structure of an empty capsid of turnip yellow mosaic virus. J Mol Biol. 2004;341:1205-14.

[42] Steinmetz NF, Findlay KC, Noel TR, Parker R, Lomonossoff GR, Evans DJ. Layer-by-layer assembly of viral nanoparticles and polyelectrolytes: The film architecture is different for spheres versus rods. ChemBioChem. 2008;9:1662-70.

[43] Rong J, Niu Z, Lee A, Wang Q. Self-assembly of viral particles. Curr Opin Colloid Interface Sci. 2011;16:441-50.

[44] Lvov Y, Haas H, Decher G, Mohwald H, Mikhailov A, Mtchedlishvily B, et al. Successive Deposition of Alternate Layers of Polyelectrolytes and a Charged Virus. Langmuir. 1994;10:4232-6.

[45] Suci PA, Klem MT, Arce FT, Douglas T, Young M. Assembly of multilayer films incorporating a viral protein cage architecture. Langmuir. 2006;22:8891-6.

[46] Yoo PJ, Nam KT, Qi JF, Lee SK, Park J, Belcher AM, et al. Spontaneous assembly of viruses on multilayered polymer surfaces. Nat Mater. 2006;5:234-40.

[47] Yoo PJ, Nam KT, Belchert AM, Hammond PT. Solvent-assisted patterning of polyelectrolyte multilayers and selective deposition of virus assemblies. Nano Lett. 2008;8:1081-9.

[48] Katouziansafadi M, Favre A, Haenni AL. Effect of Freezing and Thawing on the Structure of Turnip Yellow Mosaic-Virus. Eur J Biochem. 1980;112:479-86.

[49] Noort A, Vandendries CLAM, Pleij CWA, Jaspars EMJ, Bosch L. Properties of Turnip Yellow Mosaic-Virus in Cesium-Chloride Solutions - the Formation of High-Density Components. Virology. 1982;120:412-21.

[50] Ball EM. A Technique for Comparing Electrophoretic Mobility Rates of Viruses or Virus Strains. Arch Biochem Biophys. 1966;114:547-56.

[51] Powell JD, Barbar E, Dreher TW. Turnip yellow mosaic virus forms infectious particles without the native beta-annulus structure and flexible coat protein N-terminus. Virology. 2011;422:165-73.

[52] Su Z, Lin Y, Niu Z, Li S, Kaur G, Lee LA, et al. Layer-by-layer assembly of viral capsid for cell adhesion. Acta Biomater. 2008;4:838-43.

[53] Fukuto M, Kewalramani S, Wang ST, Lin YA, Huong GN, Wang QA, et al. Systematic approach to electrostatically induced 2D crystallization of nanoparticles at liquid interfaces. Soft Matter. 2011;7:939-45.

[54] Dunn DB, Hitchbor.Jh. Use of Bentonite in Purification of Plant Viruses. Virology. 1965;25:171-92.

[55] Su ZH, Lin Y, Chen XS, Jing XB, Jiang YS. Gelatin multilayers assembled on poly(L-lactic acid) surface for better cytocompatibility. J Appl Polym Sci. 2008;109:530-6.

[56] Akashi M, Serizawa T, Yamamoto K. A novel fabrication of ultrathin poly(vinylamine) films with a molecularly smooth surface. Langmuir. 1999;15:4682-4.

[57] Seo J, Lee H, Jeon J, Jang Y, Kim R, Char K, et al. Tunable Layer-by-Layer Polyelectrolyte Platforms for Comparative Cell Assays. Biomacromolecules. 2009;10:2254-60.

[58] Cho TJ, Dreher TW. Encapsidation of genomic but not subgenomic Turnip yellow mosaic virus RNA by coat protein provided in trans. Virology. 2006;356:126-35.

CHAPTER 7

ROUGHNESS CONTROLLED OSTEOGENESIS OF MESENCHYMAL STEM CELLS ON BIOMIMETIC CAP-COLLAGEN COATING

7.1 INTRODUCTION

7.1.1 Material-mediated osteogenesis

Mesenchymal stem cells (MSCs) are multipotent adult progenitors that can be found within adult connective tissues, isolated in large quality, and expended *in vitro* with the capability to differentiate into various phenotypes [1]. By adding the inductive factors into cell culture medium, a great deal of distinct phenotypes, such as chondrocytes [2], skeletal muscle cells [3], osteoblasts [4, 5] and vascular muscle cells [6], have been derived from the MSCs. Traditionally, MSCs could be induced to undergo osteogenesis *in vitro* by supplementing culture medium with dexamethasone, ascorbic acid, and β-glycerophosphate [7]. In recent years, there have been many attempts to direct MSCs into osteogenic lineage by material chemical and physical properties [8], including surface chemistry [9], surface energy [10], stiffness [11, 12], topology [13, 14], and roughness [15-18]. These findings opened a novel and imaginative door to tissue engineering, i.e. directing stem cell differentiation to generate healthy tissue and replace diseased tissue by controlling either physical or chemical properties of the implanted materials. In bone tissue engineering, the osteo-inductivity of implanted material is critical for the success of local bone generation.

7.1.2 Calcium phosphate as osteo-conductive substrate

Calcium phosphate (CaP) is the primary inorganic component of bone matrix, which is consisting of the calcium phosphate (CaP)-collagen fillers with several level hierarchical structure orders [19]. The outstanding osteo-conductive property exhibited by CaP, makes the CaP a promising candidate as bone substitute and supplemental material for bone regeneration [20]. In fact, CaP coatings have shown exceptional effects not only on improving osteoblast proliferation [21, 22] and ameliorating the osteo-integration *in vitro* [23], but also reducing bone loss [24] and enhancing bone formation [25] *in vivo*. However, the mismatch of mechanical properties and poor interaction with surrounding tissue in long term observation of these material lead to the destruction of the implant. Coating the CaP on mechanically strong implant materials, such as metal or polymer scaffolds [20, 26, 27], was an effective way to resolve the mechanical brittleness problem without losing its biological efficacy. Recently, inspired by the component of natural bone composing of CaP (~70%) and collagen (~30%), the bio-mimetic surface coating was proposed and developed as third generation biomaterials by doping various proteins into the CaP [28, 29].

7.1.3 Generation of CaP coating by layer-by-layer deposition

Based on the bone structure, it is assumed that optimal osteo-conductive coating should have several characters: a rough surface, branched network of canals and pores, and high strength with elasticity modulus close to that of the bone [30, 31]. The osteo-conductivity of CaP coating can be affected by many factors, such as particle size of CaP, the crystallinity of CaP, the surface pattern and surface energy [32-35]. It is believed that a

higher surface energy, higher crystallinity and smaller size of CaP particles would result in a better osteo-conductive coating. The surface roughness, a dominant factor on cell-substrate and cell-cell interactions, has been demonstrated to direct the adhesion, proliferation, differentiation and final fate of various cells [16, 36-38]. However, very few of reports have unveiled the roughness effect on osteo-conductivity of CaP coating, and how the roughness contributes to the osteo-conductivity is unanswered [39-41]. To address this issue, we need a coating technique which has mild fabrication conditions, homogenously controllable physical properties and long term stability. The layer-by-layer (LBL) technique based on the electrostatic interaction is an ideal method to this end. The generation of uniform polyelectrolyte multilayer films (PEMs) on various substrates, including polymers and metals, is independent of the geometry and the size of substrates by a LBL approach [42-44]. In addition, some PEMs show good stability and biocompatibility under physiological conditions. These features of the PEMs produced by the LBL technique make it suitable for the biomedicine and tissue engineering applications [45, 46]. Moreover, the deposited polyelectrolyte can provide the nucleation sites for *in situ* growing CaP coating [47, 48], where the crystallinity and morphology of coating surface could be readily controlled by regulating the nucleation conditions.

To better improve the CaP based surface coating, we report the fabrication of collagen doped CaP coatings by bio-mimetic *in situ* growing method on PEMs with a controllable surface roughness. In addition, the osteo-conductive effect of PEM/CaP-Col surface roughness on MSCs was studied, which could be potentially used to optimize the design of materials for tissue engineering applications.

7.2 RESULTS AND DISCUSSION

7.2.1 Surface feature and chemical composition of PEMs/CaP-Col surface

The fabrication process of PEMs/CaP-Col surface was demonstrated in Figure 7.1. Poly(allylamine hydrochloride) (PAH) and poly(styrene sulfonate) (PSS) were alternatively deposited onto the silicon or glass substrates until 5 layers of PEMs were formed. Next, the substrates were horizontally incubated in the freshly prepared bio-mimetic solutions at room temperature. Upon immersing PEMs into the bio-mimetic solution, PEM surface acts as a nucleation site for CaP crystal growth [47, 48] while collagen was doped into the CaP (the surface is denoted as CaP-Col) [45, 46]. The surface roughness of CaP-Col coating increases with an increase in the incubation time. After certain incubation times, the samples were washed and dried. The following characterizations of these samples were performed on the underside of the samples to avoid the deposition of CaP precipitate from the supersaturated solution.

Both the chemical and physical properties of the surface, including the crystallinity of CaP, homogeneity and compositions of the surface, are critical to cell adhesion, proliferation and differentiation. Therefore, the surface properties were characterized in detail. Figure 7.2 showed the SEM images of PEMs/CaP-Col coating morphologies *in situ* grown from bio-mimetic solution at different incubation time points. At time scale 0 min, the surface was very smooth (Figure 7.2 a). After 1h incubation, the plate like crystal was observed with uniform distribution in the whole substrate (Figure 7.2b). Upon higher magnification, it was shown that nano-sized crystals randomly connected with each other from the growing edge (inset of Figure 7.2 b), and micro-sized pores between the crystal edges could be observed. With further incubation, the above

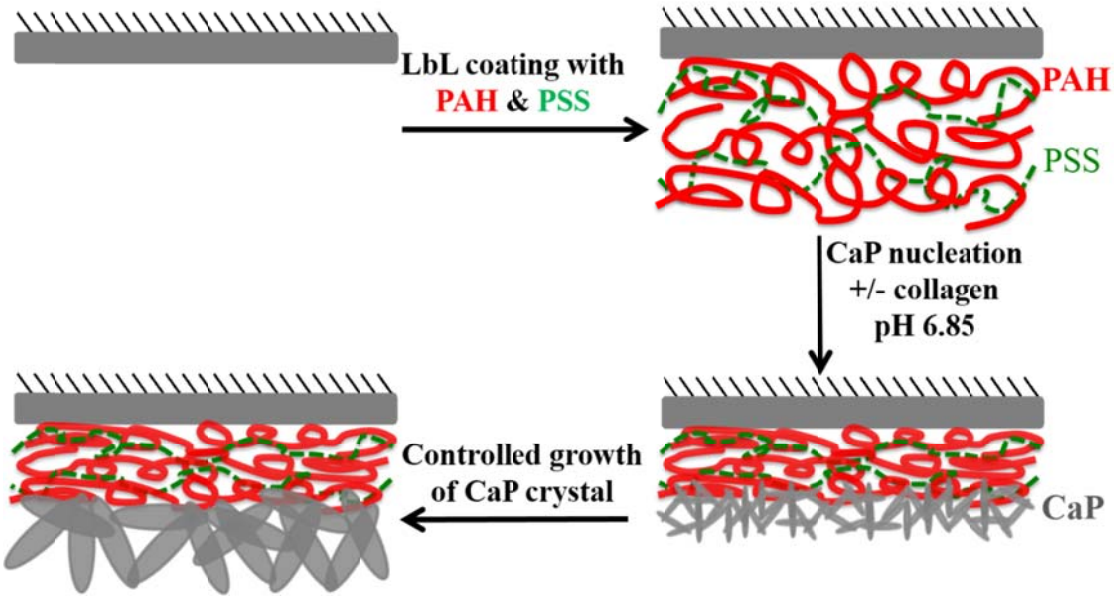

Figure 7.1 Schematic demonstration of fabricating PEMs/CaP-Col surface.

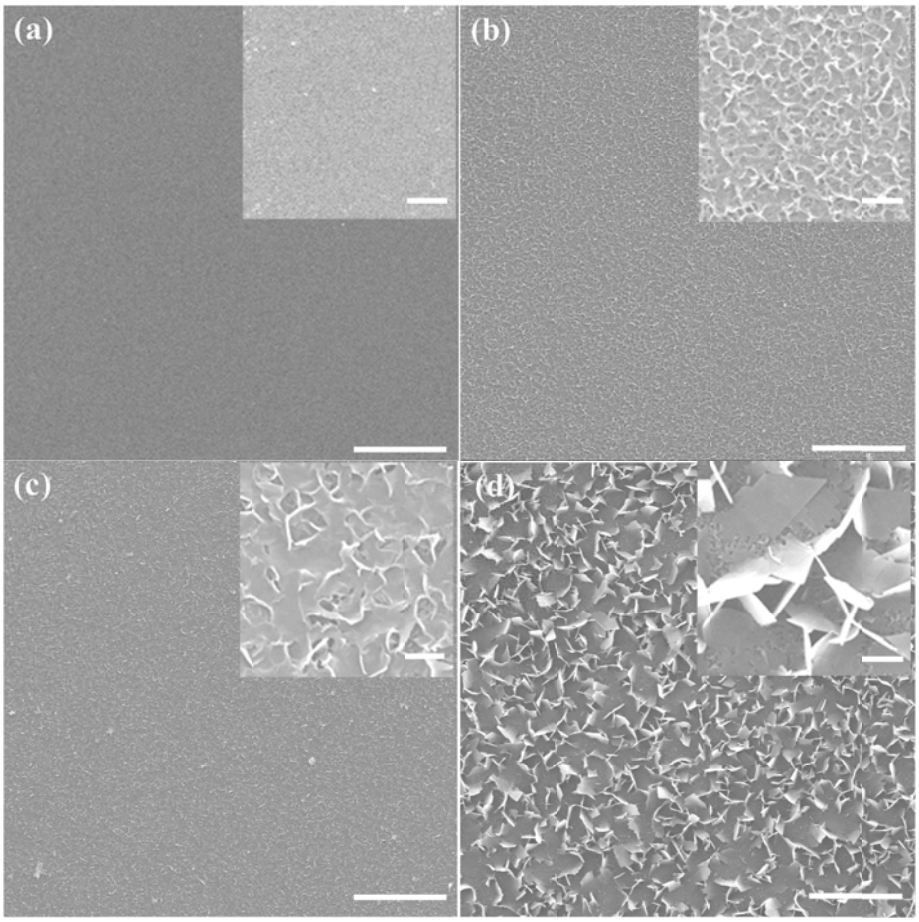

Figure 7.2 Representative SEM images of PEMs/CaP-Col coating grown from the bio-mimetic solution with different incubation time (a) 0 h, (b) 1 h, (c) 2 h, and (d) 24 h. The insets are corresponding magnified images. The scale bars indicate 20 μm, and the scale bars in the insets indicate 1 μm.

surface feature became distinct at 2 h (Figure 7.2 c), bigger crystals and pores between the crystals were observed. Upon incubation for 24 h (Figure 7.2 d), the surface feature had an obvious change to micro "flower"-like, with micro-sized petal erectly sitting on the surface. We also observed the micro-flower surface feature on PEMs/CaP samples upon 24 h incubation without the addition of the collagen (Figure 7.3), indicating that the surface feature was dominated by the CaP crystal nucleation and growing process, where the collagen did not play a critical role. In addition, the whole substrate was homogeneously covered with CaP crystals as shown in Figure 7.2, which ensured an accurate analysis on MSC cellular behaviors.

X-Ray Photoelectron Spectroscopy (XPS) was used to detect the elemental composition of the PEMs/CaP-Col coating. Compared with PEMs (Figure 7.4 a bottom), Ca and P signals appeared in both PEMs/CaP (Fig. 7.4 a middle) and PEMs/CaP-Col (Figure 7.4 a top) samples, indicating the formation of CaP within the PEMs. For PEMs *versus* PEMs/CaP, the disappearance of N signal (Figure 7.4 a middle) suggested that the coating was too thick to be penetrated by XPS (several ten nanometers), which suggested that the reappearance of N signal in PEMs/CaP-Col (Figure 7.4 a top) was from the doped collagen. In the detailed elemental analysis, the N content in the PEMs/CaP-Col samples fabricated at different incubation times dropped from the beginning 4.7% in PEMs (Figure 7.4 b left) and leveled to 1.4% after 45 min. Meanwhile, other elements (C, O, Ca and P) in PEMs/CaP-Col showed the similar trend as N, i.e. fluctuating at 25 min and leveling from 45 min onwards (Table 7.1). CaP has several crystal forms, including α- and β-tricalcium phosphate, tetracalcium phosphate, octacalcium phosphate, dicalcium phosphate dehydrate and hydroxyapatite (HAp). Among them, the HAp has the highest

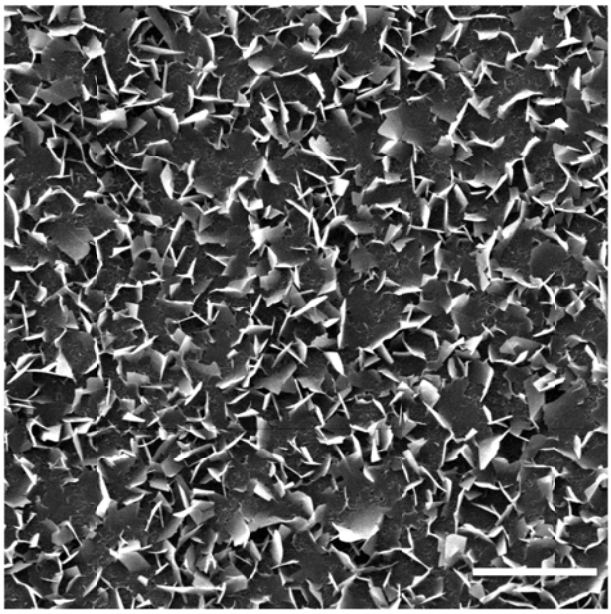

Figure 7.3 Representative SEM image of PEMs/CaP coating grown from the bio-mimetic solution 24 h without collagen. The scale bars indicates 20 μm.

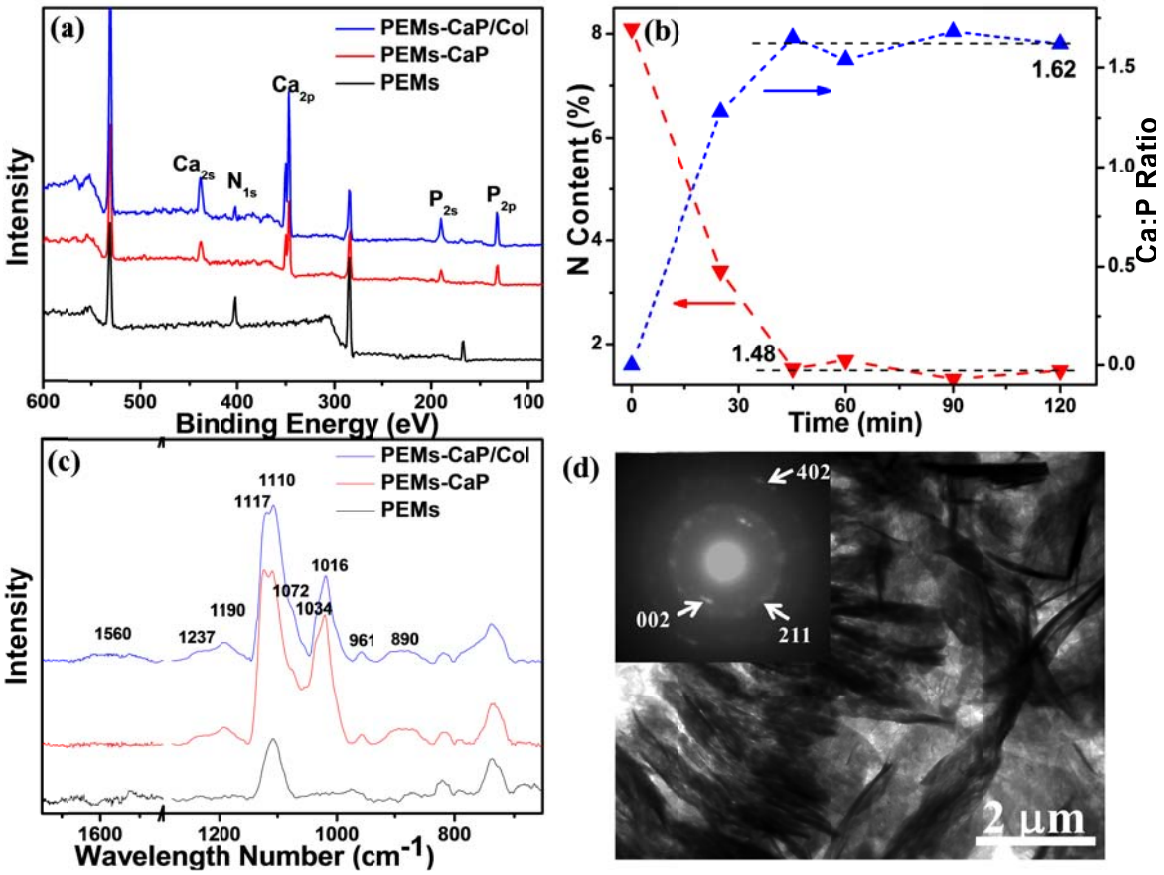

Figure 7.4 (a) XPS spectra of PEMs (bottom), PEMs/CaP (middle) and PEMs/CaP-Col (top) after 2h incubation. (b) The dependence of N content percent and the Ca:P ratio in PEMs/CaP-Col on incubation time. (c) ATR-IR spectra of PEMs (bottom), PEMs/CaP (middle) and PEMs/CaP-Col (top) after 2 h incubation. (d) TEM image of the PEMs/CaP-Col film obtained upon 2 h incubation, and the corresponding selected area electron diffraction (the inset).

Table 7.1 Element content in CaP-Col coatings with different incubation time.

Samples (mins)	Element content (%)					
	C	N	O	S	P	Ca
0	69.2	8.1	18.5	4.2	0	0
25	37.4	3.4	31.2	0	11.3	16.7
45	25.8	1.5	44.9	0	10.5	17.3
60	23.2	1.6	48.8	0	10.4	16
90	23.8	1.3	46	0	10.8	18.1
120	24.5	1.5	47.6	0	9.9	16.5

chemical similarity to the CaP in bone [27]. Furthermore, the ratio of Ca to P in PEMs/CaP-Col was leveled to 1.62 after 45 min incubation, which was close to the ratio of Ca to P (1.67) in HAp with chemical formula $Ca_{10}(OH)_2(PO_4)_6$ [49]. It suggests that the major composition in PEMs/CaP-Col coating is the HA, and the slightly lower Ca/P ratio is attributed to the other forms of CaP crystal or amorphous CaP, which is consistent with other reports [48].

The Attenuated Total Reflection Infrared (ATR-IR) spectra gave more information of these bio-mimetic surfaces, as shown in Figure 7.4 c. Compared to the PEMs (bottom, Figure 7.4 c), the main vibration bands at 961 cm^{-1} (symmetric stretching mode of the P−O bonds in PO_4^{3-}), 1016 cm^{-1} and shoulders at 1034 cm^{-1}, 1072 cm^{-1} (triply degenerated asymmetric stretching mode of the P−O bond of the PO_4^{3-}) confirmed the existence of HAp in both of PEMs/CaP (middle, Figure 7.4 c) and PEMs/CaP-Col (top, Figure 7.4 c) [48-50]. Vibration bands at 1110 cm^{-1} (CO_3^{2-} in non-stoichiometric apatite), and the wide peak with the center at 890 cm^{-1} (the overlap of bending mode and stretching mode of the CO_3^{2-}group in apatite) indicated the apatite is carbonated substitute. In addition, the vibration around 1237 cm^{-1}, 1190 cm^{-1}, 1117 cm^{-1} and 1110 cm^{-1} is due to the appearance of OCP [48-50]. Compared with PEMs/CaP, the wide peak centered at 1560 cm^{-1} in PEMs/CaP-Col is attributed to the Amide-I, II and III in collagen [51, 52]. Because of the low collagen content in PEMs/CaP-Col and the interference of the water in this vibration region, the peak intensities were too weak to separate from each other. The film of PEMs/CaP-Col was scratched off from the substrate and observed under TEM (Figure 7.4 d), and the crystal size was around micrometer scale. The selected area electron diffraction gave the characteristic diffraction index (002), (211),

and (402) of Hap [53]. All samples of PEMs/CaP-Col under different incubation time showed the same diffraction index except the 25 min incubation sample, in which no diffraction pattern was observed under TEM (Figure 7.5).

7.2.2 Roughness of PEMs/CaP-Col surface

As a quantitative measure of surface texture, the roughness of the PEMs/CaP-Col samples obtained at different incubation time was evaluated by AFM, in terms of a root mean square value, Ra, that describes the distance between peaks (or troughs) along an arbitrary line [54]. Figure 7.6 showed the AFM images and their corresponding roughness change of the coating with the incubation time. The coating roughness increased with the incubation time, from 11 ± 1.2 nm of PEMs to 187 ± 7.3 nm of PEMs/CaP-Col surface upon 2 h incubation. Further incubation lead to the increase of the roughness of PEMs/CaP-Col surface (Figure 7.7). For PEMs/CaP-Col after 24 h of incubation, the roughness reached as high as 737 ± 10.2 nm. However, the bio-mimetic coating surface obtained from longer incubation time than 2 h lead to the death of the long term (14 days) cultured cell on these rougher coatings. This is possibly due to a high cellular stress caused by the reduced contact area between cell membrane and substrate [55]. In this study, the roughness window of cells grown on PEMs/CaP-Col surfaces is between 11 ± 1.2 and 187 ± 7.3 nm, with time scale from 0 to 120 min.

The roughness of the PEMs/CaP-Col was measured again by AFM after the film was incubated in medium for 3 days at 37 °C. A slight decrease in roughness but not obvious was observed (Figure 7.8), indicating the films formed by the biomimetic method were stable and suitable for the cell culture. From another aspect, the stability of

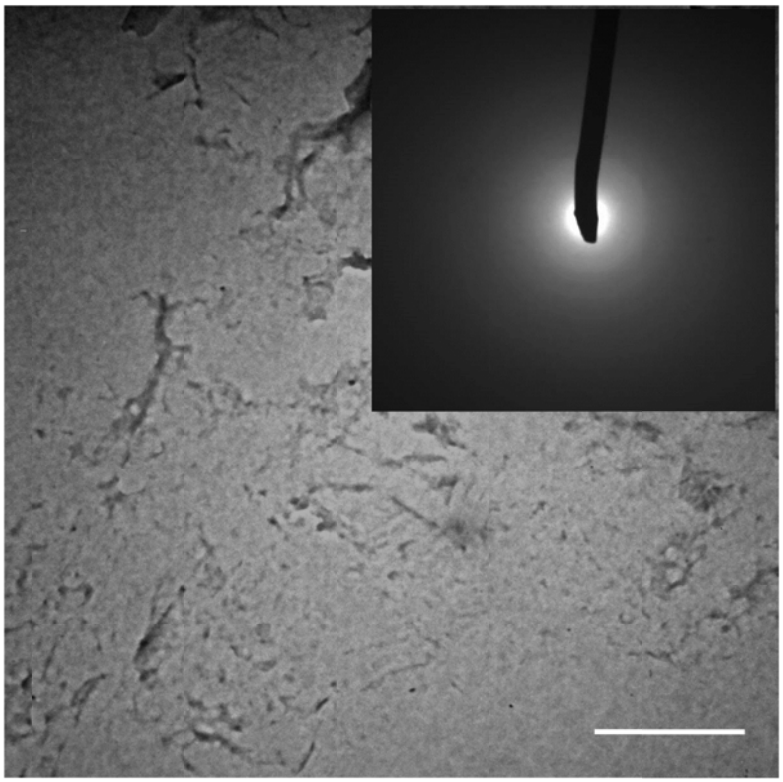

Figure 7.5 TEM image of the PEMs/CaP-Col film obtained from 25 min incubation, and the corresponding selected area electron diffraction (the inset).

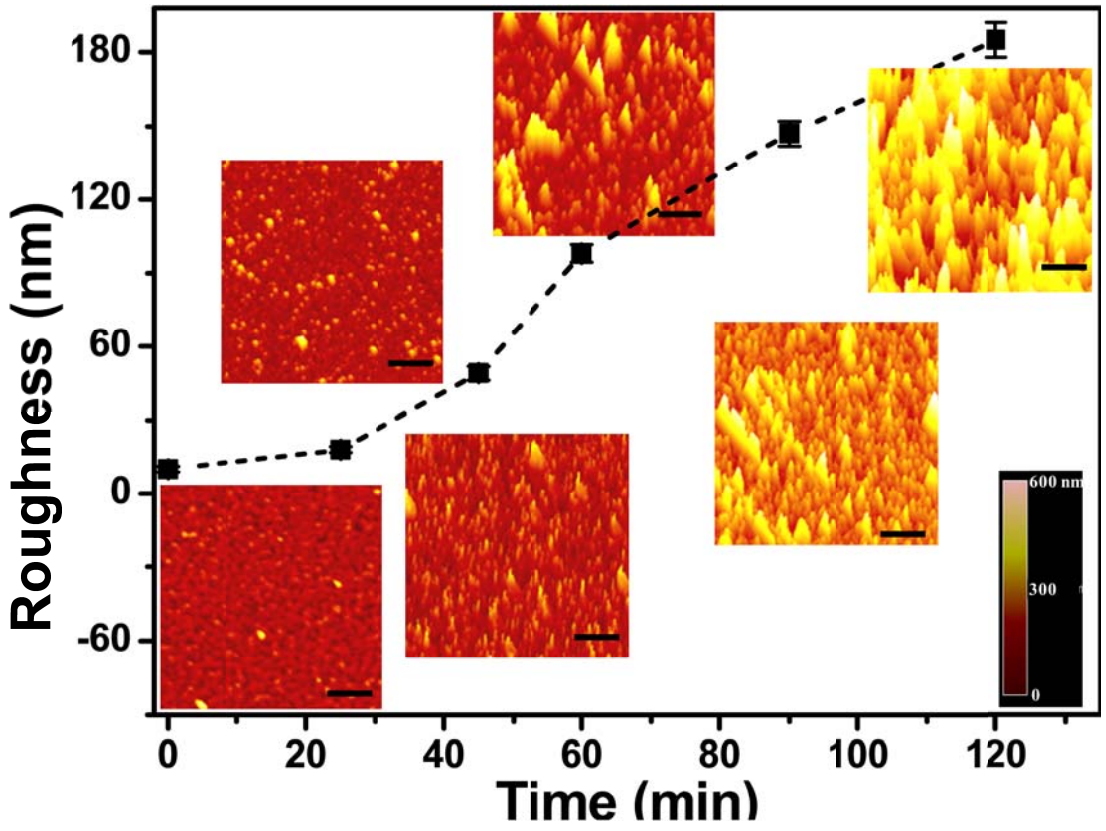

Figure 7.6 The roughness of the PEMs/CaP-Col changed with the incubation time in bio-mimetic solution. The insets are the AFM images at their corresponding time point and the height scale (right bottom) bar of these images. The scale bars in the AFM images indicate 5 μm. The roughness data shown here was the average value of at least 3 tests from 3 different samples.

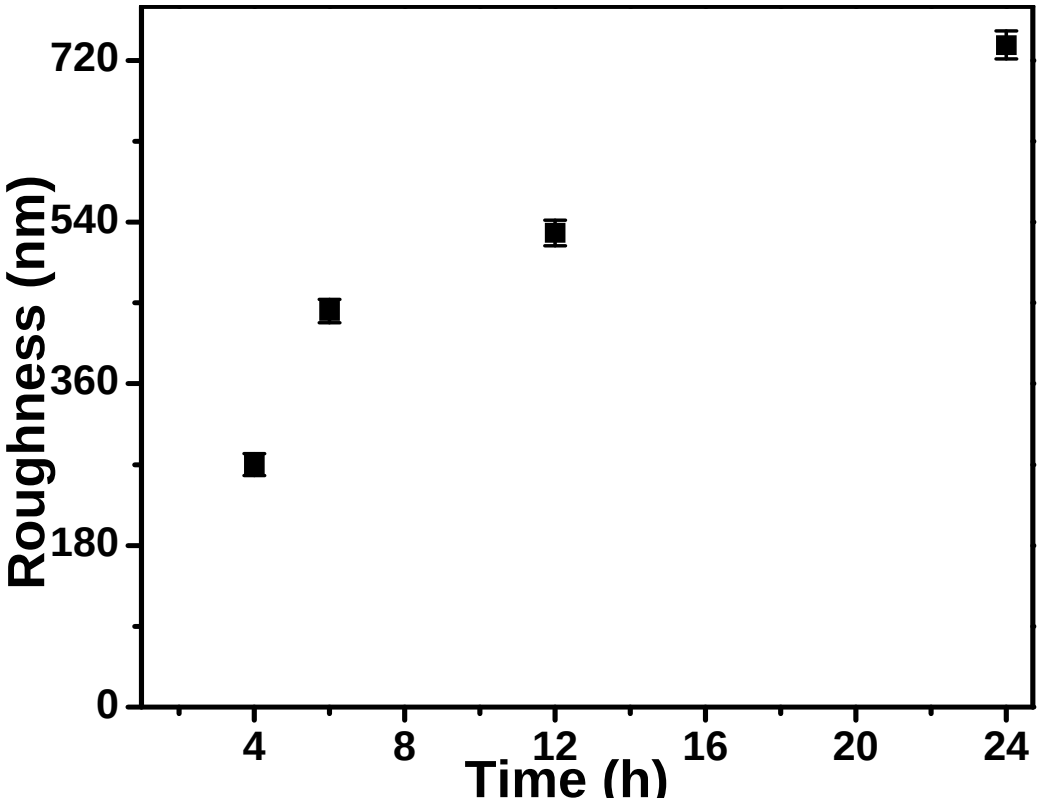

Figure 7.7 The roughness of the PEMs/CaP-Col changed with the incubation time in bio-mimetic solution. The roughness data shown here was the average value of at least 3 tests from 3 different samples.

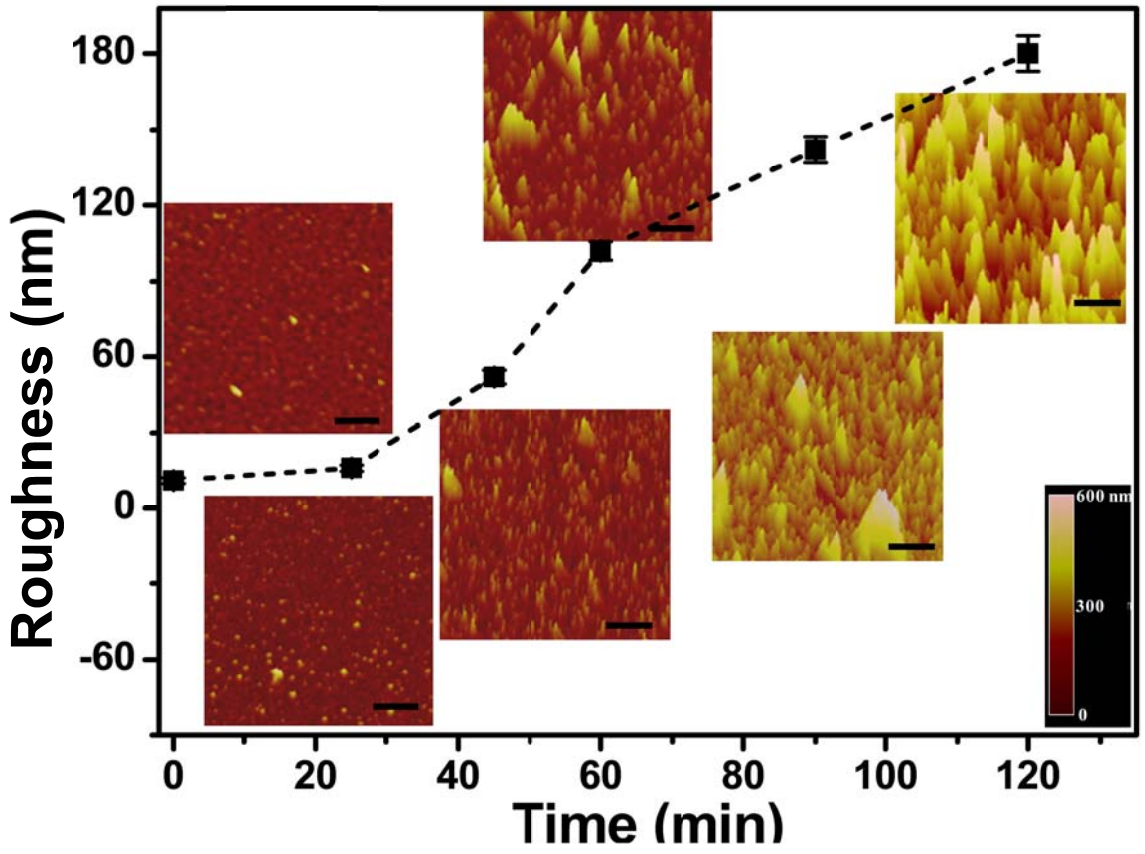

Figure 7.8 The roughness of the PEMs/CaP-Col after 3 days incubation in medium at 37 °C changed with the incubation time in bio-mimetic solution. The scale bars in the AFM images indicate 5 μm. The roughness data shown here was the average value of at least 3 tests from 3 different samples.

the film reflected the HAp as major composition of the CaP/Col coating due to its reported super stability. And the slight decrease of the roughness might be attributed to the dissolving of other forms of CaP. All data indicated that the CaP-Col coating is identical in chemical compositions (with HAp as the major CaP composites) and stable for cell culture when the incubation time is more than 45 min.

7.2.3 Substrate biocompatibility and BMSC proliferation

BMSCs were grown on PEMs/CaP-Col samples for 21 days and cell viability was examined. Figure 7.9 a showed the live/dead staining of BMSCs after 3 weeks of culture in growth media. Red stain from propidium iodide (PI) of cells on the PEMs samples indicated the cell apoptosis and poor cell viability on PEMs surface. Clearly the CaP-Col coatings on PEM improved biocompatibility dramatically based on the staining results from calcein AM and PI (Figure 7.9 a). The number of adherent BMSCs on each surface was also quantified by CellTiter Blue® assay. The data revealed that there were significantly higher cell numbers on PEMs/CaP-Col with 60 and 90 min coatings (Figure 7.9 b). Any CaP-Col coating of less than 60 min appeared to be less biocompatible, likely due to the existence of the soluble amorphous CaP, which, according to Oreffo *et al.* [56], could rapidly release ions and perturb local pH, which negatively affects cell proliferation and viability.

7.2.4 Osteo-specific gene expression

The expression of genes associated with osteogenic differentiation was examined in order to evaluate substrate osteo-conductivity. BMSCs were cultured on these samples for 21 days without traditional osteo-inductive supplements, like dexamethasone, ascorbic acid,

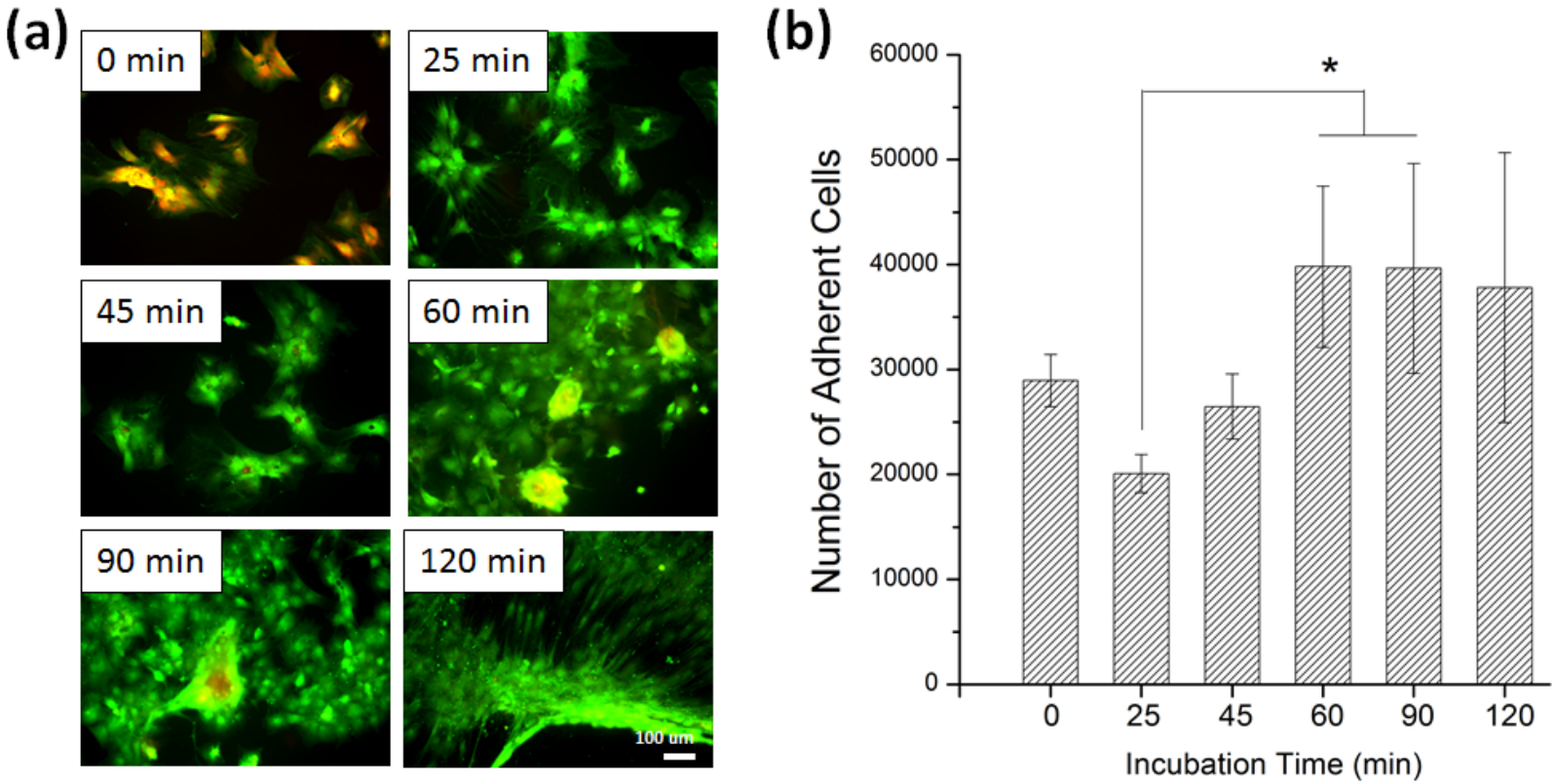

Figure 7.9 Cell proliferation analyses of BMSCs on PEMs and PEMs/CaP-Col substrates at day 21. (a) Live (green) and dead (red) staining of cells by calcein AM and propidium iodide. The scale bar equals to 100 µm. (b) Number of adherent BMSCs on different surface. The error bars denote ± 1 s.d. and (*) represents $p < 0.05$.

and β-glycerophosphate [7], thus the osteogenic signal is believed to come from PEMs/CaP-Col coating. Transcription factors that regulate osteogenesis include *DLX5*, *RUNX2*, and *OSX*. There was no difference in *DLX5* and *RUNX2* gene expression, however, *OSX* expression was upregulated in cells grown on all PEMs/CaP-Col compared to TCP control (Figure 7.10). Since *DLX5* and *RUNX2* are normally expressed earlier and before osteogenic commitment [57], it is possible that BMSCs had already committed to the osteogenic lineage at the time of analysis. On the other hand, *OSX* is a transcription factor downstream of *RUNX2* [58] and its upregulation could be observed during osteogenic maturation. The upregulation of *OSX* suggests that the top coating of CaP-Col on PEMs can induce osteogenesis of BMSCs without any osteo-inductive supplements in the culture medium.

Another osteo-specific gene studied was *BGLAP* (or osteocalcin), the most common marker of mature osteoblast, as this protein is only synthesized by fully-differentiated osteoblasts [59]. The gene expression level of *BGLAP* was significantly increased in cells grown on PEMs/CaP-Col surface at 60 and 90 min incubation time, with 60 min incubation resulting in the highest *BGLAP* gene expression level. This suggests that BMSCs on PEMs/CaP-Col were capable of terminal osteogenic differentiation into mature osteoblasts on these two substrates by 21 days. This result also confirmed that HAp is more osteo-conductive than amorphous CaP of PEMs/CaP-Col upon 25 min incubation, similar to what has been reported previously [33].

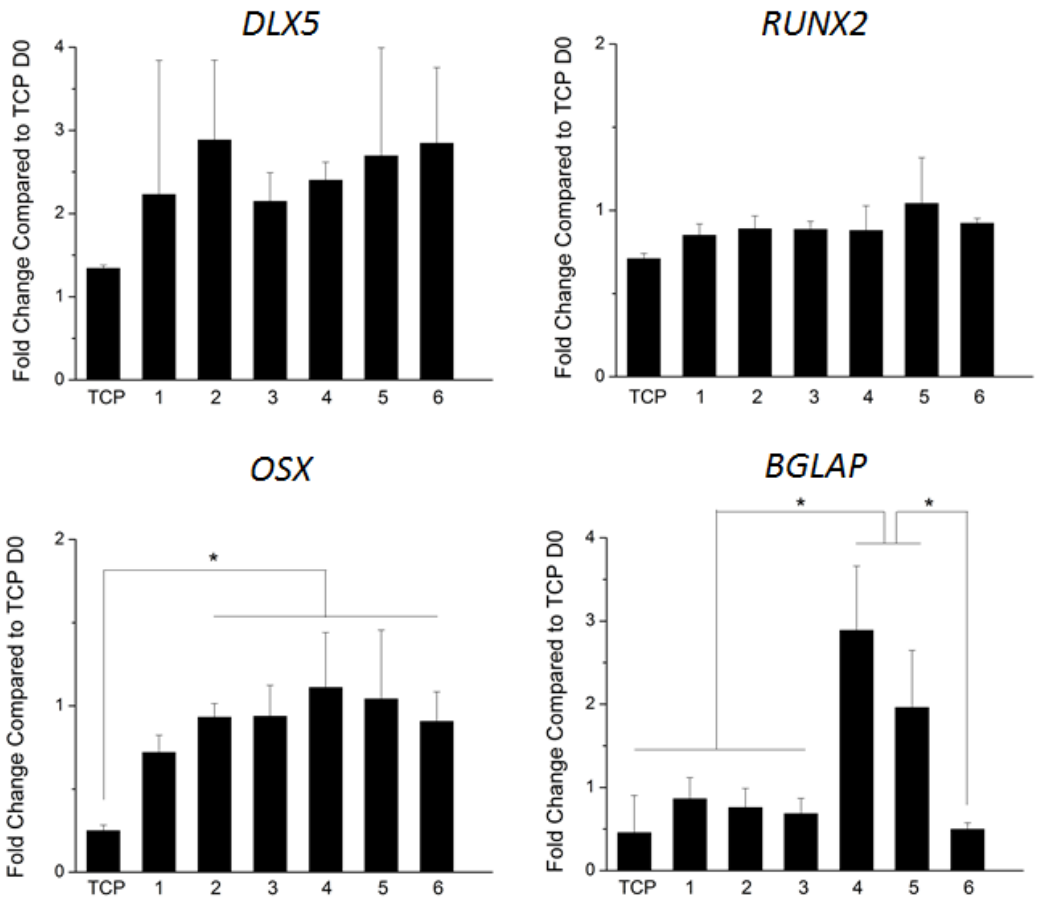

Figure 7.10 RT-qPCR analysis for osteo-specific gene expression of BMSCs on different PEMs/CaP-Col roughness at day 21 without osteoinduction. Different substrates include TCP: standard tissue culture plastic, 1: PEMs alone without CaP-Col, 2: PEMs/CaP-Col for 25 min, 3: PEMs/CaP-Col for 45 min, 4: PEMs/CaP-Col for 60 min, 5: PEMs/CaP-Col for 90 min, and 6: PEMs/CaP-Col for 120 min. In all graphs, the error bars denote ± 1 s.d. and (*) represents $p < 0.05$.

7.2.5 Protein expression of osteocalcin

Immunohistochemical staining was performed to confirm that gene expression observed (Figure 7.10) was correlated with protein expression. The staining images showed that osteocalcin protein was indeed highly expressed in BMSCs on PEMs/CaP-Col with 60, 90, and 120 min incubation time (Figure 7.11 a). The protein was mainly localized to cell aggregates and mineralized nodules. Moreover, the actin staining (Figure 7.11 a) revealed a similar cell density on each surface when compared to the live/dead staining in Figure 7.9 a. Thus, the higher osteocalcin expression could be a result of better surface biocompatibility, subsequently higher cell viability and density, which is in agreement with a recent report by Hu *et al.* [33].

7.2.7 Calcium deposition

An indicator for mineralization is calcium deposition, which could be visualized by Alizarin Red S staining. Staining of calcium deposits on each surface is displayed in Figure 7.11 b. All of the cell aggregates was stained positive for calcium production. We noticed that the mineralized nodules in BMSCs on PEMs/CaP-Col with 60 and 90 min incubation time were high in number and larger (Figure 7.11 b). To quantify this observation, we extracted the calcium stained dye from each samples and measured the absorption at 548 nm. The absorbance was then normalized to the number of cells in each sample in order to compared calcium contents regardless of the difference in cell numbers. Calcium deposition was the highest in BMSCs on PEMs/CaP-Col with roughness 98 ± 3.5 nm at a 60 min incubation time (Figure 7.11 c), which agrees with its highest *BGLAP* gene expression level shown in Figure 7.10. Osteocalcin, excreted into

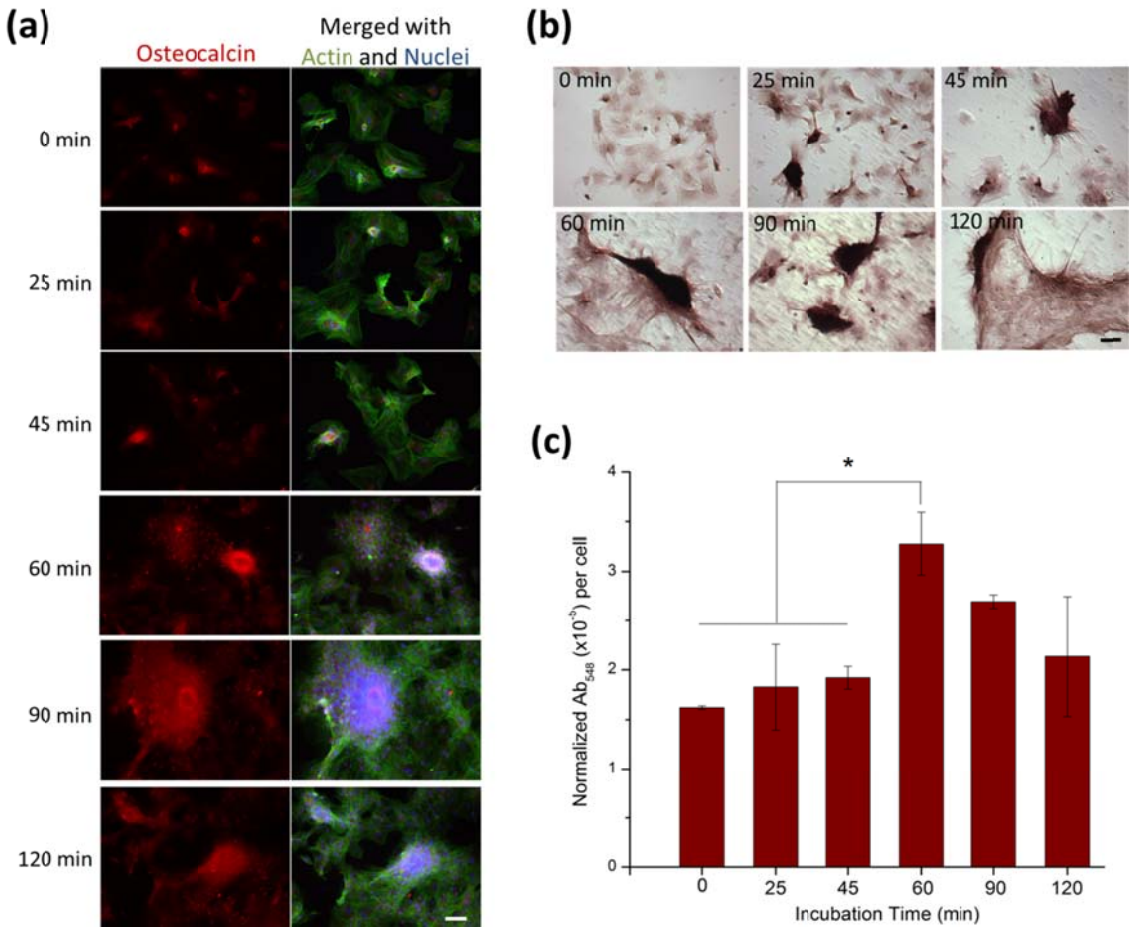

Figure 7.11 Osteocalcin protein expression and calcium deposition of BMSCs on different PEMs/CaP-Col surfaces at day 21. (a) Immunohistochemical staining for osteocalcin (red), and osteocalcin localization by overlaying with actin (green) and nuclei (blue). Scale bar equals 100 µm. (b) Chemical staining for calcium deposits by Alizarin Red S solution. Scale bar equals 100 µm. (c) Quantification of calcium deposits stained by Alizarin Red S normalized with cell numbers. The error bars denote ± 1 s.d. and (*) represents $p < 0.05$.

extracellular matrix, is rich in acidic amino acids to chelate calcium ions from the environment, facilitating mineralization [59]. The finding from these experiments indicates that the surface roughness is critical for osteogenesis, where too low or too high roughness may pose a negative effect on cell proliferation and differentiation [60]. The high sensitivity of the stem cells to the CaP-based surface properties, such as chemistry, particle size and topology, makes it difficult to compare the reported results from different laboratories to get a conclusive answer to the roughness effect on the stem cell osteogenesis [61-65]. A recent work by Kaplan *et al.* [16], demonstrated that the protein surface with higher roughness and stronger micro/nano-scale collectively enhanced the osteogenic differentiation of human mesenchymal stem cells (hMSCs), presented by the up-regulation osteogenic transcript (Col1α1, BSP, OP and Cbfα1) level. Balloni *et al.* examined the changes in hMSCs gene expression after growth on titanium surface with different roughness, and found that three osteogenic factors (Osx, BMP-2, and Runx2) that induce progressive differentiation of mesenchymal cells into osteoblasts were highly expressed on the rougher surface [37]. Surface nanoscale features could enhance the MSCs gene expression related to osteoblast differentiation as shown by Cooper *et al.*[66]. Similarly, a study about osteogenesis on nanostructures of titanium illustrated that roughness at nanoscale promoted osteogenic differentiation compared to a planar control, and the smaller nanostructure (15 nm-high pillars) showed higher efficiency at inducing mineralized nodules and osteogenic proteins than the larger nanostructures (55 and 100 nm-high pillars) [67].

On the other hand, largely increase in roughness could result in fewer contact areas between cell membrane and substrate, leading to an increase in cellular stress [55],

and the adsorbed proteins tended to denature upon binding to such rough surface [68]. Based on these findings, the rougher surface with micro/nano-scale pores (such as CaP-Col coating with 60 and 90 mins incubation in present study) would stimulate the expression of markers of osteoblastic phenotype, and further increased roughness could increase the cell stress or lead to the apoptosis. The optimal surface roughness was supported from previous reports. For example, among four kinds of TiO_2 nanotubes (30, 50, 70, 100 nm) plate with cultured hMSCs two weeks, the TiO_2 nanotubes with medium diameter (70 nm) had the highest expression of the osteogenic markers [69]. Our work, together with some recent literatures, emphasizes the importance of a balance in surface roughness, and thus the optimal surface roughness is necessary for a successful biomaterial implant design in the field of tissue engineering and bone regeneration.

7.3 CONCLUSION

Inspired by the natural bone compositions, a CaP-Col coating was successfully *in situ* grown on PEMs by incubating the PEMs into biomimetic solution under mild conditions. The CaP-Col coating roughness, varing from 11±1.2 to 737 ± 10.2 nm, was controllable by the incubation time. Homogeneity and stability of PEMs/CaP-Col surface, and the invariable chemical compositions and crystallinity with incubation time avoided the interference from other chemical cues on the cell behavior, but suitable for investigating the physical cues, such as the roughness. This study shows that most of PEMs/CaP-Col had good biocompatibility to BMSCs and could induce BMSCs osteogenesis without osteogenic inducing supplement in culture medium. Further assessment on osteo-conductivity of PEMs/CaP-Col coatings suggests that surface roughness, which was often

ignored in most coating designs, is a critical factor on the osteogenesis. The roughness window for BMSCs growing on PEMs/CaP-Col was between 18 ± 1.2 nm and 187 ± 7.3 nm, and culturing BMSCs over this range led to the cell death. Moreover, the PEMs/CaP-Col had an optimum roughness for the osteogenesis of BMSCs, about 98 ± 3.5 nm at 60 min incubation time, where the highest osteocalcin and calcium content were observed.

Our results clearly demonstrate that the surface roughness is important for directing cell behavior, and optimizing the material physical properties is necessary in a success of final implant. It represents a novel approach in easy osteo-conductive coating fabrication with a controllable nano-roughness for bone repair. Furthermore, benefited from the LBL, this PEMs/CaP-Col coating could be generated on various materials surfaces, endowing them with potential to bone tissue engineering by improving bone implant integration and enhancing bone formation without the use of chemical inducer.

7.4 EXPERIMENTAL SECTION

7.4.1 Materials

PSS (Mw ~ 70,000), PAH (Mw ~ 58,000), poly(ethyleneimine) (PEI high branched Mw ~ 60,000), sodium phosphate dibasic (Na_2HPO_4 purity 98.5%), sodium phosphate monobasic (NaH_2PO_4 purity 98.5%), calcium chloride ($CaCl_2$ purity 99.5%), hydrogen chloride (HCl), sodium hydroxide (NaOH) and trishydroxy-aminomethane (Tris, purity 99.9%) were purchased from Sigma-Aldrich used as received. Micro cover glass with diameter 18 mm, and silicon wafer were purchased from VWR. All pH value was adjusted using 0.2 M HCl and 0.2 M NaOH. Deionized water (18.2 MΩ.cm) used for

rinsing and preparing all the solutions was obtained from a Millipore Simplicity 185 purification unit. Rat tail collagen type I was purchased from BD Biosciences.

7.4.2 Substrate treatment and PEMs preparation

Glass slides and silicon wafers were immersed in slightly boiled piranha solution (3:1 mixture of 98% H_2SO_4 and 30% H_2O_2) for 20 min followed by ultrasonication three times in pure water, rinsing with copious amounts of water, and drying with a stream of nitrogen gas.

PEI, PAH and PSS solutions were prepared by dissolving in 10 mM Tris/HCl buffer with 150 mM NaCl, with final concentration 5 $mg \cdot mL^{-1}$ at pH 7.4. The polyelectrolyte multilayer films preparation followed the previous report [70]. In brief, the glass coverslip was immersed into PEI solution for 20 min, then alternatively immersed into the PAH and PSS solutions for 20 min until five layers were obtained (with PAH as outmost layer), the substrate was thoroughly washed using water between each layer.

7.4.3 Bio-mimetic surface preparation

Calcium solutions were prepared from $CaCl_2$ with a concentration of 20 mM. Phosphate solutions were obtained by mixing equimolar solutions of $Na_2HPO_4 \cdot 7H_2O$ and $NaH_2PO_4 \cdot H_2O$ with 20 mM phosphate. Both calcium and phosphate solutions were prepared with 10 mM Tris/HCl buffer in the presence of 150 mM NaCl, at pH 6.85 - 6.9. The bio-mimetic solution containing calcium, phosphate (molar ratio Ca/P = 1.0), and collagen were prepared by mixing calcium, phosphate, Tris/HCl buffer and collagen

solutions, with final concentration of 8.3 mM calcium, 8.3 mM phosphate, and 30 $\mu g \cdot mL^{-1}$ collagen, at pH 6.85 - 6.9. Once PEMs were formed, the glass coverslip were horizontally incubated in the above mentioned solutions at room temperature. The desired testing surfaces were formed in the bottom side of the glass coverslip. The freshly prepared mixture solution was used for each sample preparation. After desired incubated time, the sample was washed extensively with water and dried with nitrogen gas before the test. For control sample preparation, the PEMs were incubated in the similar solution without collagen under the same conditions. The samples prepared without and with collagen were abbreviated as PEM/CaP and PEMs/CaP-Col, respectively.

7.4.4 Characterization

The surface morphology was observed by atomic force microscopy using a NanoScope IIIA MultiMode AFM (Veeco) under the tapping mode. ATR-IR spectra were obtained on a Bruker Vertex 70 FTIR spectrometer equipped with a DTGS detector using a PIKE ATR accessory with a ZnSe crystal. XPS spectra were obtained on a ThermoElectron ESCALAB 250 spectrometer equipped with a monochromatic Al X-ray source (1486.6 eV). The spectra were recorded at a 90° take off angle with 20-eV pass energy. Scanning electron microscopy (SEM) images were taken on a JEOL JSM 5600LV scanning electron microscope. Transmission electron microscopy (TEM) observations were carried out on a JEM-2010 microscope operating at 100.0 kV.

7.4.5 BMSC isolation and expansion

Primary BMSCs were isolated from the bone marrow of young adult 150 g male Wistar rats (Harlan Sprague Dawley, Inc.). The procedures were performed in accordance with the guidelines for animal experimentation by the Institutional Animal Care and Use Committee, School of Medicine, University of South Carolina. In brief, cells were flushed from tibia and femur using a syringe needle. The cell suspension was then cultured on tissue culture plastic (TCP) for 10 days to allow attachment, with consistent washing every three days. The attached cells were passaged and maintained in DMEM growth medium supplemented with 10% fetal bovine serum (FBS), penicillin (100 μg/mL), streptomycin (100 μg/mL) and amphotericin B (250 ng/mL). Cells were passaged no more than four times after isolation before experimental testing.

7.4.6 Cell culture and proliferation

Each glass coverslip sample was seeded with 4.0×10^4 cells in growth medium and cultured for 21 days. Media was replenished every 3 - 4 days. Cell proliferation was measured by using CellTiter Blue® (Promega) at day 21 after seeding. Before cell culture termination, each sample was stained with 4 μg/mL of Calcein AM (BD Biosciencse) and 4 μg/mL of propidium iodide in culture media for 30 min at 37 °C. The cells were washed with Hyclone Dulbecco's phosphate buffered saline (DPBS; Thermo Scientific) twice and fixed in 4% paraformaldehyde for 30 min at room temperature. Images of the stained substrates were visualized under Olympus IX81 fluorescent microscopy.

7.4.7 Gene expression analysis

BMSCs (4.0×10^4) were seeded on each glass coverslip in growth medium and cultured for 21 days. BMSCs with similar density were seeded on 3.8 cm^2 TCP as a standard control and cultured for the same time period. Media was replenished every 3 - 4 days. The cell cultures were terminated at the mentioned time point and total RNA was subsequently extracted using E.Z.N.A. total RNA isolation kit (Omega). The quality and quantity of the extracted RNA were analyzed using Bio-Rad Experion (Bio-Rad Laboratories) and the RNA was reverse transcribed by using qScript™ cDNA Supermix (Quanta Biosciences). RT-qPCR (iQ5 real-time PCR detection system Bio-Rad Laboratories) was done by the method described as: 60 cycles of PCR (95 °C for 20 s, 58 °C for 15 s, and 72 °C for 15 s), after initial denaturation step of 5 minutes at 95 °C , by using 12.5 µL of iQ5 SYBR Green I supermix, 2 pmol/µL of each forward and reverse primers and 0.5 µL cDNA templates in a final reaction volume of 25 µL. Glyceraldehyde 3-phosphate dehydrogenase (GAPDH) was used as the housekeeping gene. Data collection was enabled at 72 °C in each cycle and C_T (threshold cycle) values were calculated using the iQ5 optical system software version 2.1.

The expression levels of differentiated genes and undifferentiated genes were calculated using Pfaffl's method (M.W. Pfaffl, G.W. Horgan and L. Dempfle, Relative expression software tool) for group-wise comparison and statistical analysis of relative expression results in real-time PCR, using GAPDH as the reference gene. The primers used for RT-qPCR are shown in Table 7.2. The primers were synthesized commercially (Integrated DNA Technologies, Inc.), and evaluated for an annealing temperature of

Table 7.2 Primers used for RT-qPCR to measure gene expression levels. BGLAP: osteocalcin; DLX5: distal-less homeobox 5; GAPDH: glyceraldehyde 3-phosphate dehydrogenase; OSX: osterix; RUNX2: runt-related transcription factor 2.

Gene	Forward Primer (5'-3')	Reverse Primer (3'-5')
BGLAP	AAAGCCCAGCGACTCT	CTAAACGGTGGTGCCATAGAT
DLX5	ATCATGAAAAACGGGGAGATGCCCC	TGATTGAGCTGGCTGCACTTGGGT
GAPDH	ACTAAAGGGCATCCTGGGCTACACTGA	TGGGTGGTCCAGGGTTTCTTACTCCTT
OSX	CAAGGCAGTTGGCAATAGTGGGCA	ATGTGGCAGCTGTGAATGGGCTT
RUNX2	AACGGGCACCATGGCTTTGGTTT	TTGGAGCAAGGAGAACCCCCAACAT

58˚C.

7.4.8 Osteocalcin immunostaining

BMSCs (4.0×10^4) were seeded on each glass coverslip in growth medium and cultured for 21 days. Media was replenished every 3-4 days. Cells were fixed in 4% paraformaldehyde at room temperature for 30 minutes. Each of the samples was then permeabilized with 0.1% Triton-X 100 for 15 minutes and blocked in 1.5% bovine serum albumin (BSA, Sigma-Aldrich) in PBS for 1 hour at room temperature. After blocking, the cells were incubated overnight with rabbit polyclonal antibody targeting osteocalcin (Santa Cruz) at 1:100 dilution in blocking buffer. Secondary goat anti-rabbit antibody conjugated with Alexa Fluor® 546 (Invitrogen) was used at 1:800 dilution for 2 hours at room temperature. FITC-phalloidin (1:500 in PBS) was used to stain filamentous actin. Nuclei were stained with DAPI (4, 6-diamidino-2-phenylindole, 100 ng/mL). Images of the stained substrates were taken on Olympus IX81 fluorescent microscopy.

7.4.9 Calcium staining and quantification

BMSCs (4.0×10^4) were seeded on each glass coverslip in growth medium and cultured for 21 days. Media was replenished every 3 - 4 days. CellTiter Blue® assay (Promega) was used to determine the number of cells in each sample one hour prior to cell fixation. The cells were washed with DPBS twice and fixed with 4% paraformaldehyde for 30 minutes at room temperature. Fixed samples at day 21 were then stained with 2% Alizarin red solution (Sigma-Aldrich) pH 4.1 - 4.5 for 30 minutes. Since the reaction was highly light sensitive, the substrates were wrapped in aluminum foil during the Alizarin

red staining. After washing with ultrapure water, 200 μL of 0.1 M NaOH was added to each sample to extract the dye from the sample. The amount of dye was quantified by measuring absorbance at 548 nm wavelength. Absorbance values at 548 nm were normalized against cell number from CellTiter Blue® standard curve. At least 3 samples of each condition were used in the analysis.

7.5 REFERENCES

[1] Pittenger MF, Mackay AM, Beck SC, Jaiswal RK, Douglas R, Mosca JD, et al. Multilineage potential of adult human mesenchymal stem cells. Science. 1999;284:143-7.

[2] Mackay AM, Beck SC, Pittenger MF. Human mesenchymal stem cells progress to hypertrophic chondrocytes under specific conditions in vitro. Mol Biol Cell. 1998;9:173-8.

[3] Ferrari G. Skeletal muscle regeneration by bone marrow-derived myogenic progenitors (vol 280, pg 1528, 1998). Science. 1998;281:923-7.

[4] Calvert JW, Marra KG, Cook L, Kumta PN, DiMilla PA, Weiss LE. Characterization of osteoblast-like behavior of cultured bone marrow stromal cells on various polymer surfaces. J Biomed Mater Res. 2000;52:279-84.

[5] Benayahu D, Kletter Y, Zipori D, Wientroub S. Bone-Marrow Derived Stromal Cell-Line Expressing Osteoblastic Phenotype Invitro and Osteogenic Capacity Invivo. J Cell Physiol. 1989;140:1-7.

[6] Nesti LJ, Jackson WM, Shanti RM, Koehler SM, Aragon AB, Bailey JR, et al. Differentiation Potential of Multipotent Progenitor Cells Derived from War-Traumatized Muscle Tissue. J Bone Joint Surg Am. 2008;90A:2390-8.

[7] Jaiswal N, Haynesworth SE, Caplan AI, Bruder SP. Osteogenic differentiation of purified, culture-expanded human mesenchymal stem cells in vitro. J Cell Biochem. 1997;64:295-312.

[8] Ayres CE, Jha BS, Sell SA, Bowlin GL, Simpson DG. Nanotechnology in the design of soft tissue scaffolds: innovations in structure and function. Wiley Interdiscip Rev Nanomed Nanobiotechnol. 2010;2:20-34.

[9] Benoit DSW, Schwartz MP, Durney AR, Anseth KS. Small functional groups for controlled differentiation of hydrogel-encapsulated human mesenchymal stem cells. Nat Mater. 2008;7:816-23.

[10] Discher DE, Mooney DJ, Zandstra PW. Growth Factors, Matrices, and Forces Combine and Control Stem Cells. Science. 2009;324:1673-7.

[11] Woodard JR, Hilldore AJ, Lan SK, Park CJ, Morgan AW, Eurell JAC, et al. The mechanical properties and osteoconductivity of hydroxyapatite bone scaffolds with multi-scale porosity. Biomaterials. 2007;28:45-54.

[12] Pek YS, Wan ACA, Ying JY. The effect of matrix stiffness on mesenchymal stem cell differentiation in a 3D thixotropic gel. Biomaterials. 2010;31:385-91.

[13] Dalby MJ, Gadegaard N, Tare R, Andar A, Riehle MO, Herzyk P, et al. The control of human mesenchymal cell differentiation using nanoscale symmetry and disorder. Nat Mater. 2007;6:997-1003.

[14] Lovmand J, Justesen E, Foss M, Lauridsen RH, Lovmand M, Modin C, et al. The use of combinatorial topographical libraries for the screening of enhanced osteogenic expression and mineralization. Biomaterials. 2009;30:2015-22.

[15] Deligianni DD, Katsala ND, Koutsoukos PG, Missirlis YF. Effect of surface roughness of hydroxyapatite on human bone marrow cell adhesion, proliferation, differentiation and detachment strength. Biomaterials. 2001;22:87-96.

[16] Hu X, Park SH, Gil ES, Xia XX, Weiss AS, Kaplan DL. The influence of elasticity and surface roughness on myogenic and osteogenic-differentiation of cells on silk-elastin biomaterials. Biomaterials. 2011;32:8979-89.

[17] Kaur G, Valarmathi MT, Potts JD, Jabbari E, Sabo-Attwood T, Wang Q. Regulation of osteogenic differentiation of rat bone marrow stromal cells on 2D nanorod substrates. Biomaterials. 2010;31:1732-41.

[18] Sitasuwan P, Lee LA, Bo P, Davis EN, Lin Y, Wang Q. A plant virus substrate induces early upregulation of BMP2 for rapid bone formation. Integr Biol. 2012;4:651-60.

[19] Zhou H, Lee J. Nanoscale hydroxyapatite particles for bone tissue engineering. Acta Biomater. 2011;7:2769-81.

[20] Suchanek W, Yoshimura M. Processing and properties of hydroxyapatite-based biomaterials for use as hard tissue replacement implants. J Mater Res. 1998;13:94-117.

[21] Ducheyne P, Qiu Q. Bioactive ceramics: the effect of surface reactivity on bone formation and bone cell function. Biomaterials. 1999;20:2287-303.

[22] Yang YZ, Kim KH, Ong JL. Review on calcium phosphate coatings produced using a sputtering process - an alternative to plasma spraying. Biomaterials. 2005;26:327-37.

[23] Lu HH, El-Amin SF, Scott KD, Laurencin CT. Three-dimensional, bioactive, biodegradable, polymer-bioactive glass composite scaffolds with improved mechanical properties support collagen synthesis and mineralization of human osteoblast-like cells in vitro. J Biomed Mater Res Part A. 2003;64A:465-74.

[24] Fitter S, Dewar AL, Kostakis P, To LB, Hughes TP, Roberts MM, et al. Long-term imatinib therapy promotes bone formation in CML patients. Blood. 2008;111:2538-47.

[25] Rezwan K, Chen QZ, Blaker JJ, Boccaccini AR. Biodegradable and bioactive porous polymer/inorganic composite scaffolds for bone tissue engineering. Biomaterials. 2006;27:3413-31.

[26] Hench LL. Bioceramics - from Concept to Clinic. J Am Ceram Soc. 1991;74:1487-510.

[27] Dorozhkin SV, Epple M. Biological and medical significance of calcium phosphates. Angewandte Chemie-International Edition. 2002;41:3130-46.

[28] Uchida M, Oyane A, Kim HM, Kokubo T, Ito A. Biomimetic coating of laminin-apatite composite on titanium metal and its excellent cell-adhesive properties. Adv Mater. 2004;16:1071-4.

[29] Oyane A, Ootsuka T, Hayama K, Sogo Y, Ito A. Enhanced immobilization of acidic proteins in the apatite layer via electrostatic interactions in a supersaturated calcium phosphate solution. Acta Biomater. 2011;7:2969-76.

[30] Kokubo T, Kim HM, Kawashita M. Novel bioactive materials with different mechanical properties. Biomaterials. 2003;24:2161-75.

[31] Zhang Y, Zhang MQ. Synthesis and characterization of macroporous chitosan/calcium phosphate composite scaffolds for tissue engineering. J Biomed Mater Res. 2001;55:304-12.

[32] Cai YR, Liu YK, Yan WQ, Hu QH, Tao JH, Zhang M, et al. Role of hydroxyapatite nanoparticle size in bone cell proliferation. J Mater Chem. 2007;17:3780-7.

[33] Hu Q, Tan Z, Liu Y, Tao J, Cai Y, Zhang M, et al. Effect of crystallinity of calcium phosphate nanoparticles on adhesion, proliferation, and differentiation of bone marrow mesenchymal stem cells. J Mater Chem. 2007;17:4690-8.

[34] dos Santos EA, Farina M, Soares GA, Anselme K. Surface energy of hydroxyapatite and ss-tricalcium phosphate ceramics driving serum protein adsorption and osteoblast adhesion. Journal of Materials Science-Materials in Medicine. 2008;19:2307-16.

[35] Meinel L, Karageorgiou V, Hofmann S, Fajardo R, Snyder B, Li CM, et al. Engineering bone-like tissue in vitro using human bone marrow stem cells and silk scaffolds. J Biomed Mater Res Part A. 2004;71A:25-34.

[36] Campoccia D, Arciola CR, Cervellati M, Maltarello MC, Montanaro L. In vitro behaviour of bone marrow-derived mesenchymal cells cultured on fluorohydroxyapatite-coated substrata with different roughness. Biomaterials. 2003;24:587-96.

[37] Balloni S, Calvi EM, Damiani F, Bistoni G, Calvitti M, Locci P, et al. Effects of Titanium Surface Roughness on Mesenchymal Stem Cell Commitment and

Differentiation Signaling. International Journal of Oral & Maxillofacial Implants. 2009;24:627-35.

[38] Costa-Rodrigues J, Fernandes A, Lopes MA, Fernandes MH. Hydroxyapatite surface roughness: Complex modulation of the osteoclastogenesis of human precursor cells. Acta Biomater. 2012;8:1137-45.

[39] Mustafa K, Wennerberg A, Wroblewski J, Hultenby K, Lopez BS, Arvidson K. Determining optimal surface roughness of TiO2 blasted titanium implant material for attachment, proliferation and differentiation of cells derived from human mandibular alveolar bone. Clinical Oral Implants Research. 2001;12:515-25.

[40] Suzuki K, Aoki K, Ohya K. Effects of surface roughness of titanium implants on bone remodeling activity of femur in rabbits. Bone. 1997;21:507-14.

[41] Grizon F, Aguado E, Hure G, Basle MF, Chappard D. Enhanced bone integration of implants with increased surface roughness: a long term study in the sheep. Journal of Dentistry. 2002;30:195-203.

[42] Decher G. Fuzzy nanoassemblies: Toward layered polymeric multicomposites. Science. 1997;277:1232-7.

[43] Kim KS, Zhao Y, Jang H, Lee SY, Kim JM, Kim KS, et al. Large-scale pattern growth of graphene films for stretchable transparent electrodes. Nature. 2009;457:706-10.

[44] Decher G, Hong JD, Schmitt J. Buildup of Ultrathin Multilayer Films by a Self-Assembly Process .3. Consecutively Alternating Adsorption of Anionic and Cationic Polyelectrolytes on Charged Surfaces. Thin Solid Films. 1992;210:831-5.

[45] Tang ZY, Wang Y, Podsiadlo P, Kotov NA. Biomedical applications of layer-by-layer assembly: From biomimetics to tissue engineering. Adv Mater. 2006;18:3203-24.

[46] Boudou T, Crouzier T, Ren KF, Blin G, Picart C. Multiple Functionalities of Polyelectrolyte Multilayer Films: New Biomedical Applications. Adv Mater. 2010;22:441-67.

[47] Murphy WL, Mooney DJ. Bioinspired growth of crystalline carbonate apatite on biodegradable polymer substrata. J Am Chem Soc. 2002;124:1910-7.

[48] Ngankam PA, Lavalle P, Voegel JC, Szyk L, Decher G, Schaaf P, et al. Influence of polyelectrolyte multilayer films on calcium phosphate nucleation. J Am Chem Soc. 2000;122:8998-9004.

[49] Raynaud S, Champion E, Bernache-Assollant D, Thomas P. Calcium phosphate apatites with variable Ca/P atomic ratio I. Synthesis, characterisation and thermal stability of powders. Biomaterials. 2002;23:1065-72.

[50] Koutsopoulos S. Synthesis and characterization of hydroxyapatite crystals: A review study on the analytical methods. J Biomed Mater Res. 2002;62:600-12.

[51] George A, Malone JP, Veis A. The secondary structure of type I collagen N-telopeptide as demonstrated by Fourier transform IR spectroscopy and molecular modeling. Proc - Indian Acad Sci, Chem Sci. 1999;111:121-31.

[52] Payne KJ, Veis A. Fourier-Transform Ir Spectroscopy of Collagen and Gelatin Solutions - Deconvolution of the Amide I-Band for Conformational Studies. Biopolymers. 1988;27:1749-60.

[53] de Jonge LT, Leeuwenburgh SCG, van den Beucken JJJP, te Riet J, Daamen WF, Wolke JGC, et al. The osteogenic effect of electrosprayed nanoscale collagen/calcium phosphate coatings on titanium. Biomaterials. 2010;31:2461-9.

[54] Ducker WA, Senden TJ, Pashley RM. Direct Measurement of Colloidal Forces Using an Atomic Force Microscope. Nature. 1991;353:239-41.

[55] Thomas WE, Discher DE, Shastri VP. Mechanical Regulation of Cells by Materials and Tissues. MRS Bull. 2010;35:578-83.

[56] Oreffo ROC, Driessens FCM, Planell JA, Triffitt JT. Effects of novel calcium phosphate cements on human bone marrow fibroblastic cells. Tissue Eng. 1998;4:293-303.

[57] Nishimura R, Hata K, Ikeda F, Ichida F, Shimoyama A, Matsubara T, et al. Signal transduction and transcriptional regulation during mesenchymal cell differentiation. J Bone Miner Metab. 2008;26:203-12.

[58] Nakashima K, Zhou X, Kunkel G, Zhang ZP, Deng JM, Behringer RR, et al. The novel zinc finger-containing transcription factor Osterix is required for osteoblast differentiation and bone formation. Cell. 2002;108:17-29.

[59] Fujisawa R, Tamura M. Acidic bone matrix proteins and their roles in calcification. Frontiers in Bioscience-Landmark. 2012;17:1891-903.

[60] Loiselle AE, Wei L, Faryad M, Paul EM, Lewis GS, Gao J, et al. Specific Biomimetic Hydroxyapatite Nanotopographies Enhance Osteoblastic Differentiation and Bone Graft Osteointegration. Tissue Eng Part A. 2013;19:1704-12.

[61] Lavenus S, Pilet P, Guicheux J, Weiss P, Louarn G, Layrolle P. Behaviour of mesenchymal stem cells, fibroblasts and osteoblasts on smooth surfaces. Acta Biomater. 2011;7:1525-34.

[62] Phillips JE, Petrie TA, Creighton FP, Garcia AJ. Human mesenchymal stem cell differentiation on self-assembled monolayers presenting different surface chemistries. Acta Biomater. 2010;6:12-20.

[63] Olivares-Navarrete R, Hyzy SL, Hutton DL, Erdman CP, Wieland M, Boyan BD, et al. Direct and indirect effects of microstructured titanium substrates on the induction of mesenchymal stem cell differentiation towards the osteoblast lineage. Biomaterials. 2010;31:2728-35.

[64] Samavedi S, Whittington AR, Goldstein AS. Calcium phosphate ceramics in bone tissue engineering: A review of properties and their influence on cell behavior. Acta Biomater. 2013;9:8037-45.

[65] Shi ZL, Huang X, Cai YR, Tang RK, Yang DS. Size effect of hydroxyapatite nanoparticles on proliferation and apoptosis of osteoblast-like cells. Acta Biomater. 2009;5:338-45.

[66] Mendonca G, Mendonca DBS, Simoes LGP, Araujo AL, Leite ER, Duarte WR, et al. The effects of implant surface nanoscale features on osteoblast-specific gene expression. Biomaterials. 2009;30:4053-62.

[67] Sjostrom T, Dalby MJ, Hart A, Tare R, Oreffo ROC, Su B. Fabrication of pillar-like titania nanostructures on titanium and their interactions with human skeletal stem cells. Acta Biomater. 2009;5:1433-41.

[68] Roach P, Farrar D, Perry CC. Surface tailoring for controlled protein adsorption: Effect of topography at the nanometer scale and chemistry. J Am Chem Soc. 2006;128:3939-45.

[69] Moon KS, Yu SH, Bae JM, Oh S. Biphasic Osteogenic Characteristics of Human Mesenchymal Stem Cells Cultured on TiO2 Nanotubes of Different Diameters. J Nanomater. 2012;2012:Article ID 252481.

[70] Zan XJ, Su ZH. Incorporation of Nanoparticles into Polyelectrolyte Multilayers via Counterion Exchange and in situ Reduction. Langmuir. 2009;25:12355-60.

APPENDIX A – REPRINT PERMISSION FOR CHAPTER 1

CONTRACTS-COPYRIGHT (shared) <Contracts-Copyright@rsc.org>
Mon 11/18/2013 3:59 AM
To:SITASUWAN, PONGKWAN <sitasuwp@email.sc.edu>;

Dear Pongkwan

The Royal Society of Chemistry (RSC) hereby grants permission for the use of your paper(s) specified below in the printed and microfilm version of your thesis. You may also make available the PDF version of your paper(s) that the RSC sent to the corresponding author(s) of your paper(s) upon publication of the paper(s) in the following ways: in your thesis via any website that your university may have for the deposition of theses, via your university's Intranet or via your own personal website. We are however unable to grant you permission to include the PDF version of the paper(s) on its own in your institutional repository. The Royal Society of Chemistry is a signatory to the STM Guidelines on Permissions (available on request).

Please note that if the material specified below or any part of it appears with credit or acknowledgement to a third party then you must also secure permission from that third party before reproducing that material.

Please ensure that the thesis states the following:

Reproduced by permission of The Royal Society of Chemistry

and include a link to the paper on the Royal Society of Chemistry's website.

Please ensure that your co-authors are aware that you are including the paper in your thesis.

Regards

Gill Cockhead
Publishing Contracts & Copyright Executive
Royal Society of Chemistry,
Thomas Graham House,
Science Park, Milton Road,
Cambridge, CB4 0WF, UK
Tel +44 (0) 1223 432134

APPENDIX B – REPRINT PERMISSION FOR CHAPTER 6

Thank You For Your Order!

Dear Miss. Pongkwan Sitasuwan,

Thank you for placing your order through Copyright Clearance Center's RightsLink service. Elsevier has partnered with RightsLink to license its content. This notice is a confirmation that your order was successful.

Your order details and publisher terms and conditions are available by clicking the link below:
http://s100.copyright.com/CustomerAdmin/PLF.jsp?ref=a006e225-b623-4ce1-a6fa-e6eacc71e138

Order Details
Licensee: Pongkwan Sitasuwan
License Date: Nov 4, 2013
License Number: 3262150515727
Publication: Acta Biomaterialia
Title: Polyvalent display of RGD motifs on turnip yellow mosaic virus for enhanced stem cell adhesion and spreading
Type Of Use: reuse in a thesis/dissertation
Total: 0.00 USD

To access your account, please visit https://myaccount.copyright.com.

Please note: Online payments are charged immediately after order confirmation; invoices are issued daily and are payable immediately upon receipt.

To ensure we are continuously improving our services, please take a moment to complete our customer satisfaction survey.

B.1:v4.2

+1-877-622-5543 / Tel: +1-978-646-2777